Università degli Studi di Padova

Dipartimento di Fisica e Astronomia "Galileo Galilei"

Corso di Laurea Magistrale in Astronomia

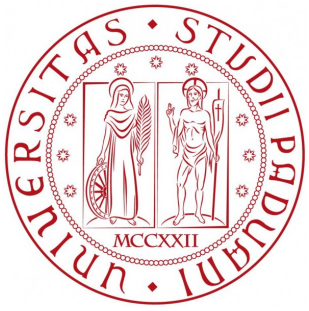

Primordial non-Gaussianity and scale-dependent bispectra in the Cosmic Microwave Background

Relatore: Dott. Michele Liguori
Correlatore: Prof. Giuseppe Tormen

Laureando: Filippo Oppizzi

Corso di Laurea in Astronomia

Tesi di Laurea Magistrale

Anno Accademico 2013-2014

Introduzione

La *Teoria dell'Inflazione* permette di superare molti dei limiti intriseci dell'attuale Modello Cosmologico Standard, spiegando inoltre il meccanismo che ha determinato le condizioni iniziali da cui si è evoluto l'Universo. Secondo il modello inflazionario, nei primissimi istanti di vita ($\sim 10^{-37} s$ dopo la singolarità iniziale), l'Universo ha attraversato un periodo di espansione enormemente accelerata, detto appunto Inflazione. Durante questo periodo, le oscillazioni quantistiche del campo di energia dominante, detto *Inflatone*, sono cresciute fino a raggiungere scale cosmologiche. Da queste fluttuazioni primordiali sarebbe quindi iniziata l'evoluzione che ha portato alla formazione delle strutture che compongono il nostro Universo.
Grazie alle altissime risoluzioni raggiunte dalle moderne osservazioni, i set di dati raccolti rappresentano un banco di prova fondamentale per questa teoria, di cui, negli anni, sono state proposte innumerevoli versioni, che ancora attendono una verifica sperimentale. Una delle tecniche più efficenti per discriminare tra i diversi modelli è la misura della componente non Gaussiana del campo primordiale. L'osservabile più strettamente legato al campo di perturbazioni primordiale a cui abbiamo accesso, è la distribuzione in temperatura della *radiazione cosmica di fondo*. La misura della non-Gaussianità primordiale nella distribuzione in temperatura della Radiazione Cosmica di Fondo è la tecnica migliore per discriminare tra i diversi modelli inflazionari.
L'indicatore statistico più sensibile ad una eventuale non Gaussianità è il *bispettro*, $B_\Phi(k_1, k_2, k_3)$, ovvero la trasformata di Fourier del correlatore a tre punti. Purtroppo, le singole configurazioni del bispettro non possono essere rilevate, in quanto completamente dominate dalla varianza cosmologica. Inoltre, la complessità analitica di questo correlatore rende il suo calcolo e la sua analisi numerica una notevole sfida computazionale. Per superare questi problemi, i modelli di bispettro vengono costruiti in modo che l'informazione sulla componente non gaussiana sia contenuta in un solo parametero, f_{NL}, che viene quindi derivato dall'integrazione su tutte le possibili configurazioni del bispettro. Il contributo derivante dalle diverse configurazioni viene definito attraverso la *shape function*, la cui forma dipende dal modello teorico sottostante. Inoltre, per diminuire il tempo computazionale richiesto, il bispettro deve essere scritto in forma fattorizzata nelle frequenze spaziali k_1,k_2 e k_3, in modo da abbassare il costo computazionale da $\mathcal{O}(\ell_{max}^5)$ a $\mathcal{O}(\ell^3)$.
Diverse teorie inflazionarie, inoltre, prevedono che il parametro di non-Gaussianità primordiale, f_{NL}, vari in funzione della scala spaziale delle oscillazioni. La dipendenza di scala di f_{NL} è definita dal parametro n_{NG}. Porre dei limti alla dipendenza di scala del bispettro, può fornire informazioni completamente nuove sui processi fisici che entrano in gioco ai livelli di energia raggiunti nell'Universo primordiale ($\sim 10^{15}\, GeV$), assoluta-

mente inaccessibili anche per i più moderni acceleratori di particelle.
Tuttavia, finora non era ancora stata sviluppata una forma separabile ed analiticamente esatta per bispettri con dipendanza di scala, necessaria per una corretta analisi dei dati ad altissima risoluzione resi disponibili dalle moderne missioni, come il satellite *Planck*.
In questo lavoro abbiamo ricavato una forma fattorizzabile ed analiticamente esatta per il parametro d'ampiezza f_{NL}. Grazie a questa parametrizzazione è possibile studiare la dipendenza di scala di *ogni* modello di bispettro fattorizzabile esistente in letteratura, attraverso algoritmi più veloci ed accurati per la previsione e l'analisi.
Abbiamo quindi sviluppato tutto l'apparato computazionale necessario per calcolare bispettri con dipendenza di scala e per stimare l'efficienza delle moderne *surveys* cosmologiche nel porre vincoli sui valori di f_{NL} ed n_{NG}.
Come prima applicazione, abbiamo studiato il bispettro della distribuzione in temperature della Radiazione Cosmica di Fondo attraverso un'analisi basata sulla matrice di Fisher. Per ottenere una conferma della validità dei nostri metodi, abbiamo preso in considerazione un esperimento ideale che riproducesse la sensibilità di WMAP (risoluzione angolare 12 minuti d'arco, corrispondenti ad un ordine di multipolo massimo $\ell_{max=500}$ nella nostra analisi), ottenendo risultati compatibili con quelli presenti in letteratura.
Questa tesi è organizzata come segue. Nel Primo capitolo si può trovare una breve introduzione sulle teorie che stanno alla base della moderna Cosmologia, dove viene posta particolare attenzione all'Inflazione ed alle implicazioni di questa teoria. Nel Secondo capitolo vengono descritte le caratteristiche delle anisotropie della Radiazione Cosmica di Fondo e la fisica che le governa. Nel Terzo capitolo definiamo il bispettro primordiale, in che modo sia legato al bispettro angolare della Radiazione Cosmica di Fondo, e definiamo il formalismo usato nella trattazione di questi argomenti. Nel Quarto capitolo esponiamo la procedura analitica che ha portato allo sviluppo di una fattorizzazione con dipendenza di scala per f_{NL}. Nel Quinto capitolo, dopo una breve digressione sul quadro statistico *Bayesiano*, mostriamo i risultati della nostra analisi numerica. Infine, il Sesto capitolo è dedicato ad ulteriori discussioni ed alle conclusioni.

Abstract

The *Theory of Inflation* is a cornerstone of modern Cosmology, as it both overcomes several important limits of the hot Big Bang scenario and provides a mechanism for the generation of primordial cosmological perturbations. Large experimental efforts are thus ongoing to test Inflation by means of large cosmological datasets.
The best observable to test initial conditions, supposedly set by Inflation, is the *Cosmic Microwave Background*. Measurements of primordial *non-Gaussianity* have in particular been shown to be a very powerful tool to discriminate between different Inflationary models. The statistic most sensitive to a non-Gaussian signal is the three-point correlator in Fourier space, namely the *bispectrum*.
Unfortunately, the bispectrum signal predicted by Inflation is expected to be very small, making a single bispectrum configuration undetectable even by an ideal completely noiseless experiment, due to the intrinsic Cosmic Variance limitations. Furthermore, the analytical complexity of this correlator makes its computation and analysis a significant numerical challenge.
These problems are overcome compressing all the non-Gaussian information in a single parameter, f_{NL}, obtained integrating over all the possible bispectrum configurations, weighted by a *shape function*. To decrease the computational time, and to make bispectrum analysis feasible, is absolutely needed to write the bispectrum in *factorized* form, *i.e.* as a linear combination of products of three one-dimensional functions, each depending by a single perturbation wavenumber. It can in fact be shown that the use of factorized bispectra allows to reduce the computational cost from $\mathcal{O}(\ell_{max}^5)$ to $\mathcal{O}(\ell_{max}^3)$.
The primordial non-Gaussian parameter f_{NL} is predicted to be scale-dependent in several Inflationary models. Putting constraints on the running parameter, n_{NG}, will provide new information about the Physical processes taking place in the very early Universe.
However, a separable form for a scale-dependent bispectrum did not yet exist. In this work, starting from an ansatz for a scale-dependent amplitude, we develop a factorizable form for the amplitude parameter f_{NL}. Our parametrization is analitically exact, and it allows to compute a separable scale-dependent form for *every* bispectrum shape existing in the literature.
This form permits faster and more accurate algorithms for forecasting and analysis. We develop a complete set of numerical tools to compute scale-dependent bispectra and to estimate the efficiency of modern surveys to constrain the non-Gaussian amplitude and its scale-dependence.
As an initial application of our result, we perform a Fisher matrix analysis of the bispectrum of the CMB temperature field and and we derive forecasts on f_{NL} and on the

running parameter n_{NG} for a WMAP-like experiment (angular resolution 12 arcmin. corresponding to a maximum multipole $\ell_{max} = 500$ in the analysis).
This thesis is organized as follows. In the first chapter, we make a brief introduction about the main theoretical aspects of modern Cosmology, with special attention to the Inflationary theory and its implications. In the second chapter we give an overview of the main the features of CMB anisotropies and the underlying Physics. In the third chapter we define the primordial bispectrum, showing how it is related to the angular CMB bispectrum, and we define the formalism used to treat it. In the fourth chapter we expose our analytical results in the development of a scale-dependent factorization. In the fifth chapter, after a brief digression over the *Bayesian* statistical framework, we show the results of our numerical analysis. Finally the sixth chapter is devoted to further discussion and our conclusion.

Contents

List of Figures

Chapter 1

Theoretical Background

The first developments of what is now known as "the standard Cosmological model" trace back to the beginning of the last century, when the recently fomulated General theory of Relativity allowed the development of a complete and testable theory of the structure and the evolution of the Universe. The basis of this model are the so called *Cosmological Principle* and the expansion of the Universe. The former states that the Universe is homogeneous and isotropic on large scales, the latter derived form observations. The crucial piece of evidence in favor of Universe expansion is the observation that the galaxies recede from us at a velocity proportional to the distance. This is appreciable from the famous *Hubble diagram*, so named in honor of its discoverer Edwin Hubble. The resulting picture is a Universe homogeneous and isotropic, that expands starting from a initial state of high energy density, the so called Big Bang.
In this chapter we outline a brief overview of the standard cosmological model. We first illustrate the basis of modern Cosmology and then we address in more detail the issue of initial conditions and describe the basic concepts underlying the theory of Inflation.

1.1 The Standard Cosmological Model

The Standard Cosmological Model, also known as "Hot Big Bang" model, assumes a Homogeneous and Isotropic Universe in constant expansion.
In 1929 Edwin Hubble found the relation between the distance of galaxies and redshift z called *Hubble Law*:

$$z = \frac{H_0 d}{c}, \tag{1.1}$$

where H_0 is the so called *Hubble constant*. The redshift is the shift of the photons wavelength to the red end of the spectrum due to the recession of galaxies from us

$$z = \frac{\lambda_{obs} - \lambda_{emit}}{\lambda_{emit}} \simeq \frac{v_{rec}}{c}, \tag{1.2}$$

where the relation between redshift and velocity applies only for low redshift. The Hubble law states so that the galaxies are receding from us with velocity that increase linearly with distance with a slope given by H_0. The original Hubble diagram is showed in figure 1.1.

General relativity allows us to extrapolate the expansion backwards in time. This yields to the conclusion that the Universe evolved from a state in which energy density diverges to infinite. The term "Big Bang" refers to this initial singularity and to the following hot phase in which the Universe expanded while dramatically cooling down.
It was in this moment that part of the chemical composition of the Universe was established. The atomic nuclei are predicted to form when the temperature fell below $\sim 0.1MeV$ during the so called "Big Bang Nucleosynthesis" (BBN from now). From the condition of nuclear statistical equilibrium it is possible to derive the expected abundances of the nuclei formed. The theoretical predictions depend on the combined density of protons and neutrons, which, in Cosmology, is called "baryon density". Thus BBN allows to measure the primordial baryon density, as well as the relative abundances of several light elements. These predictions are consistent with observational measurements of light elements, obtained for example with the analysis of distant Quasar spectra. This consistency provides one of the main confirmation of the Big Bang models.
But the evidences of an early hot phase are not exhausted with elements abundance. The photons that, in equilibrium with matter, formed this primordial plasma are still observable today as a diffuse background of black-body radiation, the *Cosmic Microwave Background* (from now CMB). The predictions of elements abundance and of CMB represent the great successes that allowed the Hot Big Bang model to establish itself as the Standard Cosmological Model.
It was however soon realized that a simple Universe filled with standard matter could not explain a vast range of observations, like rotational curves of galaxies and gravitational lensing from distant clusters. The observations reveal many inconsistencies between the distribution of luminous matter and the gravitational potential. In order to explain this we need to introduce a new "Dark Matter" component (DM) that doesn't interact directly with matter and radiation but contributes to the gravitational potential. In other words, DM feels gravitational interactions, but does not interact electromagnetically.
Moreover recent measurements of the expansion rate using the supernovae Ia as standard candles led to the identification of another new component: Dark Energy. This is the dominating component and it is supposed to be the source of the late time acceleration in the expansion rate.
A further extension of the standard model comes from the Inflationary theory that we will study in more detail in section (1.3).

1.1.1 The Cosmological Principle

The Cosmological Principle is the foundation of modern Cosmology. It is an extension of the Copernican Principle stating that the Earth is not in a particular position in the space. Together with the observed isotropy it leads to the assumption of homogeneity.
Today we have evidences of homogeneity and isotropy on large scales, but it's interesting to notice that the Cosmological Principle was introduced without any observational justification. It seemed essential, to the formulation of a concrete theory, to assume a basic simplicity to the global structure. The inspiration came from the ideas of Ernst Mach that the inertia is related with the distribution of matter on large scale: since the inertial mass remains constant everywhere the distribution of matter shall be homogeneous. This is one of the suggestions that brought Einstein to assume that the nature

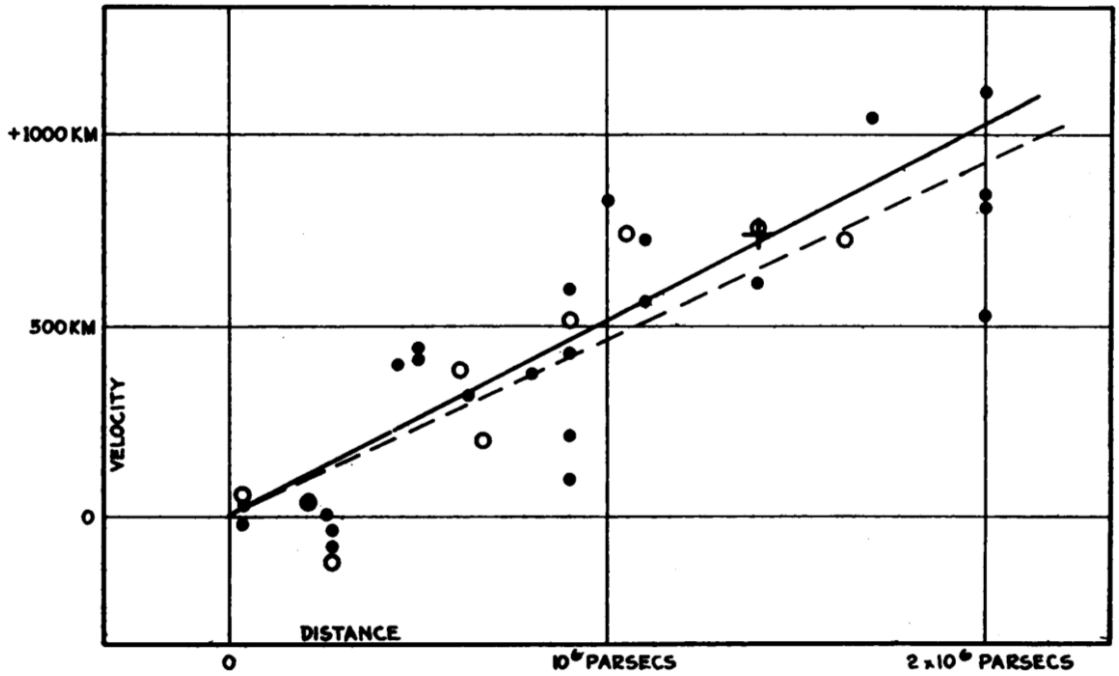

Figure 1.1: The original Hubble diagram [27], the ordinate axis represents the velocities (unit should be [KM/sec]) and the abscissa are the distance (unit should be [Mpc]). The filled point are corrected for the Sun's motion, while the open ones are not. The solid line is the best fit to the filled point and dashed line is the best fit to the open ones.

of space-time is strictly bounded with the matter distribution. Mach's vision was never verified, but general relativity, together with the Cosmological Principle, proved to be the right path toward a simple and concrete theory.
In fact the Cosmological Principle was present in various form in all the cosmological theories born in the last century, from the Big Bang to the Steady State Cosmology.

1.1.2 Friedmann-Lemaître-Robertson-Walker Metric

The Einstein equations describe gravitation as a result of the relation between the energy density and the geometry of space-time. The geometric properties are described by the *metric* tensor that defines how coordinates are related to physical distance.
First of all we must emphasize that the Cosmological Principle is valid only if we consider all the Universe at the same instant. The geometrical interpretation then implies that space, but not space-time, must be maximally symmetric. Since a symmetry corresponds to a conservation rule, a 3 dimensional space must be invariant under both translation and rotations to agree with the cosmological principle.
The Friedmann-Lemaître-Robertson-Walker metric (FLRW from now) describes a 4-dimensional space-time admitting an infinity of 3-dimensional subspaces maximally sym-

Parameter	Ω_m	Ω_Λ	$\Omega_b h^2$	H_0	z_*	Age[Gyr]
Planck	0.3175	0.6825	0.022068	67.11	1090.43	13.819

Table 1.1: Best fit values for some cosmological parameters estimated by *Planck* Surveyor [38]

metric. Therefore, using the signature $(-,+,+,+)$, the FLRW metric tensor is:

$$g_{\mu\nu} = \begin{pmatrix} -1 & 0 & 0 & 0 \\ 0 & a^2(t) & 0 & 0 \\ 0 & 0 & a^2(t) & 0 \\ 0 & 0 & 0 & a^2(t) \end{pmatrix}. \tag{1.3}$$

Here we use *comoving coordinates*: the metric is free of time-space cross-terms so the space components are proportional to a single function of t. The result is that a physical point keeps the same spatial coordinates at any time. The expansion is quantified by the scale factor $a(t)$, whose present value is set to one. It allows to pass from *comoving distance*, that remains constant in the expansion and measures the difference between coordinates, to physical distance that grows in time. A maximally symmetric space will be certainly spherically symmetric, so the line element is usually defined in spherical coordinates giving:

$$\mathrm{d}s^2 = -\mathrm{d}t^2 + a^2(t)\left[\frac{\mathrm{d}r^2}{1-kr^2} + r^2(\mathrm{d}\theta^2 + \sin^2\theta \mathrm{d}\phi^2\right]. \tag{1.4}$$

This leads to the definition of the parameter k. It describes the *curvature* of space-time: the case $k = 0$ corresponds to a flat space with no curvature ; $k = 1$ corresponds to a positive curvature, or to an closed space; $k = -1$ corresponds to a negative curvature and to a open space.
With the metric we can compute the Ricci tensor $R_{\mu\nu}$ and the Ricci scalar R and then write down the Einstein equation:

$$R_{\mu\nu} - \frac{1}{2}g_{\mu\nu} = 8\pi G T_{\mu\nu}, \tag{1.5}$$

where $T_{\mu\nu}$ is the *energy momentum tensor*, in our case we consider a perfect fluid:

$$T_{\mu\nu} = \begin{pmatrix} -\rho & 0 & 0 & 0 \\ 0 & P & 0 & 0 \\ 0 & 0 & P & 0 \\ 0 & 0 & 0 & P \end{pmatrix}, \tag{1.6}$$

here ρ is the energy density and P is the pressure for unit of surface of the fluid. The energy density can be expressed in function of the density of each component $\rho = \rho_m + \rho_\Lambda + \rho_\gamma + \rho_\nu$ where the subscript m indicates the matter density, Λ the Dark Energy density, γ the photons density and ν the neutrinos. The matter density term contains both baryon and Dark matter contribution $\rho_m = \rho_b + \rho_{DM}$. From the solution of 1.5 (for further details see appendix A or [14] for a complete discussion) comes the

Friedmann equations:

$$\left(\frac{\dot{a}}{a}\right)^2 = \frac{8\pi G}{3}\rho - \frac{k}{a^2} \tag{1.7}$$

$$\frac{\ddot{a}}{a} = -\frac{4\pi G}{3}(\rho + 3P). \tag{1.8}$$

Equation (1.7) defines how rapidly the scale factor changes, this is called *Hubble rate*:

$$H(t) = \frac{1}{a}\frac{\mathrm{d}a}{\mathrm{d}t} \tag{1.9}$$

the most important fact is that it is relate to the energy density, the measurement of the Hubble rate provide precious information about the history of the Universe. The Hubble rate's value at present time is the Hubble constant that appears in equation (1.1).
The composition of the Universe is defined in relation to the critical density ρ_c by the density parameter Ω.

$$\rho_c = \frac{3H^2}{8\pi G}, \tag{1.10}$$

$$\Omega = \rho\frac{8\pi G}{3H^2}. \tag{1.11}$$

Rewriting (1.7) it's trivial to understand the meaning of critical density:

$$\Omega - 1 = \frac{k}{H^2 a^2}. \tag{1.12}$$

ρ_c is then the density for which the Universe is spatially flat. The relation between the curvature and the energy content of the Universe can be summarized as:

$$\begin{array}{lcccccc} \text{Open} & \leftrightarrow & k = -1 & \leftrightarrow & \Omega < 1 & \leftrightarrow & \rho < \rho_c \\ \text{Flat} & \leftrightarrow & k = 0 & \leftrightarrow & \Omega = 1 & \leftrightarrow & \rho = \rho_c \\ \text{Close} & \leftrightarrow & k = 1 & \leftrightarrow & \Omega > 1 & \leftrightarrow & \rho > \rho_c \end{array} \tag{1.13}$$

Current experiments suggest a total density very close to ρ_c, that is $\Omega = \rho/\rho_c \simeq 1$. The most recent measurements of the density composition and other parameters are shown in table (1.1).

1.1.3 The Cosmic Microwave Background

The detection of the CMB by Penzias and Wilson in 1965 set the milestone for the affirmation of the Big Bang as standard cosmological model. The CMB was predicted for the first time by Gamow in the 40s as the natural consequence of an expanding Universe; whereas it is totally incompatible with a steady state Universe.
Actually the controversy was not immediately decided. The CMB is the relic of the hot ancient Universe, coming from an epoch in which radiation and matter were tightly coupled by the Compton and Coulomb scattering with free electrons, forming the so called *photon-baryon fluid* [35]. Being emitted in a condition of high equilibrium the

CMB photons were expected to possess a black-body spectrum. However it was very difficult for the time to avoid atmospheric absorption and measure the spectrum with the required narrow accuracy. Finally in the 90s the COBE spacecraft, with its spectrophotometer FIRAS, measures the most perfect black-body spectrum in nature, with a temperature of $2.753 \pm 0.002K$, showed in figure 1.2. Furthermore, measurement of its color temperature shows that it is extraordinarily uniform over the whole sky providing strong evidence for large scale isotropy.
The CMB photons scatter the last time at the epoch called *recombination* [34][58][42]. Recombination signs the moment in which neutral hydrogen began to form lowering the number of free electrons. Before recombination due to the high temperature electrons could not bind to the nuclei to form neutral atoms, in this early times the free electrons gave an high contribution to the optical depth via Compton scattering. When the temperature was lowered enough to allow the formation of the first atoms the number of free electrons fell down; without their contribution optical depth fell down too and radiation and matter decoupled. The matter began to cluster, forming the structure we observe today, while the photons were free to travel through space with nearly no interactions, giving rise to a diffuse electromagnetic signal of Cosmological origin, hence the name, that we already been using, of "Cosmic Microwave Background". Looking at the CMB we see the image of a spherical section of this primordial photon-baryon fluid just after the decoupling, this is the so called *Last Scattering Surface*. It is like to see a snapshot of a section of the primordial plasma taken at the recombination. From the statistical mechanics we know that photons decoupling occurred when the temperature of the Universe was $\sim 3000\,K$. The intensity of the radiation emitted by a gas of photon with a blackbody spectrum follows the Planck distribution:

$$I_\nu = \frac{4\pi\hbar\nu^3}{c^2}\left[\exp\left(\frac{2\pi\hbar\nu}{k_B T}\right) - 1\right]^{-1}. \tag{1.14}$$

The energy density of uniform blackbody radiation is defined by:

$$\rho_\gamma = 2\int \frac{\mathrm{d}^3 p}{(2\pi)^3}\frac{1}{e^{p/T}-1} = \frac{\pi^2}{15}T^4, \tag{1.15}$$

were p is the momentum of the photons. The evolution of energy can be computed from the conservation law for the energy momentum tensor (1.6):

$$\nabla_\mu T^\mu_{\ \nu} = \partial_\mu T^\mu_{\ \nu} + \Gamma^\mu_{\alpha\mu} T^\alpha_{\ \nu} - \Gamma^\alpha_{\nu\mu} T^\mu_{\ \nu} = 0, \tag{1.16}$$

considering the $\nu = 0$ component, and computing the connection (A.2) for the FLRW metric, we have the conservation law in an expanding universe:

$$\frac{\partial\rho}{\partial t} + H[3\rho + 3P] = 0. \tag{1.17}$$

The radiation pressure is $P_\gamma = \rho_\gamma/3$, so that (1.17) gives $\rho_\gamma \propto a^{-4}$, this implies that the temperature scales as a^{-1}. We can so compute the growth of the scale factor from the recombination to our day. Since the CMB temperature decreased by about a factor ~ 1100, $a(t)$ should be increased equally, consistently with the expansion of the Universe.

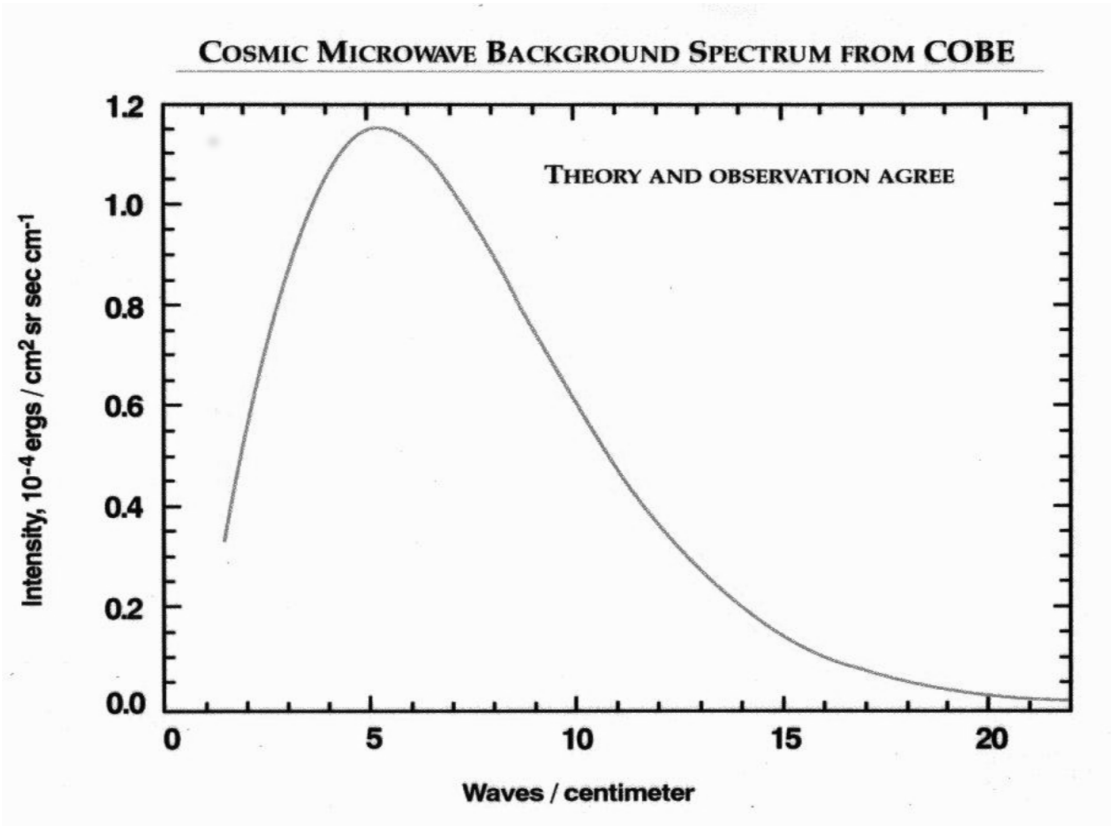

Figure 1.2: CMB spectrum taken by FIRAS spectrophotometer from COBE spacecraft [32]. The agreement between blackbody curve and observations is so hight that the measured points ad the error bars disappear under the theoretical curve.

The redshift of the CMB photons can easily be computed by applying the Wien law, it is so:

$$z = \frac{\lambda_{max}^{obs} - \lambda_{max}^{*}}{\lambda_{max}^{*}} = T_* \left(\frac{1}{T} - \frac{1}{T_*} \right) \simeq \frac{T_*}{T} \simeq 1100, \tag{1.18}$$

were $*$ indicates the values at recombination.
As we said the CMB is extremely uniform, but at a sensitivity level of about one part in 1000 of the total intensity a dipolar anisotropy can be observed. It is naturally attributed to the kinematic Doppler effects associated with the Earth's motion through a reference frame in which the radiation is at rest. This allows to compute the peculiar motion of our galaxy with respect the cosmic reference frame. The result is $v \simeq 600\, Km/s$ in direction of the constellation of Hydra Centaurus, in the same direction of the other galaxies of our group.
Observations with a sensitivity of 10^{-5} part of the total intensity opens new scenarios in the study of the CMB: since they show the presence very small anisotropies. These anisotropies are the result of gravitational fluctuations on the last scattering surface and their origin cannot be explained by the Standard Cosmological Model. The large scale structure we observe today nearly certainly originated from these little perturbation. The most accredited theory to explain the origin of these anisotropies is Inflation we

will describe in the next section.

1.2 Perturbations Power Spectrum and Random Fields

In this section we briefly review some key elements of the formalism used to describe cosmological perturbations, that will be widely used in the following. With this aim we introduce the concepts of *random field* and of perturbations *Power Spectrum*.
We have seen that the expansion history of the Universe, as well as is curvature, depends on the evolution of the energy density of different components: matter radiation and cosmological constant. These density fields are homogeneous in the background FLRW model, so its natural to describe them as:

$$\rho(x,t) = \rho(t) + \delta(x,t) \tag{1.19}$$

where $\rho(t)$ represents the background density and $\delta(x,t)$ is the density perturbation field, representing small deviations from homogeneity. In the standard Cosmological scenario we always assumed that the density of different components presents small initial fluctuations over its smooth background value, that later on grow via gravitational instability, forming all the structures we see today in the Universe. Of course this opens the problem of explaining where these initial perturbations came from. As we will see better in the next section, the most accredited explanation of the origin of perturbation is the so called *theory of Inflation*. In this scenario, as we will specify later, the perturbation field is intrinsically stochastic, non-deterministic; as we will see in the next section the reason lies in the Heisenberg's Uncertainty Principle obeyed by the quantum processes that at very early times generated the perturbation.
Since $\delta(x,t)$ is a random field, we cannot make deterministic predictions about one specific realization. What we can do is to make a statistical description of the Universe; taking a CMB related example, we can predict *e.g* how many hot and cold spot there are *on average*, and the expected fluctuation of this number, but we cannot tell *exactly* how many of them we are going to see, and where they are going to be located in our observed universe.
In other words, and more precisely, when we say that the perturbations are random fields we mean that for every position x_i at a given time t (wich we will omit to explicitly write from now)the quantity $\delta(x_i)$ is a random variable.
The value of a random variable cannot be predicted but we can associate to the variable the *probability density function* (PDF) $P_x(\hat{\delta})$. It quantifies the probability that the variable $\delta(x)$ takes a certain value $\hat{\delta}$ in a certain point x. Considering N points we define the joint probability $P_{(x_1 x_2 \dots x_N)}(\hat{\delta}_1, \hat{\delta}_2, \dots, \hat{\delta}_N)$ as the probability that in every point $\{x_1, x_2, \dots, x_N\}$ the random variable takes respectively the values $\{\hat{\delta}_1, \hat{\delta}_2, \dots, \hat{\delta}_N\}$.
The physical quantities described by random fields, as the Universe density distribution, are so defined by the statistical properties of the field. The statistical distribution of a random variable δ can be described through the *moments* of the PDF, which are the expectation value of the quantity:

$$\mu_k = \int \mathrm{d}\delta(x)\, [\delta(x) - \langle \delta(x) \rangle]^k P_x(\delta(x)). \tag{1.20}$$

Following a most common notation we define the first 4 moments as

$$\mu_1 = \mu = \langle \delta(x) \rangle \qquad \text{Average} \tag{1.21}$$

$$\mu_2 = \sigma^2 = \langle \delta^2(x) \rangle - \langle \delta(x) \rangle^2 \qquad \text{Variance} \tag{1.22}$$

$$\mu_3 = \int \mathrm{d}\delta(x) \, [\delta(x) - \langle \delta(x) \rangle)]^3 P_x(\delta(x)) \qquad \text{Skewness} \tag{1.23}$$

$$\mu_4 = \int \mathrm{d}\delta(x) \, [\delta(x) - \langle \delta(x) \rangle)]^4 P_x(\delta(x)) \qquad \text{Kurtosis} \tag{1.24}$$

Furthermore if the random variables are more than one, as it happens when we consider random fields, which are collections of random variables, we can define the *correlation function* $\xi(r)$ and the *covariance*, for example taking the density perturbation in x and in $x + r$:

$$\xi(r) = \langle \delta(x) \delta(x + r) \rangle \tag{1.25}$$

$$\mathrm{cov}(\delta(x), \delta(x + r)) = \langle \delta(x) \delta(x + r) \rangle - \langle \delta(x) \rangle \langle \delta(x + r) \rangle. \tag{1.26}$$

Given N variables we can define the *covariance matrix*: it is a $N \times N$ matrix that quantifies the covariance for every combination of variable.
The most important characteristic of cosmological density perturbations, inherited, as we will see, from quantum fluctuations, is their *Gaussianity*. Gaussian distribution is:

$$P(x) = \frac{1}{\sqrt{2\pi\sigma}} \exp\left[-\frac{(x - \mu)^2}{2\sigma^2} \right], \tag{1.27}$$

from this definition we can note that the Gaussian distribution is completely defined by the first two moments: the average μ and the variance σ^2. The higher ones are null if odd ($\mu_3, \mu_5 \dots$) while the evens ones can be defined as powers of σ.
The energy density of the different cosmological components Universe is thus described, for each components, by a "random Gaussian scalar field". This allows us to totally describe it with its *Power Spectrum*. In fact the power spectrum is, as we will shortly see, the analogous for random fields to what the variance is for random variable. As a Gaussian random variable is entirely described by average and variance, a Gaussian random field will entirely be defined by its power spectrum. To define the power spectrum we start taking the Fourier transform of the field:

$$\delta(x) = \int \frac{\mathrm{d}^3 k}{(2\pi)^3} \, \delta(k) e^{ik \cdot x}, \tag{1.28}$$

the perturbation in real space is a random variable, then, so is its Fourier transform. Furthermore, since the field is stationary and isotropic, the covariance matrix in Fourier space is diagonal, and its elements are defined as:

$$\langle \delta(k) \delta(k') \rangle = (2\pi)^3 P_\delta(k) \delta_D(k - k'), \tag{1.29}$$

where $P_\delta(k)$ is the perturbation Power Spectrum: it is defined as the diagonal elements of the covariance matrix of the perturbation in Fourier Space and, if the perturbation

field is Gaussian, the Power Spectrum entirely defines it.
The *Wiener-Khintchine theorem* states that the Power spectrum is the Fourier transform of the correlation function:

$$\xi(r) = \int \frac{\mathrm{d}^3 k}{(2\pi)^3} P_\delta(k) e^{ik\cdot r}. \tag{1.30}$$

The Power Spectrum is directly related to variance of the field:

$$\sigma^2 = \int \frac{\mathrm{d}^3 k}{(2\pi)^3} P_\delta(k), \tag{1.31}$$

the variance of the field is so defined by the three dimensional integral on all scales k of the Power Spectrum. Before concluding this short digression on random fields, we would like to stress that, whereas here we have stressed Cosmological perturbation as Gaussian fields, in the following of this thesis we will focus our attention on non-Gaussianity. This apparent contradiction is due to the fact that some degree of non-Gaussianity is allowed by theories of primordial Inflation, but is expected to be always very small. So to study the evolution of the Universe, formation of structure, and cosmological parameters, we can safely work assuming that everything is Gaussian. On the other hand, detecting a tiny primordial non-Gaussian component in itself would be hugely important, as it could shed light on the Physics of the Early Universe. This will clarified and studied in more details in chapter 3

1.3 Inflation

As it often happens in science, the great discovery of the CMB opened a number of new questions about the formation of our Universe. As we saw, the Standard Cosmological Model does not explain the origins if the little temperature anisotropies, but there is an even most evident problem. One of the main issues is the impressive level of uniformity of the CMB sky; this is a wonderful proof of the Cosmological principle but, on the other hand, is a fact rather difficult to justify.
To better understand this issue we have to introduce the concept of *comoving horizon* η. The comoving horizon is the maximum comoving distance traveled by light since the beginning of the Universe. Obviously, for two regions to communicate, they should be at a comoving distance smaller than the comoving horizon. If they aren't, they cannot have exchanged any information.
If recombination happened $\sim 380,000\,\mathrm{yr}$ after the Big Bang, as the model predicts, and the Universe was radiation dominated, the size of comoving horizon at that time subtends a very small angle from our point of view. Furthermore, as we will see treating CMB anisotropies in the next chapter (section 2.2.1), the CMB temperature Power Spectrum provides accurate information about the size of causally connected regions at the recombination, resulting in an estimate of $\sim 2^\circ$.
Despite this, the CMB appears to be thermalized at all angular scales, so physical processes must have acted on all scales in order to allow the Universe to reach an equilibrium state.
If this couldn't happen, how can all the sky appear to have been in thermal equilibrium,

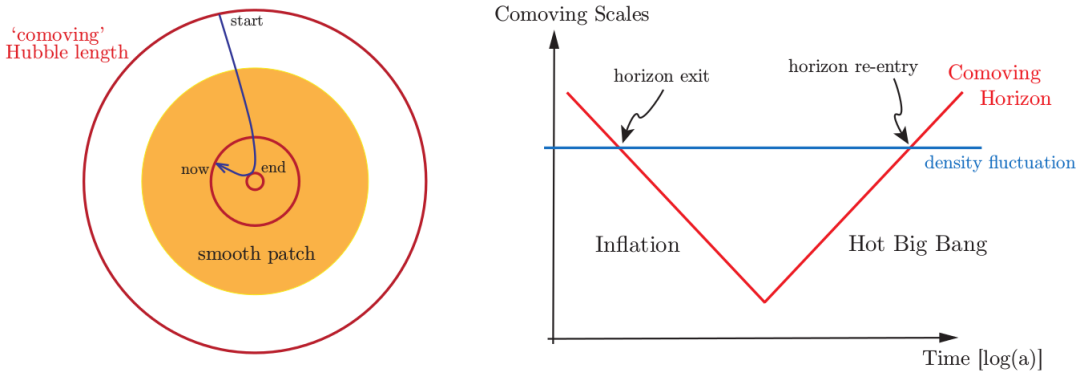

Figure 1.3: Evolution of Hubble radius in an inflationary Universe. The left figure shows the Hubble sphere before and after Inflation, and how it is now, still inside the smooth patch. The right panel shows how Inflation solves the horizon problem. All scales that are relevant to cosmological observations today were larger than the Hubble radius until $a \sim 10^{-5}$. However, at sufficiently early times, these scales were smaller than the Hubble radius and therefore causally connected. Image taken from [7].

when it couldn't even be considered a single thermodynamic system? This apparent impasse is the so called *Horizon Problem*, a possible explanation to this problem comes from *Inflationary theory*. As we will see, this theory can also explain even the origin of the inhomogeneities.
Inflation states that, at very early times, the Universe underwent a period of accelerated expansion. To understand how this can solve the horizon problem, it is more illuminating to reason in terms of *Hubble radius* instead of comoving horizon. Acceleration implies $\mathrm{d}^2a/\mathrm{d}t^2 > 0$, that is:

$$\frac{\mathrm{d}^2 a}{\mathrm{d}t^2} = \frac{\mathrm{d}}{\mathrm{d}t}\left[a\frac{1}{a}\frac{\mathrm{d}a}{\mathrm{d}t}\right] = \frac{\mathrm{d}}{\mathrm{d}t}\left(\frac{1}{aH}\right)^{-1} > 0. \tag{1.32}$$

The quantity $1/aH$ is the Hubble radius: it is the physical distance a particle can travel in one expansion time. It is related to the comoving horizon by the equation:

$$\eta = \int_0^a \frac{\mathrm{d}a'}{a'}\frac{1}{Ha'}. \tag{1.33}$$

The difference between the two is that regions farther than η never could have communicated in the past (*i.e*, from t=0 up to today) whereas if they are at distance grater than $1/aH$ they aren't connected only at given time. From (1.32) we see that the consequence of an accelerated expansion is the decrease of the Hubble radius, as it's shown in the right panel of figure 1.3. Different region of the CMB, thus, are effectively not connected at the recombination, but only in terms of Hubble radius. The comoving horizon instead grew together with the scale factor, so that it was bigger than the last scattering surface yet at the recombination. If Inflation succeed, zones outside the Hubble radius at recombination can have been causally connected at the early times in which they thermalized, as it can be seen in the left panel in figure 1.3. Quantitatively, to solve the

horizon problem, during Inflation the Universe must have expanded over approximately 28 orders of magnitude [19].
Once it's proven that Inflation can provide solutions to these inconsistencies, the following step is to define what type of energy is needed to produce it. The second Friedmann equation (1.8), under the condition (1.32) gives $(\rho + 3P) < 0$, so Inflation requires:

$$P < -\frac{1}{3}\rho. \tag{1.34}$$

The energy density ρ is positive, so the the pressure must be negative. We don't know any type of ordinary matter that has a negative pressure. We have to suppose that what drives Inflation is some kind of field arising at the high energy scale of the primordial Universe. Objects with the required properties can indeed be found in the high energy extension of the Standard Model of Particle Physics.

1.3.1 The Cosmological Flatness Problem

Before proceeding with our discussion, is interesting to note another aspect of our Universe that the Standard Cosmological Model doesn't explain: that is its *flatness*. In the previous section (equation 1.12) we showed how the geometry of the Universe is strictly related to its energy content ρ. Nowadays we know, from various measurements, that the value of density parameter $\Omega_0 = \rho/\rho_c$, at our time, is very close to 1. $\Omega = 1$ corresponds to a flat Universe, every deviation from this value, even if very small, involves a certain degree of curvature.
However, the studies of the Friedman equation (1.7) in proximity of the initial singularity lead to disturbing conclusions. This equation can be rearranged as:

$$(\Omega^{-1} - 1)\rho a^2 = \frac{3kc^2}{8\pi G} = \text{const.}\,, \tag{1.35}$$

since the right hand side of this equation is constant, and in a radiation dominated Universe the energy density decreases more quickly than a^2 increases, we expect that the factor $(\Omega^{-1} - 1)$, representing the deviation from flatness, increases in time. A full calculation (see e.g. [12] for a full derivation) lends to the conclusion that the factor $(\Omega^{-1} - 1)$ must be increased of ~ 60 order of magnitude from the initial singularity until now. This involves that,in order to to agree to current measurements, the initial value of the density parameter had to depart from 1 by less than one part in 10^{60}!
This kind of problems are called *fine tuning problems*: if we consider the early Universe to be radiation dominated we discover that the probability that it survives so long are incredibly small, because the range of Ω value for which our Universe exists is 1 ± 10^{-60}.
The solution comes from the fact that, during the Inflationary epoch, the scale factor grew exponentially; meanwhile, as we shall see in the next section, the energy density of the Inflaton field, that dominates the expansion, remained roughly constant. Following equation (1.35), this implies that the factor $(\Omega^{-1} - 1)$ decreased equally during the same period.
Thus if $|\Omega^{-1} - 1|$ initially takes any arbitrary value, a period of Inflation can force it down towards 0 and leave it extremely small, around 10^{-62} as required above, for example. Subsequent evolution of the universe will cause the value to grow, bringing

it to the currently observed value of around 0.01. In this way, thanks to Inflation, the sensitive dependence on the initial value of Ω has been removed.

1.3.2 Primordial Potential

At early time the energy density of the Universe reached incredibly high levels, about $10^{15} GeV$ when $\sim 10^{-37}\, s$ passed from Big Bang. This energy is 9 order of magnitude above the limits of modern particle accelerators. Physics in this range of energy is, from an experimental point of view, still unexplored. If Inflation occurred, the more reasonable explanation seems that it was driven by one or more quantum scalar fields, called *inflaton*, arising at these scales.
In order to understand how a scalar field component can produce acceleration in the expansion rate, we have to take a look at the Einstein equations. Let us start by considering the energy momentum tensor of a homogeneous scalar field $\psi(t)$, for now we neglect the first order perturbation $\delta\psi(x,t)$, so we have

$$T^{\alpha}_{\ \beta} = g^{\alpha\nu}\frac{\partial\psi}{\partial x^n u}\frac{\partial\psi}{\partial x^{\beta}} - g^{\alpha}_{\ \beta}\left[g^{\mu\nu}\frac{\partial\psi}{\partial x^{\mu}}\frac{\partial\psi}{\partial x^{\nu}} + V(\psi)\right], \tag{1.36}$$

were $V(\psi)$ is the potential of the field and for the metric we used the signature $(-,+,+,+)$. Since the field is homogeneous we consider only the time derivative, the time-time component for a perfect isotropic fluid is $T^0_{\ 0} = -\rho$:

$$\rho = \frac{1}{2}\left(\frac{\mathrm{d}\psi}{\mathrm{d}t}\right)^2 + V(\psi), \tag{1.37}$$

and the space-space component, which represent the pressure, gives:

$$P = \frac{1}{2}\left(\frac{\mathrm{d}\psi}{\mathrm{d}t}\right)^2 - V(\psi). \tag{1.38}$$

The first of these equations shows that the dynamic of a scalar field is totally analogue to that of a single particle moving in a potential. The second tells us that a negative pressure requires more potential energy than kinetic. Little kynetic energy implies that the energy density and the potential remain nearly constant in time. From equation (1.7) it's clear that this condition produces the exponential expansion required to solve the horizon problem!
These assumptions form the basis for the simplest model of Inflation: the so called "single-field slow-roll" scenario [30] [3]. In the slow-roll picture, the scalar field is initially characterized by a very flat potential. This makes $V >> E_k$ in (1.37) and (1.38), thus producing the conditions for acceleration. Inflation ends when the field reaches the end of the plateau, and falls down into its ground state (*i.e* we have a transition from a "false vacuum" to a "true vacuum"), as shown in figure 1.4. At this point the field oscillates around the minimum, and decays into ordinary matter and radiation. Initial energy in the false vacuum state thus get converted into the various components of the cosmological fluid. This phase is called *reheating* and it sets initial conditions in the Standard cosmological Model.
The name *slow-roll* derives from the analogy with the dynamics of a classic point particle

rolling down a potential.
The equation governing the evolution of the field in an expanding Universe is:

$$\frac{\mathrm{d}^2\psi}{\mathrm{d}t^2} + 3H\frac{\mathrm{d}\psi}{\mathrm{d}t} + \frac{\mathrm{d}V(\psi)}{\mathrm{d}\psi} = 0. \tag{1.39}$$

During Inflation the Hubble rate remains nearly constant. Meanwhile the scale factor grows nearly exponentially, so its relation with conformal time can be simplified as:

$$\eta = \int_{a_e}^{a} \frac{\mathrm{d}a}{a^2 H} \simeq -\frac{1}{aH}. \tag{1.40}$$

The slow-roll model is usually characterized by the parameters:

$$\epsilon = -\frac{\dot{H}}{aH^2}, \tag{1.41}$$

$$\eta = -\frac{1}{aH\dot{\psi}}\left[3aH\dot{\psi} + a^2\frac{\partial V}{\partial \psi}\right], \tag{1.42}$$

that quantify how slowly the field is rolling. By definition, an Inflationary epoch has $\epsilon < 1$.
So far we have presented the zeroth order picture, this provides a good solution for the horizon problem but it doesn't explain the onset of the fluctuations. It has been shown that a perturbative expansion of the homogeneous scalar field may account for the initial power spectrum of perturbations [5][10][20][21][22][53]. We can express the field as:

$$\psi(\vec{x}, t) = \psi(t) + \delta\psi(x, t), \tag{1.43}$$

where the first term is the homogeneous part and the second represents the perturbation. The zeroth order part is responsible for the accelerated expansion, while the first order part induces perturbations on the metric. The existence of this perturbation component is unavoidable in quantum context, since indetermination principles imply small quantum fluctuations of the field, giving rise to this $\delta\psi$ term. From General Relativity we know that the density of matter and radiation is coupled to the scalar field perturbation (1.43). Therefore it is the scalar part that eventually provided the initial conditions for density fluctuations after reheating. Given the limited scope of this brief introduction, we omit here the full treatment needed to derive the power spectrum for the perturbative term (see *e.g.* [14] for a full calculation), and we simply outline the main aspects of the derivation.
The most common way is to derive the equation for $\delta\psi$ in a gauge[1] in which the scalar field is spatially decoupled from the density fluctuations, called *spatially flat slicing*. In this gauge the spatial part of the metric remains unperturbed. So the first order part of the inflaton scalar field can be directly derived from the conservation of the energy momentum tensor, leaving:

$$\ddot{\delta}\psi + 2aH\dot{\delta}\psi + k^2\delta\psi = 0, \tag{1.44}$$

[1] A gauge theory is a type of field theory in which the Lagrangian is invariant under a continuous group of local transformations. The terms *gauge* refers to the coordinate systems connected by these transformations. In General Relativity a gauge is defined by a specific choice ot the functional relation linking coordinates in the unperturbed background to coordinates in the perturbed space.

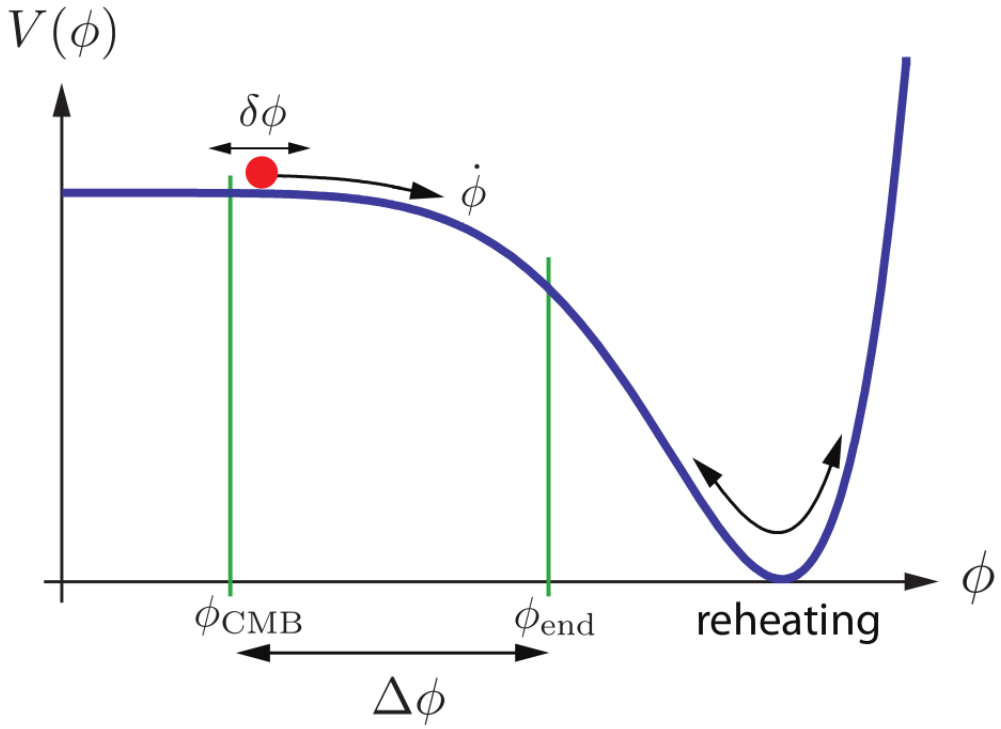

Figure 1.4: Inflation potential (the inflaton field is ϕ instead of ψ). ϕ_{end} indicates the point in which the kinetic energy equals the potential and the Inflation ends. CMB fluctuations are created at ϕ_{CMB} about 60 e-folds before the end of Inflation. At reheating, the energy density of the inflaton is converted into radiation. Image taken from [6].

were dots indicate derivatives with respect to conformal time. Given this equation, we have to find a gauge invariant variable[2] related to $\delta\psi$ in the flat slicing gauge and to the metric perturbation Φ in the conformal Newtonian gauge. Again, we will not formally define the Newtonian gauge here. It suffices to say for our purposes that, when perturbing the metric with this gauge choice, the perturbation variable Φ takes a clear Physical meaning: it is the Newtonian potential generated by the small fluctuation in the homogeneous background curvature.
Once we found a definition for the inflaton perturbation, and understand how it can be related to the density perturbation, we need to define their power spectrum, so that it can be compared with its observed counterpart. The choice of the power spectrum as observable is strictly related to the quantum nature of the field. If we rearrange (1.44) into the form of a harmonic oscillator and quantize it (for further details about the quantum harmonic oscillator see [37]) it's easy to define the variance of the operator that would represent the field. This is important because, in the simplest picture of the single scalar field, in consequence of their quantum mechanical origins, the fluctuations are Gaussian.
As we saw in section 1.2 Gaussian distribution is fully characterized by mean and variance. In our case the mean is 0 by definition (1.43), therefore its variance is sufficient

to totally define the field. The variance is related to the Power Spectrum by:

$$\langle|\delta\psi(\vec{x})\delta\psi(\vec{x}')|\rangle = (2\pi)^3 P_\psi(k)\delta^3(\vec{k}-\vec{k}'), \tag{1.45}$$

where $P_\psi(k)$ is the power spectrum. As we were saying above, being linked to the variance, the power spectrum fully defines the perturbations fields. It is thus a quantity of paramount importance in Cosmology.
Omitting a bit of mathematics, we leap to the definition of the spectrum in the spatially flat slicing gauge:

$$P_{\delta\psi} = \langle|\delta\psi|^2\rangle = \frac{H^2}{2k^3}. \tag{1.46}$$

The next step is to find the gauge invariant variable, in the flat slicing gauge it is:

$$\zeta = -\frac{aH}{\dot{\psi}}\delta\psi. \tag{1.47}$$

The power of this variable is thus related with (1.46):

$$P_\zeta = \langle|\zeta|^2\rangle = \left(\frac{aH}{\dot{\psi}}\right)^2 \langle|\delta\psi|^2\rangle = \left(\frac{aH}{\dot{\psi}}\right)^2 P_{\delta\psi}. \tag{1.48}$$

In the Newtonian gauge at the end of Inflation $\zeta = 3\Phi/2$, here Φ represent the gravitational potential fluctuation, finally we can define the power spectrum of the primordial Newtonian potential generated by density perturbations:

$$P_\Phi = \frac{4p_\zeta}{9} = \left.\frac{8\pi G H^2}{9\epsilon k^3}\right|_{aH=k}. \tag{1.49}$$

Observing equation (1.49) we see that Inflation produces a so called *scale-invariant* power spectrum, that is $P(k)k^3$ is constant. As we will see in detail in the next chapter, the CMB power spectrum is indeed nearly scale-invariant. A scale-invariant (or scale-free) spectrum is characterized by a constant logarithmic slope, physically this means that the process from which it derives acted in the same way at all scales. The little deviation from scale invariance, detected with a high degree of significance in recent surveys (*Planck* satellite), is also matching a specific prediction of Inflation, once corrections to the power spectrum in a slow-roll parameter expansion are accounted for. CMB observation thus provide an outstanding confirmation of the Inflationary paradigm.

1.3.3 Non-Gaussianity

Until now most predictions of Inflation passed the observational tests. The Universe appears to be remarkably flat, homogeneous and isotropic and the measured power spectrum is very near to the Harrison-Zel'dovich one.
However, the standard single-field slow-roll scenario briefly outlined above is not the only possible Inflationary model we can build. On the contrary, literally hundreds of models have been proposed in the literature, eventually involving different scalar fields potentials

[2]Gauge invariant are quantities remaining unchanged under gauge transformation. They are useful to connect one gauge to another.

and kinetic terms, or possibly including multiple fields as well as different mechanisms for the generation of perturbations. Moreover, some alternatives to Inflation are still compatible with current data. If we want to discriminate between all these possibilities, we need to consider observables beyond the power spectrum of scalar perturbation. A good way to discriminate between different scenarios is the measurement of primordial non-Gaussianity. The standard single-field slow-roll paradigm implies very small deviations from Gaussianity since the field is essentially a quantum harmonic oscillator in its ground state. A certain degree of non-Gaussianity does arise from small non-linear coupling with gravity, but it has been shown to be tiny and undetectable. However a number of more complex models exist predicting some degree of non-Gaussianity in the perturbations.

If a field is not Gaussian then its power spectrum is no longer enough to fully define it, thus the natural step is to look at higher order correlator. The lowest order indicator of Non-Gaussianity is the three-point function ("skewness"), because it is identically 0 for a Gaussian field. Actual calculations in the Inflationary framework (beyond the scope of this Introduction) show that the three point function is generally and by far the largest correlator produced in non-standard models.

The study of the primordial three-point function in CMB data is thus the focus of this thesis. The most interesting aspect is that different models predict different 3-point functions, so that measurements of this type allow to strongly discriminate between different scenarios, that would otherwise be totally degenerate if looking just at the power spectrum.

We must emphasize that a non-Gaussian signal, even if present, is predicted to be totally subdominant with respect to the Gaussian component of primordial perturbations, and require very accurate, high resolution datasets to be studied. The recent CMB data provided by the WMAP, and especially *Planck* satellite, are ideal suited to this purpose.

Chapter 2

Cosmic Microwave Background Anisotropies

For decades after its discovery, the only known anisotropy in the Cosmic Microwave Background was the dipole due to the Earth motion [50]. Starting from the 1990s, however, technological progress, especially space telescopes, allowed the detection of $\sim 10^{-5}$ fluctuations in its temperature field [51]. This discovery marked a key moment in the development of the modern cosmological model, lifting a veil on the very early Universe and enabling astrophysicists to constrain a number of cosmological parameters with unprecedented accuracy. The most important feature of these anisotropies is that they are small enough to consider their evolution in linear regime. This entails that the correspondence between their sources and what we observe on the Last Scattering Layer is easy to model and understand analytically.
The main tool used in the study of these fluctuations is the *angular power spectrum* C_ℓ, which is essentially the variance derived from the spherical harmonic expansion of the temperature distribution. The comparison between observed C_ℓ and theoretical ones provides accurate information about the physics of the primordial plasma of baryons and photons.
The anisotropies can be classified as primary if are generated on the Last Scattering Surface and secondary if the deviations in photons temperature occurs in the journey towards us, after last scattering.

2.1 Power Spectrum

As we saw in the previous chapter, the CMB presents the most perfect black body spectrum in nature. Furthermore, it is highly isotropic with mean temperature $T = 2.753K$, so that we can describe it in terms of small temperature fluctuations $\Theta(\vec{x}, \hat{n}, \tau) = \Delta T/T$, where $\vec{x}$ is the radial coordinate, $\hat{n}$ is the direction vector and τ is the conformal time, so a local observer today has $\vec{x} = 0$ and $\tau = 0$. It's important to emphasize that, deriving from quantum fluctuations, $\Theta(\vec{x}, \hat{n}, \tau)$ is a random field and it's impossible to predict its magnitude in a deterministic way. For this reason what we observe and study is its statistical distribution over the full sky. CMB fluctuations lie over the surface of a sphere, for which the spherical harmonics are a complete set of orthonormal functions.

They can be expressed as a Fourier series writing:

$$\Theta(\vec{x},\hat{n},\tau)=\sum_{\ell=0}^{\infty}\sum_{m=\ell}^{\ell}a_{\ell m}(\vec{x},\tau)Y_{\ell}^{m}(\hat{n}). \tag{2.1}$$

We now want to derive a useful relation which links the multipoles $a_{\ell m}$ on the right hand side of (2.1) to the Fourier coefficients of the temperature field on the left hand side. We thus perform a plane-wave expansion for the perturbation at a given point:

$$\Theta(\vec{x},\hat{n},\tau)=\int\frac{\mathrm{d}^3k}{(2\pi)^3}\,e^{i(\vec{x}\cdot\vec{k})}\Theta(\vec{k},\hat{n},\tau)\equiv\int\frac{\mathrm{d}^3k}{(2\pi)^3}\,e^{i(\vec{x}\cdot\vec{k})}\sum_{\ell=0}^{\infty}(-i)^{\ell}(2\ell+1)\Theta_{\ell}(\vec{k},\tau)P_{\ell}(\vec{k}\cdot\hat{n}), \tag{2.2}$$

where the functions $P_\ell(\vec{k}\cdot\hat{n})$ are the *Legendre Polynomials* (see appendix B.1.1). From the addition theorem for spherical harmonics we know that:

$$P_{\ell}(\vec{k}\cdot\hat{n})=\frac{4\pi}{2\ell+1}\sum_{m=\ell}^{\ell}\overline{Y_{\ell}^{m}}(\hat{k})Y_{\ell}^{m}(\hat{n}), \tag{2.3}$$

then from direct substitution we can derive:

$$\Theta(\vec{x},\hat{n},\tau)\equiv 4\pi\int\frac{\mathrm{d}^3k}{(2\pi)^3}\,e^{i(\vec{x}\cdot\vec{k})}\sum_{\ell=0}^{\infty}(-i)^{\ell}\Theta_{\ell}(\vec{k},\tau)\sum_{m=\ell}^{\ell}\overline{Y_{\ell}^{m}}(\hat{k})Y_{\ell}^{m}(\hat{n}). \tag{2.4}$$

Equating (2.1) and (2.4) we obtain the definition of the coefficients of the CMB temperature multipoles as functions of the Legendre coefficients on the temperature field in Fourier space:

$$a_{\ell m}(\vec{x},\tau)=4\pi(-i)^{\ell}\int\frac{\mathrm{d}^3k}{(2\pi)^3}\,e^{i(\vec{x}\cdot\vec{k})}\Theta_{\ell}(\vec{k},\tau)\overline{Y_{\ell}^{m}}(\hat{k}), \tag{2.5}$$

this formula will come handy later on.
Since for $\Theta(\vec{x},\hat{n},\tau)$ it's impossible to make predictions about any particular $a_{\ell m}$, what is studied is the distribution from which they are drawn. The mean value is zero for all $a_{\ell m}$, so if they are Gaussian (and to a good approximation they are), they are fully characterized by their variance. The covariance matrix of these coefficients defines the angular power spectrum:

$$\langle a_{\ell m}\overline{a_{\ell' m'}}\rangle=C_{\ell}\delta_{\ell\ell'}\delta_{mm'}, \tag{2.6}$$

where the average is performed over a theoretical ensemble of many different realization of Universe. Unfortunately there is only one CMB sky from where we can measure the $a_{\ell m}$, therefore, in order to estimate the CMB multipoles, we have to rely on an "ergodic approximation", assuming that averaging over the azimuthal number m (*i.e.* over different multipole orientation on the sky) is equivalent to averaging on the full ensemble. This is of course justified by rotational invariance, which make the variance C_ℓ independent of m. Since, for a fixed ℓ, we have only $2\ell+1$ elements in our sample,

we obtain a fundamental lower limit to the precision with which we can determine the C_ℓ. This is called *cosmic variance* and is defined as:

$$\left(\frac{\Delta C_\ell}{C_\ell}\right)_{cv} = \sqrt{\frac{2}{2\ell+1}}. \tag{2.7}$$

The counterpart of the angular power spectrum in real space is the angular two-point correlation function of the temperature field, they are related by:

$$\langle \Theta(\hat{n}_1)\Theta(\hat{n}_2)\rangle = \frac{1}{4\pi}\sum_{\ell=0}^{\infty}(2\ell+1)C_\ell P_\ell(\hat{n}_1\cdot\hat{n}_2). \tag{2.8}$$

In the C_ℓ lies a huge amount of information about the primordial potential, the physics of the primordial plasma at recombination and the evolution of the Universe, we have to be able to discern those we are looking for. In order to separate contribution from initial condition (*i.e.* Inflation) and radiative transport effects (*i.e.* microphysics of the baryon-photon plasma before recombination) we write Fuorier counterpart of the fluctuations $\Theta_\ell(\vec{k},\tau)$ in the form:

$$\Theta_\ell(\vec{k},\tau) = \Phi(\vec{k})\Delta_\ell(k,\tau), \tag{2.9}$$

$\Phi(\vec{k})$ is the primordial potential fluctuations that we already encountered in the previous chapter and $\Delta(k,\tau)$ is the solution of a Boltzmann equation derived by keeping into account all gravitational and physical interactions between matter and radiation components in the Universe before recombination. $\Delta(k,\tau)$ is called the *CMB radiation transfer function.*

The Boltzmann equation describes the statistical behavior of a thermodynamic system out of thermodynamic equilibrium. In other words it tells us how the abundance and the energy distribution of every component of the Universe changes in consequence of their interactions. This allows to predict how the perturbations evolve when they cross the horizon and they begin to be affected by micro-physical effects. This evolution is formalized by the transfer function: it quantifies the variations of energy density due to the energy transport and how these affect the CMB temperature field. A full treatment of the Boltzmann equation for CMB anisotropies is beyond the scope of this thesis, and can be found in *e.g.* [14]. The Boltzmann equation is generally solved numerically by public available "Boltzmann code", such as CMBfast and CAMB, yielding the final transfer function and allowing the computation of the CMB power spectrum, as well of the bispectrum, as we will see in the following chapter.

The power spectrum of initial fluctuations is the two-point correlator of $\Phi(\vec{k})$:

$$\langle \Phi(\vec{k})\Phi(\vec{k'})\rangle = (2\pi)^3 P_\Phi(k)\delta^3(\vec{k}+\vec{k'}). \tag{2.10}$$

To relate it to the angular power spectrum we combine (2.10), (2.5) and (2.6) to get:

$$\langle a_{\ell m}\overline{a_{\ell' m'}}\rangle =$$
$$= (-i)^{\ell+\ell'}(4\pi)^2 \iint \frac{\mathrm{d}^3k}{(2\pi)^3}\frac{\mathrm{d}^3k'}{(2\pi)^3}\langle\Phi(k)\overline{\Phi}(k')\rangle e^{i(\vec{x}\cdot\vec{k}-\vec{x}\cdot\vec{k'})}\Delta_\ell(k,\tau)\Delta_{\ell'}(k',\tau)\overline{Y_\ell^m}(\hat{k})Y_{\ell'}^{m'}(\hat{k'}), \tag{2.11}$$

applying (2.10), for the Dirac delta's proprieties this equation becomes:

$$\langle a_{\ell m}\overline{a_{\ell' m'}}\rangle = (-i)^{\ell+\ell'}(4\pi)^2 \int \frac{\mathrm{d}^3k}{(2\pi)^3} P_\Phi(k)\Delta_\ell(k,\tau)\Delta_{\ell'}(k,\tau)\overline{Y_\ell^m}(\hat{k})Y_{\ell'}^{m'}(\hat{k}). \tag{2.12}$$

The angular part of the integral over the spherical harmonics leaves two δ factor, giving the final formula:

$$\begin{aligned}\langle a_{\ell m}\overline{a_{\ell' m'}}\rangle &= C_\ell\delta_{\ell\ell'}\delta_{mm'} = (-i)^{\ell+\ell'}\frac{2}{\pi}\int \mathrm{d}k\, k^2 P_\Phi(k)\Delta_\ell(k,\tau)\Delta_{\ell'}(k,\tau)\delta_{\ell\ell'}\delta_{mm'},\\ C_\ell &= \frac{2}{\pi}\int \mathrm{d}k\ k^2 P_\Phi(k)\Delta_\ell^2(k,\tau).\end{aligned} \tag{2.13}$$

This relation connects, for a given ℓ, the observable C_ℓ with the theoretical quantity $\Theta_\ell(\vec{k},\tau)$, which depends on the composition of the primordial plasma, and on initial conditions at the end of inflation, providing a fundamental test for the cosmological models.
It's important to notice that at first order the C_ℓ and $P_\Phi(k)$, as well as $a_{\ell m}$ and Φ, are linked by a linear operator, hence if the primordial perturbation field is Gaussian also the CMB temperature field must show the same distribution. This makes the CMB a perfect observable to test primordial non-Gaussianity.
If we were working with galaxies, primordial non-Gaussianity will be concealed by the effects of the highly non-linear evolution undergone by matter distribution in recent eras. In this context the effect of primordial non-Gaussian signal constitutes only a correction on the galaxy bispectrum, so that to measure the primordial signal we have first to distinguish it from non-Gaussianity due to non-linear evolution.
The relations presented in this chapter show that knowing $\Delta_\ell(k,\tau)$ allows to fully determine the C_ℓ, and account for all radiative effects. As we were mentioning earlier, the calculation of $\Delta_\ell(k,\tau)$ can be done through a full numerical treatment of the Einstein-Boltzmann system. However it is still useful to get an idea of the Physical processes involved, and to derive analytical expression of the transfer functions in special cases, in particular for large scale perturbations, where the microphysics does not play a rule (on superhorizon scales causal interactions cannot take place). This is what we are going to do in the next section.

2.2 Primary Anisotropies

As we stated before, primary anisotropies are generated in the epoch before recombination. To understand their nature we have to know the behavior of the pre-recombination

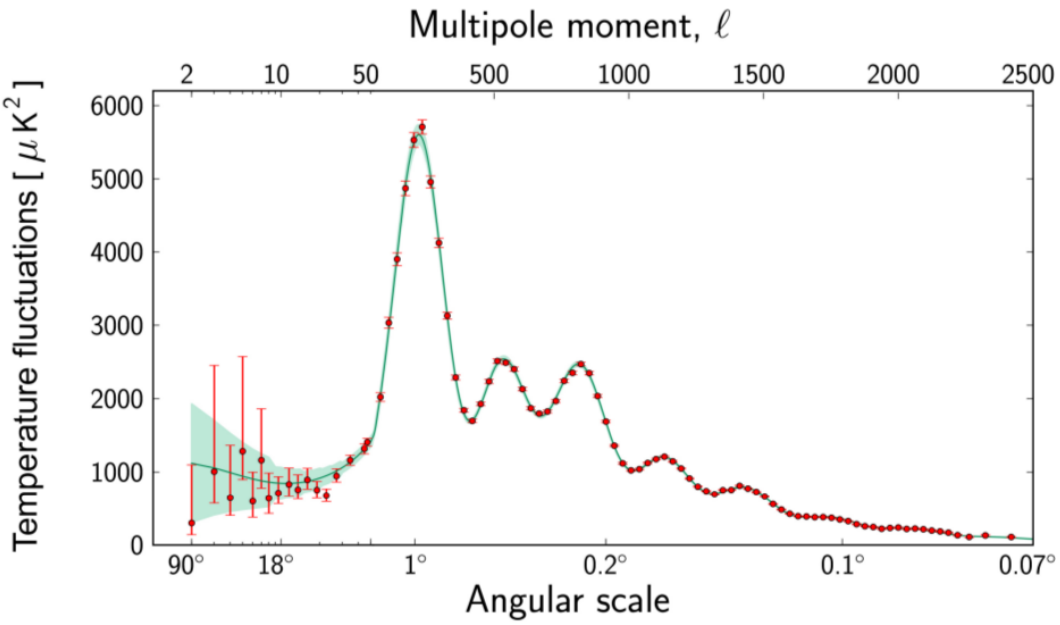

Figure 2.1: CMB power spectrum. The red dots correspond to measurements made with *Planck* Surveyor. The green curve represents the theoretical best fit while the pale area around the curve shows the predictions of all the variations of the standard model that best agree with the data. Source http://sci.esa.int/planck/.

Universe. As we mentioned in section 1.1.3, the very Early Universe was ionized and optically thick. Photons interacted with electrons via Compton scattering forming a tightly coupled system (including protons, linked to electrons via Coulomb scattering [35]), and could not freely propagate. As the Universe expanded and cooled down, electrons and protons combined to form neutral hydrogen. When this process was completed, photons no longer interacted with baryons and the Universe became transparent. This is called the epoch of recombination and it took place at $z \sim 1100$, when the temperature was $\sim 3000\,K$ [34][58][42].
Before recombination, gravitational infall of electrons and protons into potential wells (formed by dark matter) was not possible, due the radiation pressure. When the density of matter an radiation increases, due to gravitational infall, also radiation pressure (proportional to density) increases, until it eventually reverse the motion. We thus get propagation of *acoustic waves* in the plasma.
In a Universe with a low baryon content (like the one in which we live), the speed of sound in the plasma is very close to $c/\sqrt{3}$ and it defines the *acoustic horizon i.e.* the distance that acoustic oscillations could travel from $t = 0$ up to a given time t. The acoustic horizon at the recombination define a crucial scale: perturbations with wavelenght larger than this scale could not oscillate, contrarily to sub horizon scale.
We now study in more detail the behavior of the photon-baryon fluid in these two cases.

2.2.1 Large Scales

As just mentioned above at scales larger than the *acoustic horizon* at recombination ($\sim 2^\circ$) perturbations cannot be affected by any microphysics. These anisotropies are frozen into their initial conditions, as they were set down by the primordial potential presumably during Inflation. If we assume a scale invariant primordial power spectrum $P_\Phi(k)$, then at low multipoles, the CMB angular power spectrum also displays a scale-invariant behavior, as we expect from the fact that there aren't physical process that can drive any kind of evolution. This would in principle make large scales ideal to test Inflation but, unfortunately, in this regime the measurement is also strongly limited by the cosmic variance, as we saw in formula (2.7).
The phenomenon which dominates the super-Horizon fluctuations is called *Sachs-Wolfe effect* [41]. The initial potential generates metric perturbations on the last scattering surface and the photons undergo gravitational redshift escaping from them after recombination. Moreover, due to these perturbations, time at the bottom of the potential well is slightly shifted with respect to standard cosmic time in the unperturbed background. For small fluctuations the gravitational redshift effect, in natural units, gives a contribution of:

$$\frac{\Delta T}{T} = \frac{\Delta \nu}{\nu} = \Phi(r_*, \hat{n}), \tag{2.14}$$

where r_* indicates that the potential is defined at the last scattering surface. The time dilation gives:

$$\frac{\Delta T}{T} = -\frac{\Delta a}{a} = -\frac{2}{3}\frac{\Delta t}{t} = -\frac{2}{3}\Phi(r_*, \hat{n}), \tag{2.15}$$

where we take into account that, in the matter dominate epoch, $a \propto t^{\frac{2}{3}}$.
The net effect is therefore:

$$\frac{\Delta T}{T} = \frac{1}{3}\Phi(r_*, \hat{n}). \tag{2.16}$$

The angular power spectrum due to large scale anisotropies can be computed analytically thanks to the simplicity of the transfer function. The perturbation is simply $\Theta_\ell(\vec{k}, \tau) = \frac{1}{3}\Phi(k)$, plugging this into formula (2.5), and expanding the exponential in spherical harmonics,

$$\mathrm{e}^{\mathrm{i}(\vec{k}\cdot\vec{x})} = \sum_{\ell=0}^{\infty} \mathrm{i}^\ell j_\ell(kx) \sum_{m=-\ell}^{\ell} \overline{Y}_\ell^m(\hat{n}) Y_\ell^m(\hat{k}), \tag{2.17}$$

the coefficient $a_{\ell m}$ becomes:

$$a_{\ell m} = \frac{4\pi}{3}\overline{Y}_\ell^m(\hat{n}) \int \frac{\mathrm{d}^3 k}{(2\pi)^3}\Phi(\vec{k}) j_\ell(kx)\overline{Y_\ell^m}(\hat{k}) Y_\ell^m(\hat{k}). \tag{2.18}$$

Squaring this equation through the same process illustrated above we obtain:

$$\langle a_{\ell m} a^*_{\ell' m'} \rangle = \frac{2}{9\pi} \int \mathrm{d}k \; k^2 P_\Phi(k) j^2_\ell(kr_*) \delta_{ll'} \delta_{mm'}$$
$$C^{SW}_\ell = \frac{2}{9\pi} \int \mathrm{d}k \; k^2 P_\Phi(k) j^2_\ell(kr_*), \tag{2.19}$$

where the apex SW denotes that we are working in *Sachs-Wolfe approximation*. It is evident from previous definitions, and from formula (2.18), that the Sachs-Wolfe transfer function is $\Delta_\ell(k, \tau_*) = \frac{1}{3} j_\ell(kr_*)$. The power spectrum is $P_\Phi(k) = Ak^{n_s - 4}$, this integral has an analytical solution in terms of gamma functions (see appendix (B.3)):

$$\int_0^\infty \mathrm{d}k \; k^{n-2} j^2_\ell(kx) = 2^{n-4} \pi \frac{\Gamma(\ell + \frac{n}{2} - \frac{1}{2}) \Gamma(3 - n)}{\Gamma(l + \frac{5}{2} - \frac{n}{2}) \Gamma^2(2 - \frac{n}{2})}. \tag{2.20}$$

In the Harrison-Zel'dovich-Peebles model $n_s = 1$, in this case, considering the proprieties of the gamma function and the particular value $\Gamma\left(\frac{3}{2}\right) = \frac{\sqrt{\pi}}{2}$, we have:

$$\begin{aligned} C^{SW}_\ell &= \frac{2}{9\pi} A \left[2^{-3} \pi \frac{\Gamma(\ell)}{\Gamma(\ell + 2)} \frac{4}{\pi} \right] \\ &= \frac{A}{9\pi} \frac{\Gamma(\ell)}{\ell(\ell + 1)\Gamma(\ell)} = \frac{A}{9\pi} \frac{1}{\ell(\ell + 1)}. \end{aligned} \tag{2.21}$$

The product $\ell(\ell+1)C^{SW}_\ell$ is a constant. For this reason typically it is plotted $\ell(\ell+1)C_\ell$ instead of C_ℓ: where the Sachs Wolfe effect dominates we expect a plateau. This also concretely shows what we already mentioned earlier: a scale invariant primordial spectrum generates a scale invariant CMB spectrum on large scale in Sachs-Wolfe approximation. However, as it can be seen from figure 2.1, showing the actual power spectrum extracted from real data, even on large scales the spectrum is not perfectly flat. This is due to the fact that, in the complete picture, we have to consider not only the Sachs-Wolfe effect at recombination, but also late time evolution of the gravitational potential during the photon free streaming phase after recombination. This is part of the so called *Integrated Sachs-Wolfe Effect*, and we will discuss it in the section concerning secondary anisotropies.

2.2.2 Small Scales

Inside the horizon the fluctuations can be affected by causal physics. Scattering processes lead the evolution of perturbations and couple the baryons and the photons. This brings to the establishment of an equilibrium in which the gravitational potential is balanced by the radiation pressure. The main effects of Thomson scattering are *acoustic oscillations* and *diffusion damping*: the spectrum presents a series of peaks and troughs starting from the sound horizon's scale at $\ell \sim 250$ whose amplitude decreases with the scale. This trend can be clearly observed in figure 2.1. Being in strict relation with the composition of the primordial Universe the features of these peaks are a sensitive diagnostic of the ratio of dark matter and baryons and of the value of the principal cosmological parameters.

We will now provide a short qualitative description of these effects, trying to clarify the link between the physics of the baryon-photon fluid and the composition of the Universe. This simple outline will suffice for the aim of this thesis. See *e.g.* [25] for a complete treatment.

Acoustic Peaks The variations of the gravitational potential force the matter to clump into the potential wells. When a critical value of density is reached radiation pressure becomes dominant causing rarefaction of the fluid. The rarefaction continues until the gravitational attraction prevails once again and the oscillation restarts.

We saw that the amplitude of the C_ℓ represents the variance on the scale ℓ. We expect to observe an higher degree of anisotropy on the scale corresponding to modes caught at their maximum compression or rarefaction at recombination. Looking at figure 2.1, at an angular scale of order one degree we find the first peak that corresponds to the mode that completed half an oscillation. Then, at angular scales roughly an half of the first, we find the second that corresponds to the modes that ended a full cycle. This alternation continues until the peaks are damped by diffusive processes.

The acoustic peaks are a indicator of the baryon density at the recombination. As it can be seen from the upper panel of figure 2.2, if we consider an ideal completely photon-dominated fluid, the infall in the potential well doesn't modify the potential since the photon are massless. Baryons instead increase the gravitating mass making the wells deeper when they fall in, as it can be seen in lower panel of figure 2.2. This effect is the so called *baryon drag* in consequence of which the odd peaks on the spectrum, representing compressions, are higher than the evens one, representing rarefactions.

Diffusion Damping Diffusion damping appears at very small scale. Clearly in the photon-baryon fluid the scattering rate is high but not infinite, so the photons travel a certain distance λ_D between scatters.This leads to a dissipation of the anisotropies under this scale. This effect is also known as *Silk Damping* [48].

2.3 Secondary Anisotropies

After recombination, CMB photons free streamed across the entire visible Universe, gathering a wealth of information about its structure and evolution. The imprints of this long journey on the power spectrum are the so called *secondary anisotropies*. They reflect the processes that the free-steaming photons undergo after recombination. We divide them in gravitational effects and radiative effects.

The gravitational secondaries derive from gravitational potential variations along the path of the photons, that result in a non-null gravitational redshift effect. The most important gravitational effect is the *Late Integrated Sachs-Wolfe* effect (LISW). During matter domination the potential is constant at the first order, however during the Λ-dominated era the potential decays over a very long time scale generating the LISW. This effect generally shows up only in the lowest ℓ due to the slowness of the potential decays. In other words potential wells due to to high ℓ modes were crossed by photon in too little time to change significantly under the effect of dark energy.

At 2nd order the potential evolves also during matter domination giving rise to the *Rees-Sciama Effect* [40]. The potential fluctuations change in time in consequence of clustering of matter and of bulk motion of dark matter halos across the line of sights

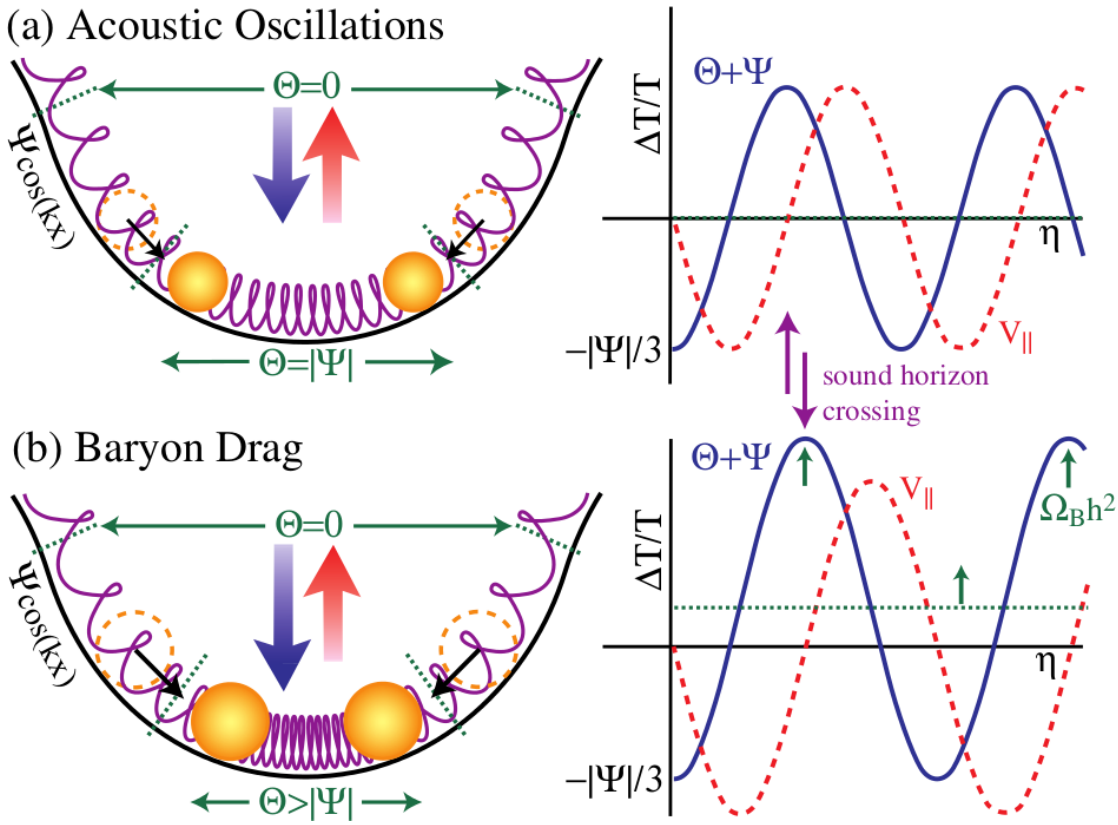

Figure 2.2: Schematic view of acoustic oscillation. *Left* potential well in real space. *Right* Evolution of potential energy and velocity. (a) Photon dominated system(b) Realistic case of photon-baryon fluid.

[8][55][45]. Another important effect is gravitational lensing due to large scale structure potential affecting the direction of propagation of free-streaming photons. It provides a second-order contribution in the perturbation theory [9].
Scattering secondaries are generated during the so called epoch of *reionization*. At $z \sim 6$ the radiation of the first generation massive star caused the ionization of the hydrogen. The high cross section of the reappeared free electrons gave rise to the recoupling of CMB photons with baryons. The consequences were the suppression of primordial anisotropy, the generation of large angle polarization and large angle Doppler effect.
The most relevant radiative contribution among secondary anisotropies is provided by the *Sunyaev-Zel'dovich effect* [54]. It derives from the interaction with the gas in galaxy clusters and dark matter halos. The internal motion of this gas provide Doppler shift as there is a transfer of energy between the hot gas and the low energy CMB photon. In addition there is also a little kinetic contribution from the peculiar velocities of gas clouds. The Sunyev-Zel'dovich effect dominates the power spectrum of secondary anisotropies on angular scale $\sim 1'$.
There are many other subdominant effects, for a complete treatment see *e.g.* [25]. **Non-Gaussianity** Being produced when the Universe was already organized in very non linear structures, most of the secondaries are non linear. The consequence is the production

of a certain degree of non Gaussianity in the temperature distribution. These effects could in principle contaminate estimates for primordial non-Gaussianity by modifying the bispectrum (essentially the three-point function of the fluctuation field, see chapter 3 for an accurate definition). Estimates of bispectra due to correlation between different secondaries, for example ISW-lensing or SZ-lensing, show that these effect can be significant for an experiment with the sensitivity of *Planck* but not for WMAP, [47][33]. However the non-Gaussian level arising from non-linear effects seems to be small enough to be neglected [29] and it will thus ignored in the following.

2.4 Cosmological Parameters

The study of the CMB anisotropies is an efficient way to measure cosmological parameter. We will now outline how changes in different parameters (total density, baryon density, dark matter density, dark energy density) affects the shape of the angular power spectrum.
The total density parameter Ω is strictly related to the curvature. If the Universe is not flat, the angular diameter distance is different from the coordinate distance. We will observe the same physical scales subtending smaller angles in an open Universe and larger angles in a closed one. For a given matter and radiation content of the Universe, the acoustic horizon provides a fixed scale, defining the position of the first peak. In light of the argument just outlined, we then see that the first peak moves in ℓ and all the spectrum is shifted if Ω varies. The position of the first peak is thus a powerful indicator of the curvature of our Universe.
As we saw in section 2.2.2 acoustic oscillations depend directly on the baryon density Ω_b, the effects of baryons beings illustrated in figure 2.2. An increase in the baryon contribution amplifies the compressions and decreases the rarefactions. As we saw, odd peaks represent compressions and even peak rarefactions. A change in the baryon density then modifies the ratio between the amplitudes of even and odd peaks. Furthermore, the baryon density influences the mean free path of photons: the larger it is the more the damping scale moves to smaller angular scales.
The matter density Ω_m determines the epoch of equality, that is, the epoch in which the matter equals the radiation contribution to the energy. The first consequence is that since the expansion rate depends on the dominant component, the physical scale of sound horizon at recombination is sensitive to the duration of radiation era. Furthermore, the radiation drives the acoustic oscillation by making the gravitational potential evolve with time [26], while dark matter does not since it is pressure less. Since the radiation doesn't cluster, the longer the Universe was radiation dominated the larger are oscillations. Rarefaction peaks are thus enhanced over compression peaks at small angular scales. In fact small scales enter the horizon and starts oscillating early, during radiation domination. In this regime, during rarefaction the gravitational potential decreases (because it is driven by the density of photons, that is decreasing), making rarefaction itself stronger. The ratio between odd and even peaks on small scales (but large enough not to be strongly affected by diffusive damping) is thus a powerful indicator of the time

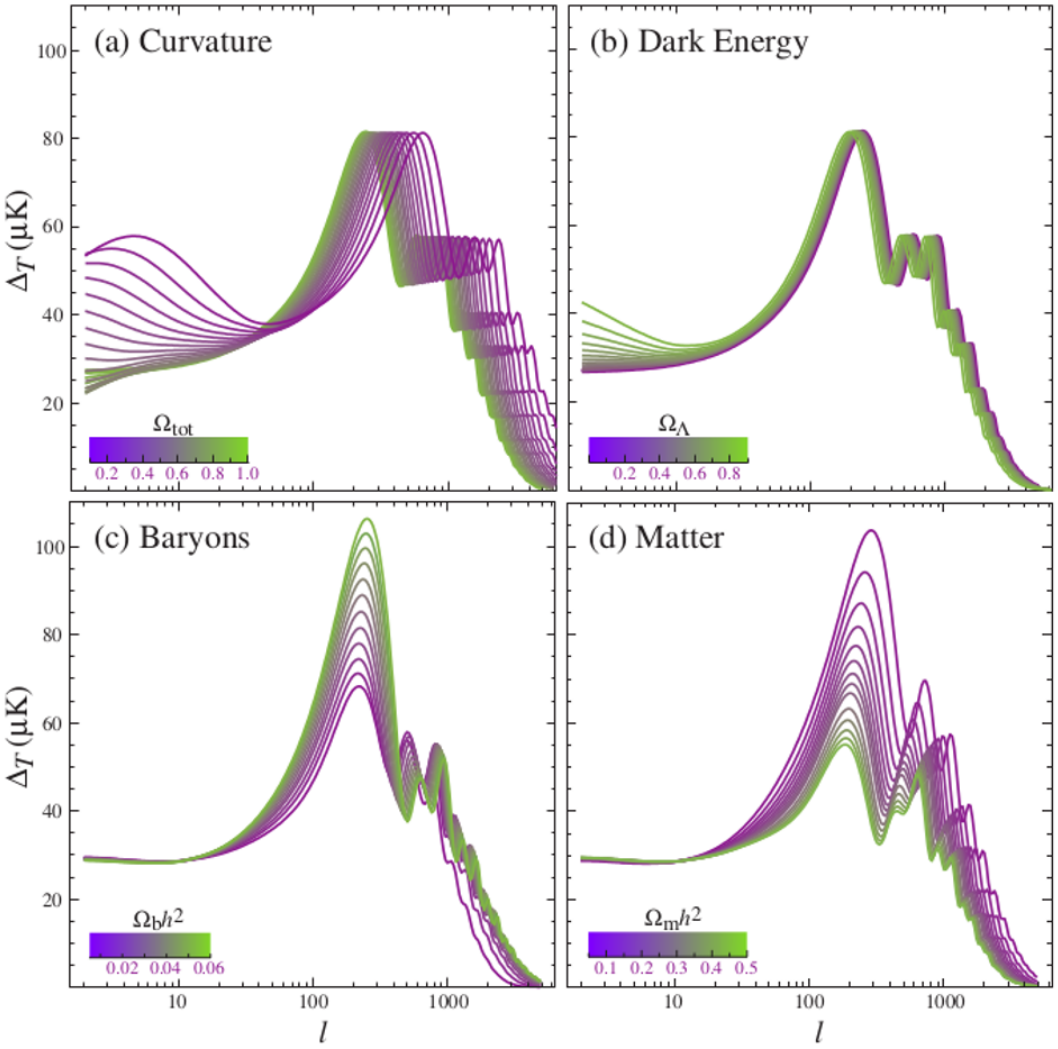

Figure 2.3: Variations of the power spectrum as function of cosmological parameters[25].

of equality [1], and consequently of the density of Dark Matter.
Dark energy was not dominating at the time of recombination. Therefore, the primary anisotropies aren't affected by it. We can observe the main effects of a non-zero cosmological constant on free-streaming photons. First of all the spectrum is shifted to larger angular scales due to the change in conformal time. The more sensitive effect to Ω_Λ is however the LISW since it depends on changes in the amplitude of the gravitational potential, generating differential redshift effects on large scales, as already explained in section 2.3. In a Λ Universe anisotropies on large scale grows, so the small scale perturbations decrease as effect of normalization.
The effects we described in this section are illustrated in figure 2.3. A full treatment

[1] If equality happens earlier, radiation driving and the subsequent enhancing of odd over evens peaks takes place at smaller and smaller scales, since modes need to enter the horizon very early to be able to oscillate during the radiation dominated phase

of this topic would require the introduction of several additional parameters, as well as a complete (numerical) Boltzmann approach. However, the study of cosmological parameters is not the focus of his thesis, and our aim in this section was just to provide a short intuitive explanation of why the CMB power spectrum is such a sensitive probe of cosmological parameters. A thorough treatment of this important topic, including a description of the overall statistical framework required to actually extract parameters from measured C_ℓ, can be found in *e.g.* [25].

2.5 CMB surveys

The high resolution measurements provided by the *Planck* mission are the last stage of an amazing run, started in 1965 with the serendipitous CMB discover by Penzias and Wilson . If nowadays we are able to make precise analysis of the temperature distribution on the Last Scattering Surface, it is thanks to the stunning technological progress, that, in less than fifty years, transforms Cosmology from speculative to precision science.
The first measurements of the CMB mainly focused on the determination of its electromagnetic spectrum. For ground observations, due to atmospheric emission, only the Rayleigh-Jeans region was accessible. During the 1970s and 1980s several high altitude balloon experiments, carrying millimetre and submillimeter spectrometers, were flown, finding evidence for the expected turn-over in the Wien region of the spectrum. However, some discrepancies between different experiments held the debate on the black-body nature of the CMB open.
To solve this question definitively, in 1989 NASA launched the first space mission dedicated to studies of the CMB: the *Cosmic Background Explorer*, better known as COBE. For the first time it was possible to provide a detailed measurement of the CMB spectrum from the millimetre to the infrared region. The *Far Infrared Absolute Spectrophotometer* (FIRAS) covered the wavelength range from 0.1 to 10 mm in two spectral channels. It operated differentially, comparing its measurements with an internal reference blackbody. The result was a nearly perfect blackbody spectrum, corresponding to a temperature of $2.726 \pm 0.010K$, with deviations from the blackbody form smaller than 0.03%. We showed the final spectrum measured by COBE in the previous chapter in figure 1.2.
Beside the measurement of the spectrum, the objectives of COBE were to provide a full-sky map of infrared dust emission, and to map the deviations from isotropy over the sky.
The instrument dedicated to the study of anisotropies was the *Differential Microwave Radiometer* (DMR), which operated in three band in the Rayleigh-Jeans region (31.5, 53 and 90 GHz) reaching an angular resolution of 7°, corresponding to $\ell_{max} \sim 30$. With this instrument, COBE measured the dipolar anisotropy due to our motion with respect the cosmological reference frame, and achieved to detect anisotropies in the Sachs-Wolfe region of the power spectrum.
After the COBE measurement, the attention of the scientific community focused on the detection of small-scale anisotropies. The first identification of small-scale anisotropies was obtained by sub-orbital balloon mission, the *Balloon Observations Of Millimetric Extragalactic Radiation and Geophysics*, more known as BOOMERanG. Crucial, for the success of this mission, was the introduction of bolometers as astronomical instruments,

mission	COBE	WMAP	Planck
pixels number	104	3×106	5×107
FWHM	7°	$12'$	$5'$
ℓ_{max}	30	1000	3000
band	3	5	9
spectral range [GHz]	$31.5 - 90$	$23 - 94$	$30 - 857$

Table 2.1: Principal technical characteristics of the missions COBE, WMAP and *Planck*

that allow high precision measurements of radiation temperature.
However, with balloon experiments is not possible to obtain a full-sky map.
The first complete map of small-scale anisotropies on CMB sky was provided by the NASA WMAP mission (*Wilkinson Microwave Anisotropy Probe*). WMAP angular resolution was twenty times higher than COBE (12 arcmin, corresponding to $\ell_{max} \sim 1000$), it observed in five different frequencies (23, 33, 41, 61 and 94 GHz). It perform analysis of temperature and polarization distributions power spectrum, playing the key role in establishing the current Standard Model of Cosmology.
The ESA *Planck* mission went beyond WMAP, improving the angular resolution to 5 arcmin, corresponding to $\ell_{max} \sim 3000$, as well as increasing both sensitivity and frequency coverage (the latter being an essential experimental feature for accurate subtraction of Astrophysical foregrounds). Its instrumentation works in in 9 different band (30, 44, 70, 100, 143, 217, 353, 545, 857 GHz), allowing an unprecedented estimation of the sky brightness in these frequencies. *Planck* also uses two different types of detectors. Radiometers at low frequencies (30-70 GHz) form the so called *Low Frequencies Instrument* (LFI). The *High Frequencies Instruments* (HFI) covers instead the range $100 - 857$ GHz. This combination of different detector technologies allows for a tight control of instrumental systematics.
In figure 2.4 we shows the CMB sky maps provided by these missions, it is evident the remarkable improvement in angular resolution between the missions. In table 2.1 we resume the principal characteristic of the missions, the resolution, the region of the electromagnetic spectrum covered.

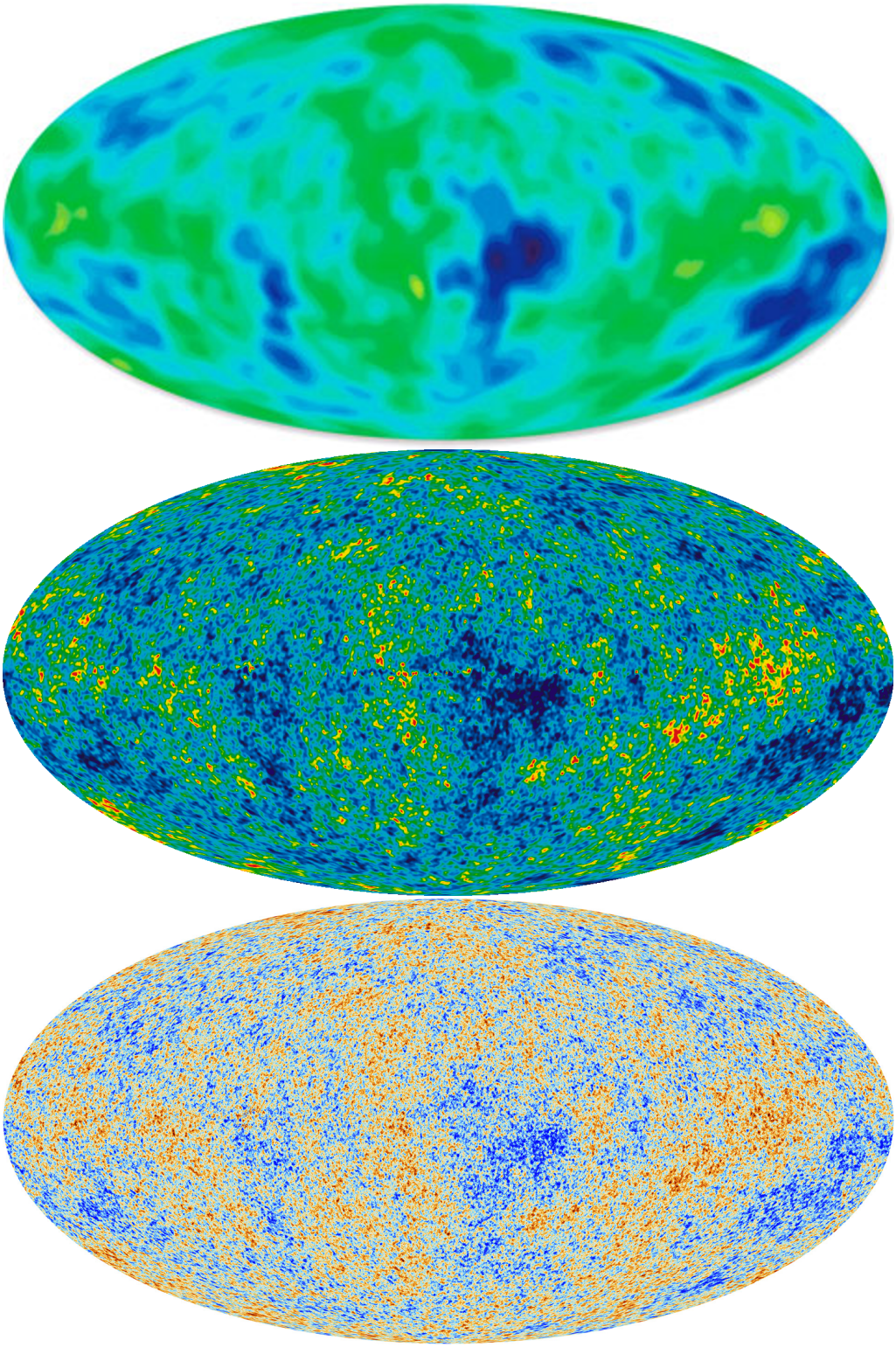

Figure 2.4: Comparison between the CMB sky maps provided by COBE (top), WMAP (center) and *Planck* (bottom). Credit NASA, ESA

Chapter 3

The CMB Bispectrum

In the pursuit for non-Gaussianities the two-point function and the power spectrum are no longer sufficient to characterize the Cosmological field of interest. As we saw in section 1.2, the power spectrum completely defines a Gaussian field. If the field is no longer Gaussian, the distribution cannot be described only in terms of average and variance, but also the higher moments are needed.
We know that, in case of a non Gaussian distribution the odd moments are no longer vanishing. In the same way as the variance is related to the Power spectrum and to the two-point correlator, we can relate the third moment, the skewness, to the three-point correlator and to its Fourier transform counterpart, the *bispectrum*. Since it is related to the third moment, also the bispectrum vanishes if the field is Gaussian. Measurements of the bispectrum amplitude thus provide a very sensitive indicator of departures from Gaussianity.
The bispectrum is usually characterized by an amplitude parameter: f_{NL}, here "NL" stands for "non-linear". It is a dimensionless parameter representing the overall amplitude of the curvature bispectrum. Bispectrum measurements are the most promising tool to test small primordial departures from Gaussianity. Other statistics, like the 4-point function, generally do not provide additional information about non-Gaussianity from Inflation [13]. An intuitive argument, which clarifies why this is the case, can be derived by remembering that non-Gaussianity from Inflation is generally very small, and expanding the primordial non-Gaussian field in a Taylor series around its Gaussian component, with f_{NL} providing the amplitude of the three-point function of expanded field. So that we expand the primordial potential in terms of an underlying Gaussian process:

$$\Phi(x) = \Phi_L(x) + f_{NL}(\Phi_L^2(x) - \langle\Phi_L^2(x)\rangle) + g_{NL}\Phi_L^3(x) + \dots , \tag{3.1}$$

here g_{NL} represents the amplitude of the non-Gaussian contribution from the four-point correlator; since the magnitude of the potential fluctuation is $\Phi_L \simeq 10^{-5}$ we see that, unless $g_{NL} >> f_{NL}$, higher order correlator are suppressed by the increasing power of Φ_L. We will see in this chapter that this expansion, called "local", strictly applies only to some Inflationary model, namely, those generating non-Gaussianity of the so called local type. However the general argument holds in nearly all cases.
As for the power spectrum, since it is defined on the surface of a sphere the CMB angular

power spectrum is obtained in terms of an harmonic expansion instead of the classical Fourier transform. Preserving the formalism of the previous chapters we can now define the angular bispectrum as:

$$B_{\ell_1\ell_2\ell_3}^{m_1m_2m_3} = \langle a_{\ell_1m_1} a_{\ell_2m_2} a_{\ell_3m_3} \rangle. \tag{3.2}$$

In order to distinguish between geometrical and physical proprieties the bispectrum can be expressed as [28]:

$$B_{\ell_1\ell_2\ell_3}^{m_1m_2m_3} = \mathcal{G}_{\ell_1\ell_2\ell_3}^{m_1m_2m_3} b_{\ell_1\ell_2\ell_3}, \tag{3.3}$$

here $\mathcal{G}_{\ell_1\ell_2\ell_3}^{m_1m_2m_3}$ is the *Gaunt integral* and $b_{\ell_1\ell_2\ell_3}$ is called the *reduced bispectrum*. The Gaunt integral is defined by:

$$\begin{aligned}\mathcal{G}_{\ell_1\ell_2\ell_3}^{m_1m_2m_3} \equiv& \int \mathrm{d}^2\hat{n}\; Y_{\ell_1}^{m_1}(\hat{n}_1) Y_{\ell_2}^{m_2}(\hat{n}_2) Y_{\ell_3}^{m_3}(\hat{n}_3) \\ =& \sqrt{\frac{(2\ell_1+1)(2\ell_2+1)(2\ell_3+1)}{4\pi}} \begin{pmatrix} \ell_1 & \ell_2 & \ell_3 \\ 0 & 0 & 0 \end{pmatrix} \begin{pmatrix} \ell_1 & \ell_2 & \ell_3 \\ m_1 & m_2 & m_3 \end{pmatrix},\end{aligned} \tag{3.4}$$

where the matrix is the Wigner-3j symbol , $\mathcal{G}_{\ell_1\ell_2\ell_3}^{m_1m_2m_3}$ is a real function which ensured that the bispectrum satisfies the triangle conditions and selections rules: $m_1 + m_2 + m_3 = 0$, $\ell_1 + \ell_2 + \ell_3 = even$ and $|\ell_i - \ell_j| \leq \ell_k \leq \ell_i + \ell_j$; in turn, these conditions guarantee the invariance under translation. For further details about the Wigner symbols proprieties see the appendix B.4.
The fact than we can find a factorization in which the reduced bispectrum is m-independent describes instead rotational invariance (isotropy) of the CMB sky.
As for the power spectrum we can estimate the Bispectrum as an average on all the m values. The observable quantity is thus the angle averaged bispectrum, given by:

$$B_{\ell_1\ell_2\ell_3} \equiv \sum_{m_1m_2m_3} \begin{pmatrix} \ell_1 & \ell_2 & \ell_3 \\ m_1 & m_2 & m_3 \end{pmatrix} B_{\ell_1\ell_2\ell_3}^{m_1m_2m_3}. \tag{3.5}$$

Inserting (3.3) in (3.5) and applying the orthogonality relation of the Wigner symbols (B.18), given the definition of $\mathcal{G}_{\ell_1\ell_2\ell_3}^{m_1m_2m_3}$ (3.4), the angle averaged bispectrum can be expressed as:

$$B_{\ell_1\ell_2\ell_3} = \sqrt{\frac{(2\ell_1+1)(2\ell_2+1)(2\ell_3+1)}{4\pi}} \begin{pmatrix} \ell_1 & \ell_2 & \ell_3 \\ 0 & 0 & 0 \end{pmatrix} b_{\ell_1\ell_2\ell_3}. \tag{3.6}$$

3.1 Primordial Bispectrum

To obtain information about the primordial potential from the CMB bispectrum we must define in which way the two quantities are linked. Equation (3.6) can be rewritten inserting the definition of angular bispectrum (3.2) and linking $a_{\ell m}$ to Φas in formula (2.5), so that we get:

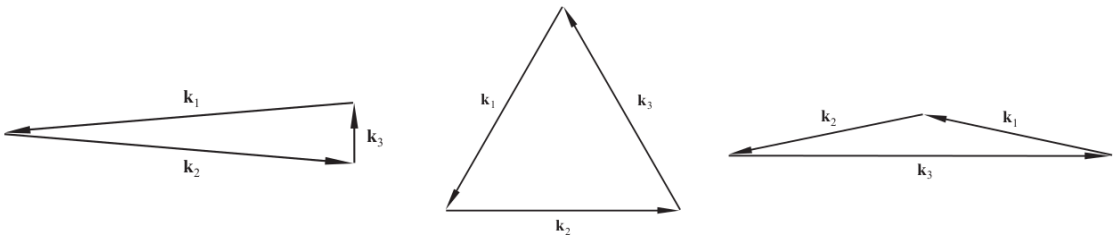

Figure 3.1: Triangle types contributing to the bispectrum corresponding to "squeezed" configurations with $k_3 << k_1 = k_2$ (left), equilateral configurations with $k_3 \simeq k_2 \simeq k_1$ (center) and flattened configurations with $k_3 \simeq k_1 + k_2$ (right). Image taken from [29].

$$
\begin{aligned}
B_{\ell_1\ell_2\ell_3} = (4\pi)^3(-i)^{\ell_1+\ell_2+\ell_3} \sum_{m_1m_2m_3} \begin{pmatrix} \ell_1 & \ell_2 & \ell_3 \\ m_1 & m_2 & m_3 \end{pmatrix} \times \\
\times \iiint \frac{\mathrm{d}^3k_1}{(2\pi)^3}\frac{\mathrm{d}^3k_2}{(2\pi)^3}\frac{\mathrm{d}^3k_3}{(2\pi)^3}\overline{Y_{\ell_1}^{m_1}}(\hat{k}_1)\overline{Y_{\ell_2}^{m_2}}(\hat{k}_2)\overline{Y_{\ell_3}^{m_3}}(\hat{k}_3)\times \\
\times \langle\Phi(\vec{k}_1)\Phi(\vec{k}_2)\Phi(\vec{k}_3)\rangle\Delta(k_1,\tau)\Delta(k_2,\tau)\Delta(k_3,\tau),
\end{aligned} \tag{3.7}
$$

where $\Delta(k,\tau)$ is the transfer function and $\langle\Phi(\vec{k}_1)\Phi(\vec{k}_2)\Phi(\vec{k}_3)\rangle$ is the three-point function of the primordial potential $\Phi(\vec{k})$ that can be defined as [43]:

$$
\langle\Phi(\vec{k}_1)\Phi(\vec{k}_2)\Phi(\vec{k}_3)\rangle = (2\pi)^2\delta_D^3(k_1+k_2+k_3)B_\Phi(k_1,k_2,k_3). \tag{3.8}
$$

$B_\Phi(k_1,k_2,k_3)$ is the primordial bispectrum, as it is function of the primordial potential only. Every model of Inflation predict a different potential $\Phi(\vec{k})$ from which it derives a specific prediction for the primordial bispectrum.

3.2 Amplitude Parameter and Shape Function

The primordial bispectrum is usually described by the *amplitude parameter* f_{NL} and the *shape function* [43]:

$$
B(k_1,k_2,k_3) = f_{NL}F(k_1,k_2,k_3) \tag{3.9}
$$

here $F(k_1,k_2,k_3)$ is the shape function that defines the dependence of the bispectrum on particular triangular configurations, the so called *shapes*. The most important bispectrum shapes, encompassing a large number of Inflationary scenarios, are showed in figure 3.1. The reason for which studies of the primordial bispectrum focus on the determination of a single amplitude parameter is that the amplitudes of the individual triangle configurations are way too small to be detected. Cosmic variance is too large to allow the measurement of a single configuration. The signal-to-noise ratio of a single configuration is:

$$
\frac{S}{N} \simeq \frac{B_{\ell_1\ell_2\ell_3}}{\sigma} \simeq \frac{B_{\ell_1\ell_2\ell_3}}{\sqrt{C_{\ell_1}C_{\ell_2}C_{\ell_3}}} \simeq \sqrt{C_\ell} \simeq 10^{-5}, \tag{3.10}
$$

here $\sigma \propto C_\ell C_\ell C_\ell$ is the variance of the bispectrum, we will compute it in section 5.2. Compressing all the bispectrum information into a single, integrated, amplitude parameter is thus the only way to hope to achieve a sufficiently high signal-to-noise ratio for a potentially significant detection. Do not forget, in fact, that the simplest models of Inflation, characterized by slow-roll a single scalar field, predict $f_{NL} \sim 10^{-2}$, while even models allowing in principle "large" non-Gaussianity make predictions[1] for $f_{NL} \sim 1$ to 10. As one can deduce from formula (3.1), a scale-invariant bispectrum will generally be linked to $P_\Phi(k)$ as

$$f_{NL} \sim \frac{B_\Phi(k,k,k)}{P_\Phi^2(k)}. \tag{3.11}$$

In addition to the f_{NL}, theories predict what kind of triangular configurations provide the greatest contribution to the overall signal (i.e. they say on which triangles the bispectrum in peaked), this is encoded in the shape function $F(k_1, k_2, k_3)$. Various Inflationary Models can be classified according to the configurations they mainly generate in the bispectrum. The most common and studied shapes are the *local shape*, the *equilateral shape* and the *orthogonal shape* [16][11].

Local shape This shape covers a wide range of models, including standard single-field slow-roll. However f_{NL} in standard single-field is predicted to be tiny, and undetectable ($f_{NL} \sim 10^{-2}$). Sizable local non-Gaussianities can be produced in Inflationary model with multiple interacting fields. The deduction of large local non-Gaussianities would thus rule out the simplest slow-roll single-field Inflationary scenarios.

The local bispectrum is peaked on "squeezed" configuration with $k_1 \simeq k_2 \gg k_3$. This shape derives from the expansion (3.1) we used earlier to show the suppression of higher order correlator. It's called "local" because non-Gaussianities are typically produced on large super-horizon scales (represented by the smallest k). Since different regions on super-horizon scales cannot interact, non-Gaussianity will not correlate different point in real space. This is evident from (3.1), where the non-Gaussian part of the potential is a *local* functional of the Gaussian part, *i.e.* $\Phi_{NL}(x) = f_{NL}(\Phi_L^2(x) - \langle \Phi_L^2(x) \rangle)$ depends only on the value of $\Phi_L(x)$ in the *same* point. The form of the local shape function is:

$$F(k_1, k_2, k_3) = 2A^2 \left[\frac{1}{k_1^{4-n_s} k_2^{4-n_s}} + \frac{1}{k_1^{4-n_s} k_3^{4-n_s}} + \frac{1}{k_2^{4-n_s} k_3^{4-n_s}} \right], \tag{3.12}$$

here A is the normalization of the Power Spectrum and n_s is the spectral index $P_\Phi(k) = A/k^{n_s-4}$. The reduced local bispectrum is showed in the right panel of figure 3.2.

Equilateral shape For the equilateral bispectrum, the shape function peaks at the equilateral triangle limit $k_1 = k_2 = k_3$ and vanishes as $\sim k_3/k_1$, it has the form:

[1] note that, for this order of magnitude estimate of the strength of the signal, we are defining f_{NL} using expansion (3.1)

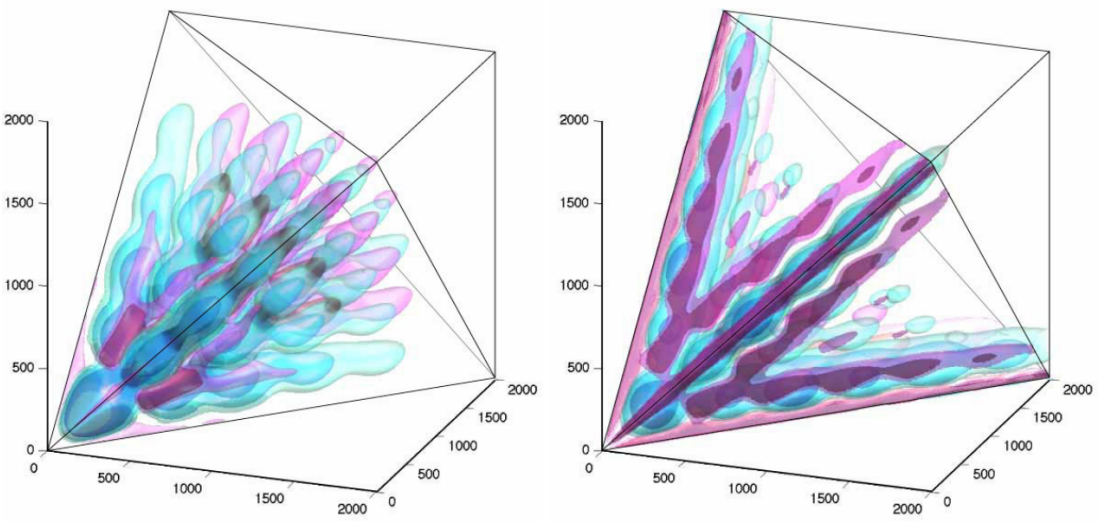

Figure 3.2: Reduced bispectra for equilateral (left) and local (right) models plotted on the tetrahedral region that inscribes the allowed combination of ℓ. On the three axes we have ℓ_1, ℓ_2, ℓ_3, so each point represent a different triangle, with colors defining the amplitude. In this representation, squeezed triangles are along the edges, equilateral triangles along the diagonal, and flattened configurations lie on the faces. The density contours illustrated represent the positive values (light blue) and the negative ones (magenta). This image is taken from [15].

$$F(k_1,k_2,k_3) = 6A^2\Bigg[-\frac{1}{k_1^{4-n_s}k_2^{4-n_s}}-\frac{1}{k_1^{4-n_s}k_3^{4-n_s}}-\frac{1}{k_2^{4-n_s}k_3^{4-n_s}}-\frac{2}{(k_1k_2k_3)^{2(4-n_s)/3}}+ \\ +\left(\frac{1}{k_1^{(4-n_s)/3}k_2^{2(4-n_s)/3}k_3^{(4-n_s)/3}}+5\,\text{perm.}\right)\Bigg]. \tag{3.13}$$

This kind of bispectrum is generated mainly from single-field Inflationary Models with non-standard kinetic terms in the Inflaton Lagrangian. In single field large wavelenght modes are frozen from the moment they leave the horizon, therefore they can not have large interactions with short wavelength modes. On the other hand modes that are still within the horizon average out any contribution to non-Gaussianities with their oscillations. For this reason the signal in squeezed triangles is now suppressed. Therefore the greatest contribution comes from the modes that have similar wavelengths and exit the horizon at about the same time sourcing an equilateral bispectrum signal. The reduced equilateral bispectrum is showed in the left panel of figure 3.2

Orthogonal shape This shape is peaked both on equilateral configurations and flat-triangle configurations (with $k_1 + k_2 \simeq k_3$). The Physical arguments that bring to this shape are the same of the equilateral one. It is derived from the combination of similar-equilateral shapes [44]. It can be approximated by the template:

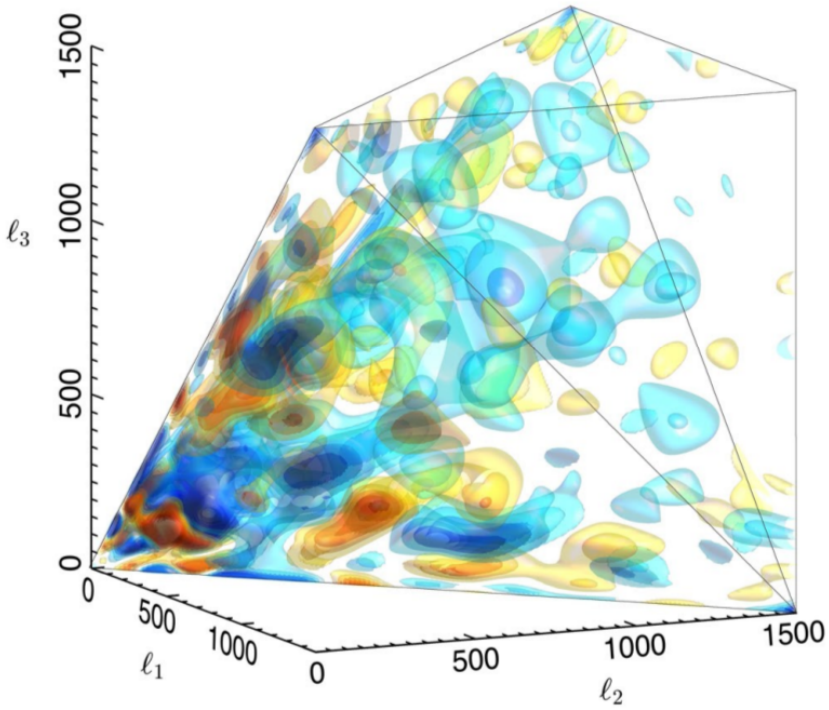

Figure 3.3: *Planck* CMB bispectrum detail in the signal-dominated regime [39].

$$F(k_1,k_2,k_3) = 6A^2\Bigg[-\frac{3}{k_1^{4-n_s}k_2^{4-n_s}}-\frac{3}{k_1^{4-n_s}k_3^{4-n_s}}-\frac{3}{k_2^{4-n_s}k_3^{4-n_s}}-\frac{8}{(k_1k_2k_3)^{2(4-n_s)/3}}+ \\ +\left(\frac{3}{k_1^{(4-n_s)/3}k_2^{2(4-n_s)/3}k_3^{(4-n_s)/3}}+5\,\text{perm.}\right)\Bigg]. \tag{3.14}$$

As an example, in figure 3.3 we report the CMB bispectrum provided by *Planck* dataset, for a detailed discussion on the *Planck* results about the constraints on primordial non-Gaussianity see [39].

3.3 Factorizability

Measurements of the CMB angular bispectrum are a very powerful tool for the detection of primordial non-Gaussianity. However they also present a huge computational challenge. The bispectrum $B^{m_1m_2m_3}_{\ell_1\ell_2\ell_3}$ has six degrees of freedom. Thus its brute-force calculation would scale like $\mathcal{O}(\ell^6_{max})$, that becomes $\mathcal{O}(\ell^5_{max})$ once triangle and parity conditions constraints are kept into account. However this is still huge for a typical modern CMB experiment, with $\ell_{max}\sim 10^3$ or larger. It's now clear that for the analysis of a survey like *Planck*, with $\ell_{max}\sim 2000$, a more efficient method is needed.
The solution is to write the bispectrum in *factorizable* form, allowing to compute three indipendent integral, one in every k_i, instead of a triple one. As we are going to see, in

this way the problem cost reduces to $\mathcal{O}(\ell_{max}^3)$.
A factorizable, or separable form, is defined by an ansatz of the kind:

$$B_\Phi(k_1,k_2,k_3) = f_{NL}F(k_1,k_2,k_3) = f_{NL}\sum_{pqr} c_{pqr}F_p(k_1)F_q(k_2)F_r(k_3) + \text{ perm.} \quad (3.15)$$

To obtain the general form for a separable bispectrum, we shall insert (3.15) in equation (3.8), then expand the dirac delta in plane wave:

$$\delta(\vec{k}_1+\vec{k}_2+\vec{k}_3) = \int \frac{\mathrm{d}^3x}{(2\pi)^3}\; exp\; \imath\big[(\vec{k}_1+\vec{k}_2+\vec{k}_3)\cdot\vec{x}\big], \quad (3.16)$$

and then apply the spherical wave expansion of vector plane wave (for further details see appendix B.2), so we obtain:

$$\begin{aligned}\delta(\vec{k}_1+\vec{k}_2+\vec{k}_3) = (4\pi)^3\int\frac{\mathrm{d}^3x}{(2\pi)^3}\Bigg\{&\Big[\sum_{\ell_1=0}^{\infty}\imath^{\ell_1}j_{\ell_1}(k_1r)\sum_{m_1=-\ell_1}^{\ell_1}\overline{Y}_{\ell_1}^{m_1}(\hat{n}_1)Y_{\ell_1}^{m_1}(\hat{k}_1)\Big]\times\\ &\times\Big[\sum_{\ell_2=0}^{\infty}\imath^{\ell_2}j_{\ell_2}(k_2r)\sum_{m_2=-\ell_2}^{\ell_2}\overline{Y}_{\ell_2}^{m_2}(\hat{n}_2)Y_{\ell_2}^{m_2}(\hat{k}_2)\Big]\times\\ &\times\Big[\sum_{\ell_3=0}^{\infty}\imath^{\ell_3}j_{\ell_3}(k_3r)\sum_{m_3=-\ell_3}^{\ell_3}\overline{Y}_{\ell_3}^{m_3}(\hat{n}_3)Y_{\ell_3}^{m_3}(\hat{k}_3)\Big].\end{aligned} \quad (3.17)$$

Here the coordinate r in the Bessel functions argument represents the lookback conformal time $r = c\tau$. Now returning to the definition (3.7) for the angular bispectrum, we can substitute $\langle\Phi(\vec{k}_1)\Phi(\vec{k}_2)\Phi(\vec{k}_3)\rangle$ with the expanded δ_D and the separable function (3.15), at last we can eliminate the summations recalling the normalization propriety of the spherical harmonics obtaining:

$$\begin{aligned}B_{\ell_1\ell_2\ell_3}^{m_1m_2m_3} =& \left(\frac{2}{\pi}\right)^3\int\mathrm{d}^3x\iiint\mathrm{d}k_1\mathrm{d}k_2\mathrm{d}k_3\,k_1^2k_2^2k_3^2\sum_{pqr}\Big[c_{pqr}F_p^{(1)}(k_1)F_q^{(2)}(k_2)F_r^{(3)}(k_3)\\ &+\; perm.\Big]\Delta_{\ell_1}(k_1,\tau)\Delta_{\ell_2}(k_2,\tau)\Delta_{\ell_3}(k_3,\tau)j_{\ell_1}(k_1r)j_{\ell_2}(k_2r)j_{\ell_3}(k_3r)\times\\ &\times\;\overline{Y_{\ell_1}^{m_1}}(\hat{n_1})\overline{Y_{\ell_2}^{m_2}}(\hat{n_2})\overline{Y_{\ell_3}^{m_3}}(\hat{n_3})\\ =&\,\mathcal{G}_{\ell_1\ell_2\ell_3}^{m_1m_2m_3}\times\left(\frac{2}{\pi}\right)^3\sum_{pqr}\Bigg[\int\;r^2\mathrm{d}r\int k_1^2\mathrm{d}k_1\,F_p^{(1)}(k_1)\Delta_{\ell_1}(k_1,\tau)j_{\ell_1}(k_1r)\times\\ &\times\int k_2^2\mathrm{d}k_2\,F_q^{(2)}(k_2)\Delta_{\ell_2}(k_2,\tau)j_{\ell_2}(k_2r)\times\\ &\times\int k_3^2\mathrm{d}k_3\,F_r^{(3)}(k_3)\Delta_{\ell_3}(k_3,\tau)j_{\ell_3}(k_3r)+perm.\Bigg].\end{aligned} \quad (3.18)$$

This is the general factorized form for the angular bispectrum, $F_{p,q,r}$ are now generic functions, their form and their number depend on the model for the primordial potential.

It is now clear why factorizing the shape allows a strong reduction in computational cost. The triple integral $\mathrm{d}k_1\mathrm{d}k_2\mathrm{d}k_3$, over all configurations, has been written as the product of three *one dimensional* integral over $\mathrm{d}k_1$, $\mathrm{d}k_2$, $\mathrm{d}k_3$, separately. This operation is performed in $\sim \ell_{max}$ operations instead of the original $\sim \ell_{max}^3$ operations. Whit $\ell_{max} \sim 10^3$ this is a huge gain, making the problem numerically tractable.
Most shapes are originally non separable, we have so to derive suitable separable approximations. Finding a separable approximation for the special case of a scale-dependent amplitude is the aim of this thesis, our results are showed in the next chapter in section 4.1.

3.3.1 A Worked Example: Local Shape

In order to show a concrete application, and clarify the formalism introduced in the first part of this Chapter, we will now show how to compute the CMB angular bispectrum predicted by primordial local NG models. As we saw earlier, the local model is defined by the real space potential:

$$\Phi(x) = \Phi_L(x) + f_{NL}\left(\Phi_L(x) - \langle\Phi_L^2(x)\rangle\right), \tag{3.19}$$

where $\Phi_L(x)$ is the linear part of the potential in real space; similarly in the Fourier space it becomes:

$$\Phi(\vec{k}) = \Phi_L(\vec{k}) + \Phi_{NL}(\vec{k}), \tag{3.20}$$

from which follows:

$$a_{\ell m} = a_{\ell m}^L + a_{\ell m}^{NL}, \tag{3.21}$$

in this way the non-Gaussianity is handled as a little "perturbation" from the linear regime. With this in mind we can develop the bispectrum (3.2):

$$B_{\ell_1\ell_2\ell_3}^{m_1m_2m_3} = \langle(a_{\ell_1m_1}^L + a_{\ell_1m_1}^{NL})(a_{\ell_2m_2}^L + a_{\ell_2m_2}^{NL})(a_{\ell_3m_3}^L + a_{\ell_3m_3}^{NL})\rangle, \tag{3.22}$$

ignoring the terms beyond the second order in $a_{\ell m}^{NL}$, remembering that the bispectrum is null for the Gaussian part (so that $\langle a_{\ell m}^L a_{\ell m}^L a_{\ell m}^L\rangle = 0$), we can write:

$$B_{\ell_1\ell_2\ell_3}^{m_1m_2m_3} = \langle a_{\ell_1m_1}^L a_{\ell_2m_2}^L a_{\ell_3m_3}^{NL}\rangle + \langle a_{\ell_1m_1}^L a_{\ell_2m_2}^{NL} a_{\ell_3m_3}^L\rangle + \langle a_{\ell_1m_1}^{NL} a_{\ell_2m_2}^L a_{\ell_3m_3}^L\rangle. \tag{3.23}$$

The non-linear part $\Phi_{NL}(k)$ is defined by:

$$\Phi_{NL} \equiv f_{NL}\left[\int \frac{\mathrm{d}^3p}{(2\pi)^3}\Phi_L(\vec{k}+\vec{p})\overline{\Phi_L(\vec{p})} - (2\pi)^3\delta_D(\vec{k})\langle\Phi_L^2(\vec{x})\rangle\right], \tag{3.24}$$

from which it derives:

$$a_{\ell m}^L = (-\imath)^\ell 4\pi \int \mathrm{d}^3k\Phi_L(\vec{k})\Delta(k,\tau)\overline{Y_\ell^m}(\hat{k}) \tag{3.25}$$

$$a_{\ell m}^{NL} = (-\imath)^\ell 4\pi \int \mathrm{d}^3k\Phi_{NL}(\vec{k})\Delta(k,\tau)\overline{Y_\ell^m}(\hat{k}). \tag{3.26}$$

Then the resulting bispectrum will consist of a sum of terms of the kind:

$$
\begin{aligned}
&\langle a^{L}_{\ell_1 m_1} a^{L}_{\ell_2 m_2} a^{NL}_{\ell_3 m_3}\rangle = \\
&= (i)^{\ell_1+\ell_2+\ell_3}(4\pi)^3\Big\langle \iiint \mathrm{d}^3k_1\mathrm{d}^3k_2\mathrm{d}^3k_3\Phi_L(\vec{k_1})\Delta(k_1,\tau)\overline{Y^{m_1}_{\ell_1}}(\hat{k_1})\Phi_L(\vec{k_2})\Delta(k_2,\tau)\overline{Y^{m_2}_{\ell_2}}(\hat{k_2})\times \\
&\quad\times \Phi_{NL}(\vec{k_3})\Delta(k_3,\tau)\overline{Y^{m_3}_{\ell_3}}(\hat{k_3})\Big\rangle \\
&= (4\pi)^3\iiint \mathrm{d}^3k_1\mathrm{d}^3k_2\mathrm{d}^3k_3\langle\Phi_L(\vec{k_1})\Phi_L(\vec{k_2})\Phi_{NL}(\vec{k_3})\rangle\Delta(k_1,\tau)\Delta(k_2,\tau)\Delta(k_3,\tau)\times \\
&\quad\times \overline{Y^{m_1}_{\ell_1}}(\hat{k_1})\overline{Y^{m_2}_{\ell_2}}(\hat{k_2})\overline{Y^{m_3}_{\ell_3}}(\hat{k_3}).
\end{aligned}
\tag{3.27}
$$

The interesting element in (3.27) is the three-field correlator $\langle\Phi_L(\vec{k_1})\Phi_L(\vec{k_2})\Phi_{NL}(\vec{k_3})\rangle$, applying the Wick theorem:

$$
\langle\Phi_1\Phi_2\Phi_3\Phi_4\rangle = \langle\Phi_1\Phi_2\rangle\langle\Phi_3\Phi_4\rangle + \langle\Phi_1\Phi_4\rangle\langle\Phi_2\Phi_3\rangle + \langle\Phi_1\Phi_3\rangle\langle\Phi_2\Phi_4\rangle,
\tag{3.28}
$$

and the definition (3.24) we can write:

$$
\begin{aligned}
&\langle\Phi_L(\vec{k_1})\Phi_L(\vec{k_2})\Phi_{NL}(\vec{k_3})\rangle = \\
=&f_{NL}\Bigg[\int\frac{\mathrm{d}^3p}{(2\pi)^3}\langle\Phi_L(\vec{k_1})\Phi_L(\vec{k_2})\Phi_L(\vec{k_3}+\vec{p})\overline{\Phi_L}(\vec{p})\rangle - (2\pi)^3\delta_D(\vec{k_3})\langle\Phi_L(\vec{k_1})\Phi_L(\vec{k_2})\rangle\langle\Phi^2_L(\vec{x})\rangle\Bigg] \\
=&f_{NL}\Bigg[\int\frac{\mathrm{d}^3p}{(2\pi)^3}\Big(\langle\Phi_L(\vec{k_1})\Phi_L(\vec{k_2})\rangle\langle\Phi_L(\vec{k_3}+\vec{p})\overline{\Phi_L}(\vec{p})\rangle + \langle\Phi_L(\vec{k_1})\Phi_L(\vec{k_3}+\vec{p})\rangle\langle\Phi_L(\vec{k_2})\overline{\Phi_L}(\vec{p})\rangle \\
&+\langle\Phi_L(\vec{k_1})\overline{\Phi_L}(\vec{p})\rangle\langle\Phi_L(\vec{k_2})\Phi_L(\vec{k_3}+\vec{p})\rangle\Big) - (2\pi)^3\langle\Phi_L(\vec{k_1})\Phi_L(\vec{k_2})\rangle\delta^{(3)}_D(\vec{k_3})\int\mathrm{d}^3\vec{k_3}P_\Phi(k_3)\Bigg].
\end{aligned}
\tag{3.29}
$$

Then applying the following relations:

$$
\begin{aligned}
\langle\Phi_L(\vec{k_1})\Phi_L(\vec{k_2})\rangle &= (2\pi)^3P_\Phi(k_1)\delta^{(3)}_D(\vec{k_1}+\vec{k_2}) \\
\langle\Phi_L(\vec{k_3}+\vec{p})\overline{\Phi_L}(\vec{p})\rangle &\equiv \langle\Phi_L(\vec{p})\overline{\Phi_L}(\vec{p}-\vec{k_3})\rangle = (2\pi)^3P_\Phi(p)\delta^{(3)}_D(\vec{k_3}) \\
\langle\Phi^2_L(\vec{x})\rangle &= \frac{1}{2(\pi)^3}\int\mathrm{d}^3\vec{k_3}P_\Phi(k_3),
\end{aligned}
$$

we obtain:

$$
\begin{aligned}
\langle\Phi_L(\vec{k_1})\Phi_L(\vec{k_2})\Phi_{NL}(\vec{k_3})\rangle = f_{NL}\Bigg[&(2\pi)^3P_\Phi(k_1)\delta^{(3)}_D(\vec{k}_1+\vec{k}_2+\vec{k}_3)\int\mathrm{d}^3\vec{p}\,P_\Phi(p)+ \\
&+(2\pi)^3P_\Phi(k_1)P_\Phi(k_2)\int\mathrm{d}^3\vec{p}\;\delta^{(3)}_D(\vec{k}_1+\vec{k}_3+\vec{p})\delta^{(3)}_D(\vec{k}_2-\vec{p})+ \\
&+(2\pi)^3P_\Phi(k_1)P_\Phi(k_2)\int\mathrm{d}^3\vec{p}\;\delta^{(3)}_D(\vec{k}_2+\vec{k}_3+\vec{p})\delta^{(3)}_D(\vec{k}_1-\vec{p})+ \\
&-(2\pi)^3P_\Phi(k_1)\delta^{(3)}_D(\vec{k}_1+\vec{k}_2+\vec{k}_3)\int\mathrm{d}^3\vec{k_3}\;P_\Phi(k_3)\Bigg].
\end{aligned}
\tag{3.30}
$$

The first and the last term cancel each other out, solving the remaining integral we obtain:

$$\begin{aligned}
&\langle \Phi_L(\vec{k_1})\Phi_L(\vec{k_2})\Phi_{NL}(\vec{k_3})\rangle = \\
&= f_{NL}\Big[(2\pi)^3 P_\Phi(k_1)P_\Phi(k_2)\delta_D^{(3)}(\vec{k}_1+\vec{k}_2+\vec{k}_3) + (2\pi)^3 P_\Phi(k_1)P_\Phi(k_2)\delta_D^{(3)}(\vec{k}_1+\vec{k}_2+\vec{k}_3)\Big] \\
&= (2\pi)^3 f_{NL} P_\Phi(k_1)P_\Phi(k_2)\delta_D^{(3)}(\vec{k}_1+\vec{k}_2+\vec{k}_3),
\end{aligned} \tag{3.31}$$

therefore the primordial separable bispectrum is:

$$B_\Phi(k_1,k_2,k_3) = (2\pi)^3\delta_D^{(3)}(\vec{k}_1+\vec{k}_2+\vec{k}_3) f_{NL}\left(P_\Phi(k_1)P_\Phi(k_2) + 2\,perm\right). \tag{3.32}$$

Comparing this result with (3.8) it's easy to identify the same structure we have already derived for the primordial bispectrum, with the δ_D which determines the geometrical proprieties and a function of the wave vectors ("Shape"), here the power spectra combination.
For this specific case, we see that the primordial bispectrum is already written in separable form. We can now use formula (3.18), with the functions F_p, F_q, F_r trivially expressed as:

$$\begin{aligned}
F_p(k) &= F_q(k) = P_\Phi(k), \\
F_r(k) &= 1,
\end{aligned}$$

to obtain:

$$\begin{aligned}
B^{m_1m_2m_3}_{\ell_1\ell_2\ell_3} =& \mathcal{G}^{m_1m_2m_3}_{\ell_1\ell_2\ell_3} \times \left(\frac{2}{\pi}\right)^3 f_{NL}\sum_{pqr}\Bigg[\int r^2\mathrm{d}r \int k_1^2\mathrm{d}k_1\, P_\Phi(k_1)\Delta_{\ell_1}(k_1,\tau)j_{\ell_1}(k_1r)\times \\
&\times \int k_2^2\mathrm{d}k_2\, P_\Phi(k_2)\Delta_{\ell_2}(k_2,\tau)j_{\ell_2}(k_2r)\int k_3^2\mathrm{d}k_3\,\Delta_{\ell_3}(k_3,\tau)j_{\ell_3}(k_3r) + 2\,perm.\Bigg].
\end{aligned} \tag{3.33}$$

This result can be recast in a more readable form through the definition of the coefficients:

$$\alpha_\ell(r) \equiv \frac{2}{\pi}\int_0^\infty k^2\mathrm{d}k\,\Delta_\ell(k,\tau)j_\ell(kr), \tag{3.34}$$

$$\beta_\ell(r) \equiv \frac{2}{\pi}\int_0^\infty k^2\mathrm{d}k\,P_\Phi(k)\Delta_\ell(k,\tau)j_\ell(kr). \tag{3.35}$$

We can now write the reduced bispectrum (3.3) for the local model in a separable and computationally efficient form:

$$b^{loc}_{\ell_1\ell_2\ell_3} = 2f_{NL}\int_0^\infty r^2\mathrm{d}r\,\left[\alpha_{\ell_1}\beta_{\ell_2}\beta_{\ell_3} + \alpha_{\ell_2}\beta_{\ell_3}\beta_{\ell_1} + \alpha_{\ell_3}\beta_{\ell_1}\beta_{\ell_2}\right], \tag{3.36}$$

where, for simplicity of notation, we have omitted to write explicitly the r-dependence of quantities in the integral above. This bispectrun is showed in figure (3.9). It is evidently weighted on the corners of the tetrahedral region representing the allowed combinations. This is expected from the fact that it peaks on the squeezed configuration with two large ℓ and the third much smaller.
For all the shapes introduced earlier there is a similar expression for the reduced bispectrum, the difference is only in the number of coefficients. For example, to express the equilateral function two more coefficients are needed [29]:

$$\gamma_\ell(r) \equiv \frac{2}{\pi}\int_0^\infty k^2 \mathrm{d}k\, P_\Phi(k)^{\frac{1}{3}} \Delta_\ell(k,\tau) j_\ell(kr), \tag{3.37}$$

$$\delta_\ell(r) \equiv \frac{2}{\pi}\int_0^\infty k^2 \mathrm{d}k\, P_\Phi(k)^{\frac{2}{3}} \Delta_\ell(k,\tau) j_\ell(kr), \tag{3.38}$$

and the expression for the equilateral bispectrum is:

$$b^{equil}_{\ell_1\ell_2\ell_3} = f_{NL}\int_0^\infty r^2 \mathrm{d}r\ [2\delta_{\ell_1}\delta_{\ell_2}\delta_{\ell_3} + (\alpha_{\ell_1}\beta_{\ell_2}\beta_{\ell_3} + 2\,\text{perm.}) + (\beta_{\ell_1}\gamma_{\ell_2}\delta_{\ell_3} + 5\,\text{perm.})] \tag{3.39}$$

This bispectrun is showed in figure (3.2) left panel, note that it is center-weighted due to the fact that it peaks on equilateral configuarations $\ell_1 \simeq \ell_2 \simeq \ell_3$.

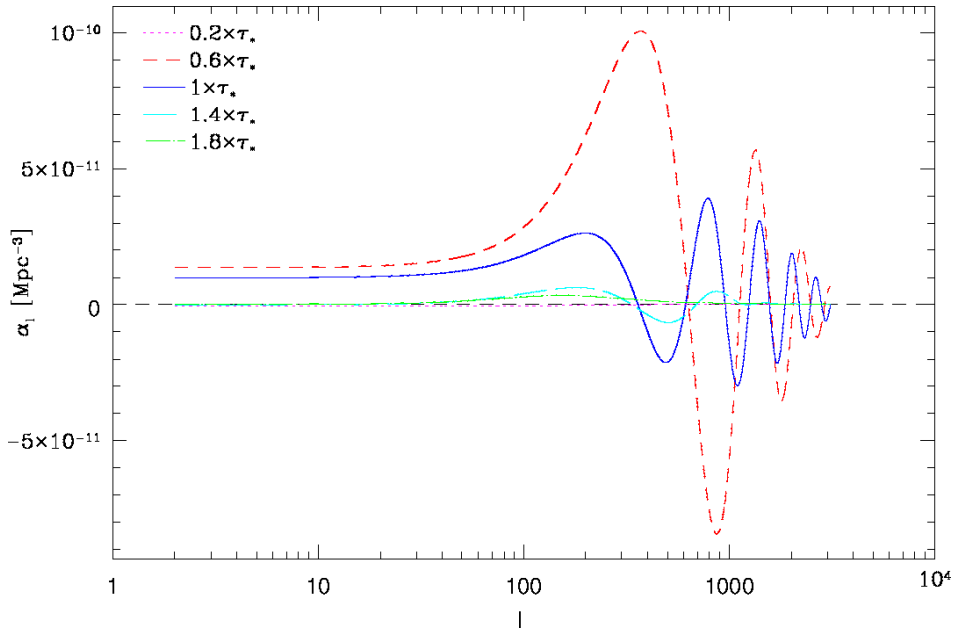

Figure 3.4: The coefficient $\alpha_\ell(r)$ defined in (3.34). The different lines refers to different value of $r = c(\tau_0 - \tau)$ defined as function of the recombination conformal time τ_*, τ_0 is the present conformal time. For our cosmological model $c\tau_* = 280.75 Mpc$.

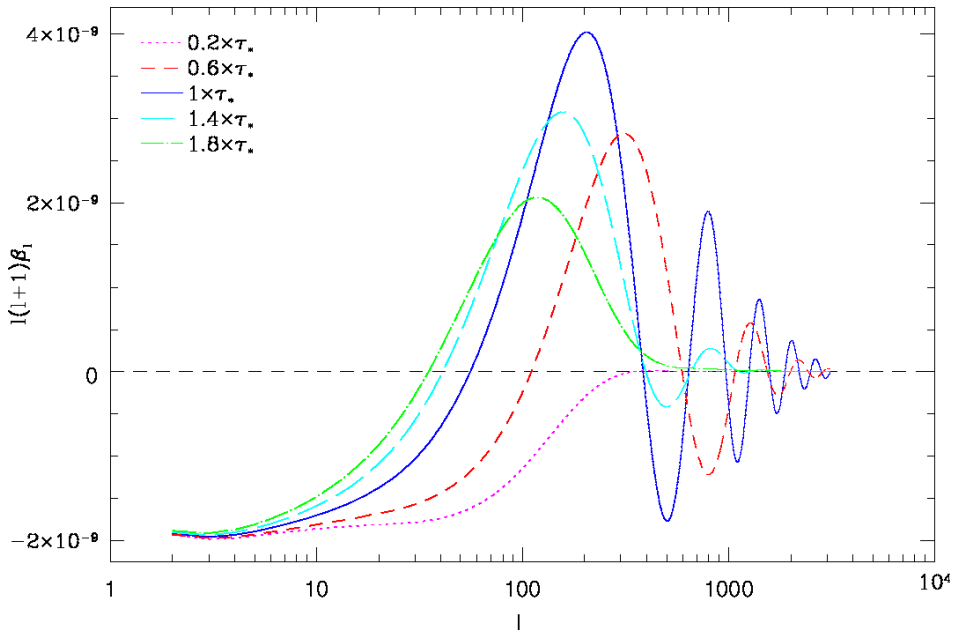

Figure 3.5: The coefficient $\beta_\ell(r)$ defined in (3.35). The different lines refers to different value of $r = c(\tau_0 - \tau)$ defined as function of the recombination conformal time τ_*, τ_0 is the present conformal time. For our cosmological model $c\tau_* = 280.75 Mpc$.

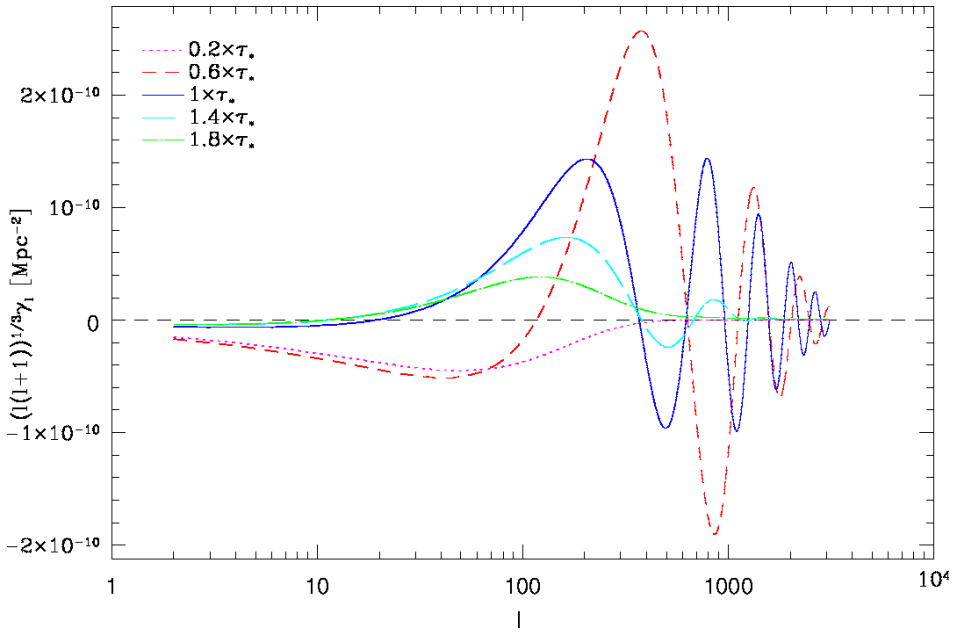

Figure 3.6: The coefficient $\gamma_\ell(r)$ defined in (3.37). The different lines refers to different value of $r = c(\tau_0 - \tau)$ defined as function of the recombination conformal time τ_*, τ_0 is the present conformal time. For our cosmological model $c\tau_* = 280.75 Mpc$

.

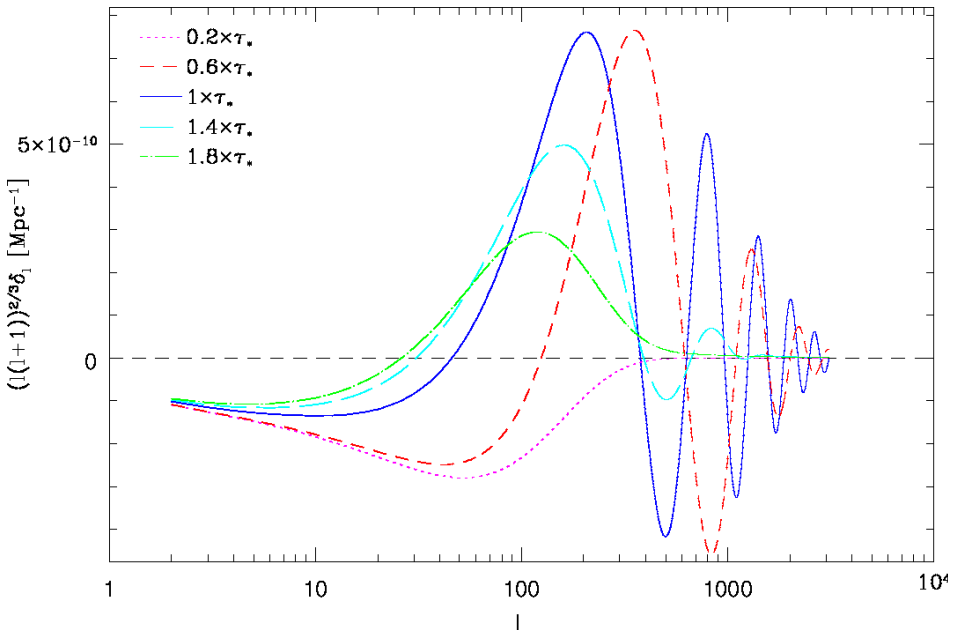

Figure 3.7: The coefficient $\delta_\ell(r)$ defined in (3.38). The different lines refers to different value of $r = c(\tau_0 - \tau)$ defined as function of the recombination conformal time τ_*, τ_0 is the present conformal time. For our cosmological model $c\tau_* = 280.75 Mpc$.

Chapter 4

Scale Dependence

Until now we have supposed the amplitude parameter f_{NL} to be scale-independent, however there exists a certain number of models which produce potentially significant variations of the amplitude over the range of scales accessible by modern observations [43]. A scale independent f_{NL} implies that the degree of non-Gaussianity remains constant at all scales. The detection of a running of this parameter would provide completely new information about the physical processes taking place in the primordial Universe. Both equilateral and local models are predicted to show a significant running of f_{NL} under certain assumption; for example single-field theory with variable speed of sound provides an equilateral shape function with scale-dependence.
In this work we develop the models described above including a scale-dependent bispectrum amplitude. To parametrize the initial bispectrum we replace the amplitude parameter with:

$$f_{NL} \to f_{NL} \left(\frac{k_1 + k_2 + k_3}{\mathbf{k}_{piv}} \right)^{n_{NG}}, \tag{4.1}$$

where n is the *running parameter*, $\mathbf{k}_{piv}$ is a pivot scale needed to constrain the amplitude. This new form however affects the factorizability of the bispectrum since it is not separable. The main point of this thesis was to find a parametrization that allows us to write this bispectrum in separable form.
A first study was made by Sefusatti et al. in [43] replacing $(k_1 + k_2 + k_3)^{n_{NG}}$ with $(k_1 k_2 k_3)^{n_{NG}}$. This form is expected to work reasonably well in the equilateral case, but probably it is inadequate for the local shape. The accuracy of this choice has not yet been checked in details; moreover, with current high sensitivity surveys like *Planck*, we need extremely high accuracy in the theoretical model to fit to the data.
All this motivate to search for a more accurate analytical description of these kind of shapes. This will be the subject of the rest of this chapter.

4.1 Analitical Results

The factor $(k_1 + k_2 + k_3)^{n_{NG}}$ is not trivially factorizable. To elude this problem we assume (without loss of generality, since running of non-Gaussianity is already known

to be small, if present) n_{NG} to be lesser than one and we replace it with the parameter $s = 1 - n_{NG}$, so the factor becomes:

$$(k_1 + k_2 + k_3)^n = \frac{(k_1 + k_2 + k_3)}{(k_1 + k_2 + k_3)^s}, \tag{4.2}$$

in this form we can replace the denominator resorting to the Schwinger parametrization[1]:

$$\frac{(k_1 + k_2 + k_3)}{(k_1 + k_2 + k_3)^s} = (k_1 + k_2 + k_3)\frac{1}{\Gamma(s)}\int_0^\infty \mathrm{d}t\, t^{s-1} e^{-t(k_1+k_2+k_3)}. \tag{4.3}$$

Looking at this equation it's clear that it is the form we are searching for; the k_i dependence comes only from separable functions: the summation in the round brackets and the exponential terms. Using this expression we finally obtain the factorized form

$$f_{NL} \to \frac{f_{NL}}{\mathbf{k}_{piv}^{n_{NG}}}\frac{1}{\Gamma(1-n_{NG})}\int_0^\infty \mathrm{d}t\, t^{-n_{NG}}\left[k_1 e^{-t(k_1+k_2+k_3)} + 2\,\text{perm.}\right]. \tag{4.4}$$

To obtain a reduced bispectrum expression with scale-dependence we have to replace f_{NL} with this new definition, and put it in separable form, defining new coefficients. For the local shape we compute:

$$\begin{aligned}
\alpha_\ell(r,t) &= \frac{2}{\pi}\int \mathrm{d}k\, k^2 \Delta_\ell(k) j_\ell(kr) e^{-tk}, &(4.5)\\
\beta_\ell(r,t) &= \frac{2}{\pi}\int \mathrm{d}k\, k^2 P_\Phi(k) \Delta_\ell(k) j_\ell(kr) e^{-tk}, &(4.6)\\
\zeta_\ell(r,t) &= \frac{2}{\pi}\int \mathrm{d}k\, k^3 \Delta_\ell(k) j_\ell(kr) e^{-tk}, &(4.7)\\
\xi_\ell(r,t) &= \frac{2}{\pi}\int \mathrm{d}k\, k^3 P_\Phi(k) \Delta_\ell(k) j_\ell(kr) e^{-tk}. &(4.8)
\end{aligned}$$

Starting from equation (3.33), with this new coefficients, we can write the reduced scale-dependent local bispectrum:

$$\begin{aligned}
b^{loc}_{\ell_1\ell_2\ell_3} = \frac{f_{NL}}{\mathbf{k}_{piv}^{n_{NG}}}\frac{1}{\Gamma(1-n_{NG})}\int_0^\infty \mathrm{d}t\, t^{-n_{NG}}\int_0^\infty \mathrm{d}r\, r^2 \Big[\Big(\alpha_{\ell_1}(r,t)\beta_{\ell_2}(r,t)\xi_{\ell_3}(r,t) + 5\,\text{perm.}\Big) + \\
+\Big(\beta_{\ell_1}(r,t)\beta_{\ell_2}(r,t)\zeta_{\ell_3}(r,t) + 2\,\text{perm.}\Big)\Big]. \qquad (4.9)
\end{aligned}$$

To obtain the same results in the equilateral case we need to define other four additional coefficients:

[1] The Schwinger parametrization is a technique developed to evaluate loop integrals in quantum field theory.

$$\gamma_\ell(r,t) \equiv \frac{2}{\pi}\int_0^\infty k^2 \mathrm{d}k\, P_\Phi(k)^{\frac{1}{3}} \Delta_\ell(k,\tau) j_\ell(kr) e^{-tk}, \tag{4.10}$$

$$\delta_\ell(r,t) \equiv \frac{2}{\pi}\int_0^\infty k^2 \mathrm{d}k\, P_\Phi(k)^{\frac{2}{3}} \Delta_\ell(k,\tau) j_\ell(kr) e^{-tk}, \tag{4.11}$$

$$\epsilon_\ell(r,t) \equiv \frac{2}{\pi}\int_0^\infty k^3 \mathrm{d}k\, P_\Phi(k)^{\frac{1}{3}} \Delta_\ell(k,\tau) j_\ell(kr) e^{-tk}, \tag{4.12}$$

$$\eta_\ell(r,t) \equiv \frac{2}{\pi}\int_0^\infty k^3 \mathrm{d}k\, P_\Phi(k)^{\frac{2}{3}} \Delta_\ell(k,\tau) j_\ell(kr) e^{-tk}. \tag{4.13}$$

Inserting (4.4) in (3.39) and using all these new coefficients we obtain the reduced equilateral bispectrum:

$$\begin{aligned} b^{equil}_{\ell_1\ell_2\ell_3} =& \frac{f_{NL}}{\mathbf{k}_{piv}^{n_{NG}}} \frac{1}{\Gamma(1-n_{NG})} \int_0^\infty \mathrm{d}t\, t^{-n_{NG}} \int_0^\infty \mathrm{d}r\, r^2 \Big[2\big(\eta_1\delta_2\delta_3 + 2\,\text{perm.}\big) + \\ &+ \big(\zeta_1\beta_2\beta_3 + 2\,\text{perm.}\big) + \big(\alpha_1\xi_2\beta_3 + 5\,\text{perm.}\big) + \big(\xi_1\gamma_2\delta_3 + 5\,\text{perm.}\big) + \\ &+ \big(\beta_1\epsilon_2\delta_3 + 5\,\text{perm.}\big) + \big(\beta_1\gamma_2\eta_3 + 5\,\text{perm.}\big) \Big], \end{aligned} \tag{4.14}$$

where we adopted a more compact notation removing the explicit dependence on (r,t) in the integrand terms, due to to space limitations. However, to avoid any misunderstanding we emphasize that these coefficients are those defined by equations from (4.5) to (4.13).

4.2 Sachs-Wolfe Approximation

As we saw in the previous chapter, if we consider only the Sachs-Wolfe effect the transfer function is very simple to compute:

$$\Delta_\ell = \frac{1}{3} j_\ell(kr), \tag{4.15}$$

without the scale dependence ansatz the local shape function can be solved analytically thanks to the properties of the spherical Bessel functions (see the Appendix B.2). Taking the Harrison-Zel'dovich-Peebles power spectrum $P_\Phi(k) = Ak^{-3}$, and using the Bessel function closure relation, the coefficients (3.34) and (3.35) become:

$$\alpha_\ell(r) = \frac{2}{3\pi}\int_0^\infty k^2 \mathrm{d}k\, j_\ell(kr_*) j_\ell(kr) = \frac{1}{3r^2}\delta(r - r*), \tag{4.16}$$

$$\beta_\ell(r) = A\frac{2}{3\pi}\int_0^\infty k^{-1} \mathrm{d}k\, j_\ell^2(kr) = \frac{A}{3\pi}\frac{1}{\ell(\ell+1)}, \tag{4.17}$$

and the standard scale-independent local bispectrum reduces to a simple analytic expression:

$$b^{loc,SW}_{\ell_1\ell_2\ell_3} = f_{NL}\frac{2}{27\pi^2}A^2\Bigg[\left(\frac{1}{\ell_1(\ell_1+1)}\,\frac{1}{\ell_2(\ell_2+1)}\right)+\left(\frac{1}{\ell_1(\ell_1+1)}\,\frac{1}{\ell_3(\ell_3+1)}\right)+ + \left(\frac{1}{\ell_3(\ell_3+1)}\,\frac{1}{\ell_2(\ell_2+1)}\right)\Bigg], \tag{4.18}$$

we can express this equation in therms of C_ℓ^{SW} (2.21):

$$b^{loc,SW}_{\ell_1\ell_2\ell_3} = 6f_{NL}\left(C^{SW}_{\ell_1}C^{SW}_{\ell_2} + C^{SW}_{\ell_1}C^{SW}_{\ell_3} + C^{SW}_{\ell_2}C^{SW}_{\ell_3}\right). \tag{4.19}$$

In the scale-dependent case, even if we work in Sachs-Wolfe regime, there isn't a trivial analytical expression, however there is still the advantage of not having to compute the full transfer function and of the drastic reduction in the number or r-evaluations in the numerical implementation of formulae (4.20) and (4.27). This is due to the fact that the particular form of the Sachs-Wolfe transfer function makes the integrals below very narrowly peaked around the recombination value r_*. The coefficients α_ℓ would be a Dirac delta in absence of the exponential term, as it can be seen in formula (4.16). In the scale-dependent case, we no longer strictly have this behavior, but the coefficient does remain narrowly peaked on its recombination value. We can the compute Sachs-Wolfe bispectra integrating on a narrow interval of r around the recombination value r_*, instead of integrating on the full history of the Universe. The new coefficients in Sachs-Wolfe regime are so:

$$\alpha_\ell(r,t) = \frac{2}{3\pi}\int \mathrm{d}k\, k^2 j_\ell(kr)j_\ell(kr_*)e^{-tk}, \tag{4.20}$$

$$\beta_\ell(r,t) = \frac{2}{3\pi}A\int \mathrm{d}k\, k^{n_s-2} j_\ell(kr)j_\ell(kr_*)e^{-tk}, \tag{4.21}$$

$$\zeta_\ell(r,t) = \frac{2}{3\pi}\int \mathrm{d}k\, k^3 j_\ell(kr)j_\ell(kr_*)e^{-tk}, \tag{4.22}$$

$$\xi_\ell(r,t) = \frac{2}{3\pi}A\int \mathrm{d}k\, k^{n_s-1} j_\ell(kr)j_\ell(kr_*)e^{-tk}, \tag{4.23}$$

$$\gamma_\ell(r,t) = \frac{2}{3\pi}A^{\frac{1}{3}}\int \mathrm{d}k\, k^{\frac{1}{3}(n_s+2)} j_\ell(kr)j_\ell(kr_*)e^{-tk}, \tag{4.24}$$

$$\delta_\ell(r,t) = \frac{2}{3\pi}A^{\frac{2}{3}}\int \mathrm{d}k\, k^{\frac{2}{3}(n_s-1)} j_\ell(kr)j_\ell(kr_*)e^{-tk}, \tag{4.25}$$

$$\epsilon_\ell(r,t) = \frac{2}{3\pi}A^{\frac{1}{3}}\int \mathrm{d}k\, k^{\frac{1}{3}(n_s+5)} j_\ell(kr)j_\ell(kr_*)e^{-tk}, \tag{4.26}$$

$$\eta_\ell(r,t) = \frac{2}{3\pi}A^{\frac{2}{3}}\int \mathrm{d}k\, k^{\frac{1}{3}(2n_s+1)} j_\ell(kr)j_\ell(kr_*)e^{-tk}, \tag{4.27}$$

where n_s is the tilt of the power spectrum.
In the next chapter we provide a comprehensive description of how we numerically implemented these results.

Chapter 5

Analysis

In the previous chapter we have derived an exact separable expansion for local and equilateral bispectra with running on the amplitude parameter. Our aim is to use this expansion to compute scale-dependent bispectra numerically and derive forecast on the detectability of f_{NL} and n_{NG} for a WMAP-like experiment[1].
A widely used approach to forecasting in cosmology is the so called *Fisher matrix analysis*. Before showing our results we will then make a brief digression to summarize some basic concepts in statistic, and define what a Fisher matrix is, and how it can be used to our purpose. For a wider description of these methods see *e.g.* [24].

5.1 Statistical Techniques

The starting point for most problems of parameter inference in statistic is the so called *Likelihood Function* $\mathcal{L}$. Assume we have a theoretical model depending on a set of parameters $\{\lambda_i\}$. We also have a set of measurement $\{x_i\}$, and our data depend on the parameter we want to estimate. We denote the probability of A given B as $P[A|B]$, so that we define the Likelihood function as:

$$\mathcal{L} = P[x|\lambda_i], \tag{5.1}$$

it represents the probability to get a certain data given the parameter. Before carrying out our experiment we have some preliminary degree of knowledge of the parameter we want to measure. This is described in terms of a starting probability distribution $P[\lambda_i]$, wich is called the *prior* [2]. If we have no preliminary information on the parameters we want to measure (as it is often the case), then we can define an uninformative prior, expressing the fact that we do not have any preference for picking some specific value of a parameter over the others. In many cases, it is intuitive to see how a totally uninformative prior is simply a uniform distribution over the allowed range of λ_i, that

[1] The same formalism readily apply to higher resolution experiments as *Planck*. However in this preliminary analysis we work at lower resolution, due to the high computational requirement of a high resolution analysis

[2] In our treatment we are defining probability as a "degree of belief", and treating parameters as random variables. That defines the so called *Bayesian* approach to parameters inference, as opposed to the "frequentist" approach, where parameters are just numbers, probability is defined as the frequency of occurrence of an event over many trials, and the concept of a parameter prior simply cannot be defined

is $P[\lambda_i] = k$, where k is a constant used to normalize $P[\lambda_i]$ to 1 over the domain $[\lambda_{min}, \lambda_{max}]$. Given two random variables A and B the *Bayes theorem* states that:

$$P[A|B] = \frac{P[B|A]P[A]}{P[B]}. \tag{5.2}$$

We can apply this crucial result to our problem, in order to get the probability distribution of our parameter, given the measured Likelihood and the prior:

$$P[\lambda_i|x] = \frac{P[x|\lambda_i]P[\lambda_i]}{P[x]}, \tag{5.3}$$

where $P[\lambda_i]$ is the prior and $P[x]$ is called *evidence* and simply acts as normalization. Since it is independent of the parameters, the evidence can be omitted as long as we are concerned with parameter inference problems. The probability distribution of the parameters given the data, is called *posterior*. A natural estimate of λ_i is the the choice which maximizes the posterior. Note that, if we have an uniform prior from (5.3) we can write:

$$P[x|\lambda_i] = \mathcal{L} \propto P[\lambda_i|x]. \tag{5.4}$$

That means that the choice of the parameters which maximizes the posterior is also the one that maximizes the Likelihood. Our parameter estimator is thus a *Maximum Likelihood* estimator. This estimator plays a crucial role in parameters inference, as can be shown that in many case it is the "Best Unbiased Estimator" (BUE) of a set of parameters given the data. Unbiased means that the average is equal to the true value of the parameter. "Best" means that it gives the most accurate estimate of the parameters, in a sense that we are now going to clarify better in order to define the uncertainty on the parameters, or rather the "error bars" (we stressed that we are still assuming an uniform prior). Our estimate is derived from the peak of the Likelihood, so its natural to assume, as a measurement of the precision of our measurement, the width of the Likelihood itself, determined in its maximum. The "width" is nothing else than the curvature of the Likelihood: if it is strongly peaked,*i.e.* the curvature is large, the errors on the estimates will be smaller. On the contrary, if around the peak the Likelihood is rather flat,*i.e.* the curvature is small, it means that the errors are larger. Performing a Taylor expansion of the logarithm of the Likelihood around the peak values $\{\hat{\lambda}_i\}$ we can approximate it with a multivariate Gaussian:

$$\ln \mathcal{L}(x, \lambda) = \ln \mathcal{L}(x, \hat{\lambda}) + \frac{1}{2}(\lambda_i - \hat{\lambda}_i)\frac{\partial^2 \ln \mathcal{L}}{\partial \lambda_i \partial \lambda_j}(\lambda_j - \hat{\lambda}_j), \tag{5.5}$$

from which it derives:

$$\mathcal{L}(x, \lambda) = \mathcal{L}(x, \hat{\lambda}) \exp\left[\frac{1}{2}(-\lambda_i - \hat{\lambda}_i)H_{ij}(\lambda_j - \hat{\lambda}_j)\right]. \tag{5.6}$$

Here $H_{ij} = -\frac{\partial^2 \ln \mathcal{L}}{\partial \lambda_i \partial \lambda_j}$ is the *Hessian matrix*, which quantifies the curvature of the Likelihood, so it is the key to compute the uncertainties on the parameter. The Hessian matrix quantifies also how much the estimates on the parameters λ_i and λ_j are correlated, if it is diagonal the measurements of the two parameters are uncorrelated. Note that this

doesn't means that the parameters itself are correlated, but that so are their estimates: for example the parameters can be completely independent but they can have a similar effect on the data.
If we fix all the parameters except one, or equivalently if we consider the case of a totally independent estimate on a parameter, the error is given by the curvature along the axes representing this parameter (in parameter space), this is called *conditional error* and is defined by:

$$\sigma_{cond,i} = \frac{1}{\sqrt{H_{ii}}}, \tag{5.7}$$

however this error is rarely relevant since is not realistic assumes a totally independent parameter or an infinite precision on the determination of the other. To obtain the marginal error on a parameter, taking into account all the correlation, we have to compute the inverse of the Hessian matrix, so we have:

$$\sigma_i = \sqrt{H_{ii}^{-1}}. \tag{5.8}$$

To estimate the error for a future experiment what is used is the expectation value of the Hessian matrix. This quantity is called *Fisher Matrix*:

$$F_{ij} = \langle H_{ij} \rangle = \langle \frac{\partial^2 \ln \mathcal{L}}{\partial \lambda_i \partial \lambda_j} \rangle. \tag{5.9}$$

There is an important lower limit to error bars derived from the so called *Cramer-Rao inequality*. It states that for any unbiased estimator the minimum uncertainty on the parameters is given by:

$$\sigma_\lambda = \frac{1}{\sqrt{F_{\lambda\lambda}}}, \tag{5.10}$$

and if other parameters are derived from the same data, we have the *marginal error*:

$$\sigma_\lambda = \sqrt{F_{\lambda\lambda}^{-1}}. \tag{5.11}$$

We are now finally in the condition to quantify our previous statement on the Maximum Likelihood estimator, namely that it is the "best" estimator. By best we mean that the errors bars obtained from a Maximum Likelihood procedure, using the procedure outlined just above, saturate the lower limit provided by the Cramer-Rao inequality. No estimator can thus obtain errors bar smaller than the Maximum Likelihood estimator. Hence its central role in parameter estimation theory. A common case is that in which the observables O^{obs} we measure come from a Gaussian distribution with mean $O(\lambda)$ and variance σ. We assume that our observations are unbiased and the mean of distribution corresponds to the real value. The Likelihood is

$$\mathcal{L} = \frac{1}{(2\pi\sigma^2)^{\frac{N}{2}}} \exp \sum_{i=1}^{N} - \frac{\left[O_i^{obs} - O_i(\lambda)\right]^2}{2\sigma_i^2} \equiv e^{\frac{\chi^2}{2}}, \tag{5.12}$$

in our case the observable will be the angular averaged bispectrum $B_{\ell_1\ell_2\ell_3}$ and the summation will be on all possible combination of indices. For a Gaussian Likelihood

minimizing the χ^2 is equivalent to maximize the Likelihood. Let us study the curvature of χ^2 about its minimum. We have

$$\chi^2(\lambda) = \chi^2(\hat{\lambda}) + \frac{1}{2}\left.\frac{\partial^2\chi^2}{\partial\lambda^2}\right|_{\lambda=\hat{\lambda}}(\lambda-\hat{\lambda})^2. \tag{5.13}$$

The coefficient of the quadratic term is the curvature of the Likelihood. In this approximation, the Likelihood around the peak is Gaussian, hence we can compute the curvature from formula (5.13), so that we have:

$$\frac{1}{2}\left.\frac{\partial^2\chi^2}{\partial\lambda^2}\right|_{\lambda=\hat{\lambda}} = \mathcal{F} = \sum_i \frac{1}{\sigma_i}\left[\left(\frac{\partial O_i(\lambda)}{\partial\lambda}\right)^2 + \left(O_i(\lambda) - O^{obs}\right)\frac{\partial^2 O_i(\lambda)}{\partial\lambda^2}\right], \tag{5.14}$$

the second term in the summation can be ignored since we assume that our observations are unbiased: if this is true the difference will oscillate around zero resulting in cancellations. With this hypothesis, the curvature can be replaced by the Fisher matrix. Generalizing to many parameters we get:

$$F_{\alpha\beta} = \sum_i \frac{1}{\sigma_i^2}\frac{\partial O_i(\lambda)}{\partial\lambda_\alpha}\frac{\partial O_i(\lambda)}{\partial\lambda_\beta}. \tag{5.15}$$

This is a very powerful results, it states that the Fisher matrix can be computed with no data, so for a given fiducial choice of the parameters it is possible to estimate the expected error bars on a parameter before the experiment is performed.

5.2 Bispectrum Fisher Matrix

We want to define the uncertainty on the two parameters f_{NL} and n_{NG} of the bispectra defined by equations (4.9) and (4.14). The errors can be defined through equation (5.15) and (5.11), the observable O_i is the angular averaged bispectrum $B_{\ell_1\ell_2\ell_3}$. So we have [28]:

$$F_{\alpha\beta} = \sum_{\ell_1\le\ell_2\le\ell_3}\frac{1}{\sigma^2_{\ell_1\ell_2\ell_3}}\frac{\partial B_{\ell_1\ell_2\ell_3}}{\partial\lambda_\alpha}\frac{\partial B_{\ell_1\ell_2\ell_3}}{\partial\lambda_\beta}, \tag{5.16}$$

where the indices α,β take value 1 or 2 and correspond to our parameters $\lambda_1 = f_{NL}$ and $\lambda_2 = n_{NG}$. The summation isn't on all permutations due to the symmetry of the bispectrum with respect to permutations of ℓ's.
We have first to derive an expression for the variance of the three-point correlator [52][17]:

$$\sigma_{\ell_1\ell_2\ell_3} = \langle B^2_{\ell_1\ell_2\ell_3}\rangle - \langle B_{\ell_1\ell_2\ell_3}\rangle^2, \tag{5.17}$$

the second term is of order 2 in the non-Gaussian part that is known to be small, so it can be neglected, the first term is

$$\langle B^2_{\ell_1\ell_2\ell_3}\rangle = \sum_{m_1m_2m_3m_1'm_2'm_3'}\begin{pmatrix}\ell_1 & \ell_2 & \ell_3\\ m_1 & m_2 & m_3\end{pmatrix}\begin{pmatrix}\ell_1 & \ell_2 & \ell_3\\ m_1' & m_2' & m_3'\end{pmatrix}B^{m_1m_2m_3}_{\ell_1\ell_2\ell_3}B^{m_1'm_2'm_3'}_{\ell_1\ell_2\ell_3}, \tag{5.18}$$

where we used the definition (3.5) for the angular averaged bispectrum. The product of two bispectra is the six-point correlator, that we expand with the Wick theorem [23][31]:

$$\langle a_{\ell_1 m_1} a_{\ell_2 m_2} a_{\ell_3 m_3} a^*_{\ell_1 m_1'} a^*_{\ell_2 m_2'} a^*_{\ell_3 m_3'} \rangle = \langle a_{\ell_1 m_1} a^*_{\ell_1 m_1'} \rangle \langle a_{\ell_2 m_2} a^*_{\ell_2 m_2'} \rangle \langle a_{\ell_3 m_3} a^*_{\ell_3 m_3'} \rangle + 14\,\text{perm.}. \tag{5.19}$$

For the full expression see the appendix (C.1). Using the definition of the power spectrum and the relation

$$a_{\ell m} = a^*_{\ell -m} (-1)^m, \tag{5.20}$$

we can rearrange this expression as

$$\begin{aligned}\sigma^2_{\ell_1 \ell_2 \ell_3} = \sum_{m_1 m_2 m_3 m_1' m_2' m_3'} & \begin{pmatrix} \ell_1 & \ell_2 & \ell_3 \\ m_1 & m_2 & m_3 \end{pmatrix} \begin{pmatrix} \ell_1 & \ell_2 & \ell_3 \\ m_1' & m_2' & m_3' \end{pmatrix} C_{\ell_1} C_{\ell_2} C_{\ell_3} \Big\{ \delta^{m_1'}_{m_1} \delta^{m_2'}_{m_2} \delta^{m_3'}_{m_3} + \\ & + \Big[\delta^{\ell_2}_{\ell_1} \delta^{m_3'}_{m_3} \big(\delta^{m_1' m_2'}_{m_1 m_2} + \delta^{-m_2}_{m_1} \delta^{-m_2'}_{m_1'} \big) + 2\,\text{perm.} \Big] + \delta_{\ell_1 \ell_2 \ell_3} \Big[\big(\delta^{m_1' m_2' m_3'}_{m_1 m_2 m_3} + \delta^{m_3' m_1' m_2'}_{m_1 m_2 m_3} + \\ & + \big(\delta^{m_3' m_1' - m_2}_{m_1 - m_2' m_3} + 5\,\text{perm.} \big) \Big] \Big\}. \end{aligned} \tag{5.21}$$

This relation strongly simplifies when we account for the action of the Kronecker delta's in parenthesis. If all the ℓ are different clearly only one term survives, the summation on m normalizes to 1 so the variance is simply the product of the three power spectra. In the case of two equal indices, we have also one of the permutations in the first square brackets, but only the term without negative index remains, hence in total two terms are considered. This follows from the orthogonality relation of the Wigner symbols (B.15) and from the triangle conditions $m_i + m_j + m_k = 0$, that implies $m_k = 0$ if $m_i = -m_j$. The remaining case to consider is $\ell_1 = \ell_2 = \ell_3$. Even in this situation, the Wigner symbols preclude terms with negative m index so we count 6 terms: the first, three from the first square bracket and two from the second one. There is also a combination in which all the terms survive: is the one in which all ℓ are equal and all m are 0. However in the summation of all possible combinations the contribution of this single one is completely negligible. In conclusion we can express the variance of the bispectrum as:

$$\sigma^2_{\ell_1 \ell_2 \ell_3} = \Delta_{\ell_1 \ell_2 \ell_3} C_{\ell_1} C_{\ell_2} C_{\ell_3} \quad \begin{cases} \Delta_{\ell_1 \ell_2 \ell_3} = 1 & \ell_1 \neq \ell_2 \neq \ell_3 \\ \Delta_{\ell_1 \ell_2 \ell_3} = 2 & \ell_i = \ell_j \neq \ell_k \\ \Delta_{\ell_1 \ell_2 \ell_3} = 6 & \ell_1 = \ell_2 = \ell_3 \end{cases} \tag{5.22}$$

Using the definition (3.6) we can express the Fisher matrix as a function of the separable reduced bispectrum:

$$F_{\alpha\beta} \equiv \sum_{2 \leq \ell_1 \leq \ell_2 \leq \ell_3} \frac{(2\ell_1 + 1)(2\ell_2 + 1)(2\ell_3 + 1)}{4\pi} \begin{pmatrix} \ell_1 & \ell_2 & \ell_3 \\ 0 & 0 & 0 \end{pmatrix}^2 \frac{1}{\sigma^2_{\ell_1 \ell_2 \ell_3}} \frac{\partial b_{\ell_1 \ell_2 \ell_3}}{\partial \lambda_\alpha} \frac{\partial b_{\ell_1 \ell_2 \ell_3}}{\partial \lambda_\beta}. \tag{5.23}$$

For realistic forecast, we should include experimental features such as the beam W_ℓ, the experimental noise N_ℓ and the sky coverage f_{sky} .
The beam describes the smearing of the image due to the finite resolution of the experiment (determined by *e.g.* antenna resolution, optical diffraction, and so on)9 In most cases it can be reasonably modeled as a Gaussian *window function* convolving the actual signal ("circular Gaussian beam"). In harmonic space, this becomes a multiplication of the $a_{\ell m}$ multipoles with a function $W_\ell \propto \exp\left(-\ell(\ell+1)/2\sigma^2\right)$. The smaller is σ, the narrower is the beam and the higher is the *resolution* of the experiment; this implies a larger accessible ℓ_{max} or, equivalently, smaller scales being resolved in real space.
Experimental noise describes the spurious contributions to the measurement coming from interaction with the environment and from instrumental effects (e.g. thermal fluctuations in the detectors, and so on). For our purposes it can be assumed to be Gaussian distributed, "withe" and "stationary" (some power at all frequencies and scales; noise in different spatial direction and in different time is uncorrelated). In this case its power spectrum becomes simply a constant. The amplitude of the noise spectrum defines the noise level. The lower is the noise, the higher is the *sensitivity* of the experiment.
Moreover, even experiments covering the full sky will not be able to use data from every direction. Astrophysical emission can become much larger than the CMB signal in certain regions of the sky (e.g. in the galactic plane, or in the direction of bright point sources, such as quasars) thus requiring to *mask* those region, with consequent loss of information and increase in parameter uncertainties. All these effect can be accounted for in the Fisher matrix by means of the following substitutions:

$$B_{\ell_1\ell_2\ell_3} \to B_{\ell_1\ell_2\ell_3} W_{\ell_1} W_{\ell_2} W_{\ell_3}, \tag{5.24}$$

$$C_\ell \to C_\ell W_\ell + N_\ell, \tag{5.25}$$

$$F_{\alpha\beta} \to f_{sky} F_{\alpha\beta}, \tag{5.26}$$

where f_{sky} is the observed fraction of the sky after masking, N_ℓ is the noise power spectrum, and W_ℓ is the beam window function. The experimental noise does not affect the bispectrum: since it is generally considered Gaussian its three point function vanishes. For $f_{sky} \neq 1$ can be found that, with good approximation, the error bars scale as $\sqrt{f_{sky}}$ [29]. This is accounted for by the f_{sky} factor in (5.26) so our results for full sky coverage can be readily rescaled to forecast errors in presence of partial sky coverage.
The power spectrum of experimental noise that appears in the denominator dominates for a certain $\ell_{S=N}$ suppressing the signal contribution for higher ℓ. On the other hand until we remain in the range of ℓ in which the noise is very low the greatest contribution to the error budget comes from cosmic variance, so we can consider the experiment to be cosmic variance dominated and neglect the experimental noise. This range is roughly $\ell_{max} \leq 500$ for WMAP $\ell_{max} \leq 2000$ for *Planck* [29], under this limits it is reasonable not to take into account N_ℓ in the Fisher matrix. In absence of experimental noise the beams cancel out, so given these remarks we can safely use (5.23) in our computation.
From the solution of (5.23) we compute the *signal-to-noise ratio* $(S/N)_\alpha$, the *correlation*

coefficient $r_{\alpha\beta}$ between the two parameters and a *degradation parameter* d_α [28]:

$$\left(\frac{S}{N}\right)_\alpha \equiv \frac{1}{\sqrt{F^{-1}_{\alpha\alpha}}}, \tag{5.27}$$

$$r_{\alpha\beta} \equiv \frac{F^{-1}_{\alpha\beta}}{\sqrt{F^{-1}_{\alpha\alpha}F^{-1}_{\beta\beta}}}, \tag{5.28}$$

$$d_\alpha \equiv F_{\alpha\alpha}F^{-1}_{\alpha\alpha}, \tag{5.29}$$

d_α describes the degradation in the signal to noise ratio due to the correlation between the two parameters.

The scaling of the signal-to-noise ratio was deduced in flat-sky Sachs-Wolfe approximation by Babich and Zaldarriaga [4]. In flat-sky approximation we assume the sky to be flat (this is a good approximation for experiments covering small regions of the sky), so we can define spectra and bispectra by mean of the classical Fourier transform instead of harmonic expansion. The flat sky bispectrum is:

$$\langle a(\mathbf{l}_1)a(\mathbf{l}_2)a(\mathbf{l}_3)\rangle = (2\pi)^2\delta^2(\mathbf{l}_1+\mathbf{l}_2+\mathbf{l}_3))B(\mathbf{l}_1,\mathbf{l}_2,\mathbf{l}_3), \tag{5.30}$$

this corresponds at (3.3) with:

$$\begin{aligned}\mathcal{G}^{m_1m_2m_3}_{\ell_1\ell_2\ell_3} &\to \delta^2(\mathbf{l}_1+\mathbf{l}_2+\mathbf{l}_3)),\\ b_{\ell_1\ell_2\ell_3} &\equiv B(\mathbf{l}_1,\mathbf{l}_2,\mathbf{l}_3).\end{aligned} \tag{5.31}$$

The signal-to-noise is defined as:

$$\left(\frac{S}{N}\right)^2 \propto \int \mathrm{d}\mathbf{l}_1^2\mathrm{d}\mathbf{l}_2^2\mathrm{d}\mathbf{l}_3^2\,\delta^2(\mathbf{l}_1+\mathbf{l}_2+\mathbf{l}_3)\frac{B^2(\mathbf{l}_1,\mathbf{l}_2,\mathbf{l}_3)}{6C(\mathbf{l}_1)C(\mathbf{l}_2)C(\mathbf{l}_3)}. \tag{5.32}$$

In the Sachs-Wolfe regime using the definition (4.18) the scaling of the signal-to-noise can be computed as:

$$\left(\frac{S}{N}\right)^2 \propto \int \mathrm{d}\mathbf{l}_1^2\mathrm{d}\mathbf{l}_2^2\mathrm{d}\mathbf{l}_3^2\,\delta^2(\mathbf{l}_1+\mathbf{l}_2+\mathbf{l}_3)\mathbf{l}_1^2\mathbf{l}_2^2\mathbf{l}_3^2\left(\frac{1}{\mathbf{l}_1^2\mathbf{l}_2^2}+\frac{1}{\mathbf{l}_1^2\mathbf{l}_3^2}+\frac{1}{\mathbf{l}_2^2\mathbf{l}_3^2}\right), \tag{5.33}$$

and the solution of the integral gives:

$$\frac{S}{N} = \mathbf{l}_{max}\ln\frac{\mathbf{l}_{max}}{\mathbf{l}_{min}}, \tag{5.34}$$

where the ln derives from the strong coupling between large and small scales from the local shape.

An approximation for general bispectra peaking in the equilateral limit was found by Komatsu and Spergel [28] starting from (5.23). The number of mode contributing increases as $\ell^{3/2}$, $\ell^3\begin{pmatrix}\ell & \ell & \ell\\ 0 & 0 & 0\end{pmatrix}^2 \propto \ell$ and $\ell^2 C_\ell \sim$ constant so:

$$\begin{aligned}\left(\frac{S}{N}\right)_\alpha \sim \sqrt{F_{\alpha\alpha}} &\sim \ell^{3/2}\times\ell^{3/2}\left|\begin{pmatrix}\ell & \ell & \ell\\ 0 & 0 & 0\end{pmatrix}\right|\times\frac{\partial b_{\ell\ell\ell}}{\partial\lambda_\alpha}\frac{1}{C_\ell^{3/2}}\\ &\sim \ell^{3/2}\times\ell^{1/2}\times\frac{\partial b_{\ell\ell\ell}}{\partial\lambda_\alpha}\frac{\ell^3}{(\ell^2C_\ell)^{3/2}} \sim \ell^5\frac{\partial b_{\ell\ell\ell}}{\partial\lambda_\alpha}.\end{aligned} \tag{5.35}$$

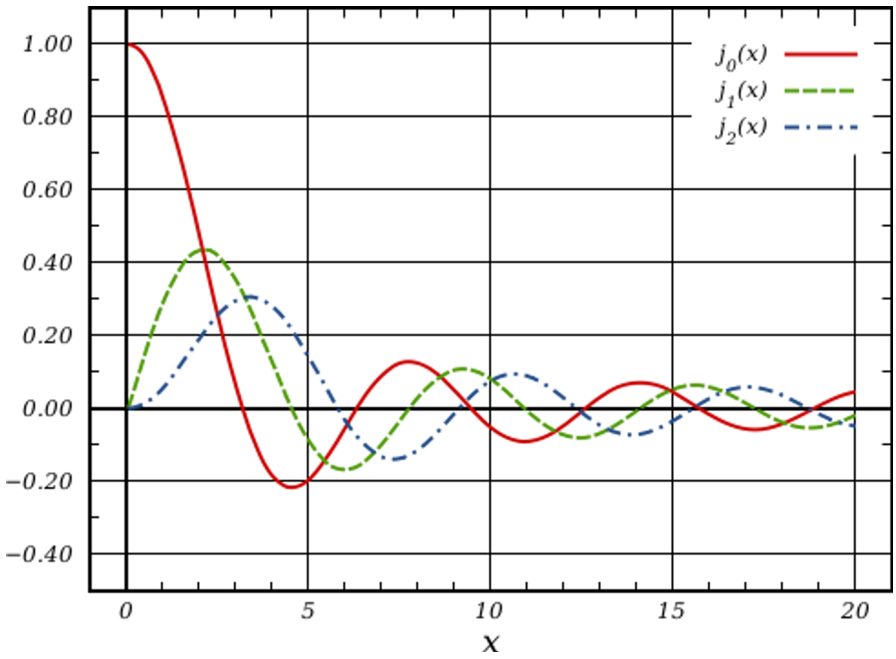

Figure 5.1: The first three spherical Bessel function

The scaling of the bispectrum is ℓ^{-4} as we see from (4.18) so, with some dimensional consideration can be found that:

$$\left(\frac{S}{N}\right)_{\alpha} \sim \ell \times 10^{-4} f_{NL} \tag{5.36}$$

5.3 Computational Implementation

Our numerical implementation comprises three stages: we first compute the coefficients, then we use them to evaluate reduced bispectra for which we perform the Fisher matrix analysis. All algorithms are developed in FORTRAN 95. All these numerical evaluations consist in the solution of definite integrals or, for the Fisher matrix, summations over bispectrum configurations.
In the first step we construct an algorithm to evaluate the coefficients defined by formulae (4.20) to (4.27). We compute every coefficient in a grid of values in coordinates r (conformal distance), t (Schwinger parameter) and ℓ that we will use also for the following computation.
These coefficients are defined by integrals over dk whose integrand functions present an highly oscillatory behavior due to the action of the spherical Bessel functions, as can be see in figure 5.1. The best way to solve these integrals numerically is to use the rectangle method[3] with a very fine quadrature. We use the partition provided from the standard package CAMB, which is the actual standard algorithm for the computation of CMB anisotropies, used both for WMAP and *Planck* data analysis. The CAMB code allows

[3]the rectangle method computes an approximation to a definite integral, made by finding the area of a collection of rectangles whose heights are determined by the values of the function.

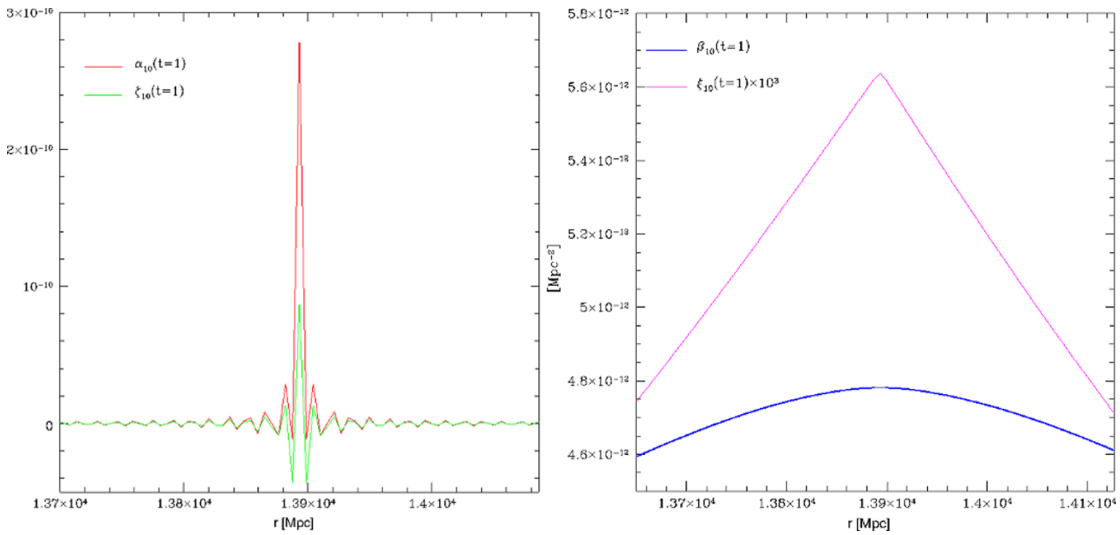

Figure 5.2: α_{10}, ζ_{10} (left) and β_{10}, ξ_{10} (right) coefficients as a function of the lookback conformal time r

to define the accuracy and the number of quadrature nodes in the computation of the transfer function. In order to improve the accuracy of bispectra evaluation we have to improve the level of accuracy with respect to standard C_ℓ computation, this approach is widely used in the literature.[4]. As a result the transfer functions are sampled in 33653 points in the interval $[2.35 \times 10^{-6}, 0.70551608]$ Mpc^{-1}. As a comparison we note that for standard C_ℓ evaluation ~ 3000 points are needed.
The spherical Bessel functions $j_\ell(kr)$ are computed with the subroutine "bjl.f90" from CMBfast[5]. This code use asymptotic approximations from [57] and [2]. The code compute different asymptotic expansions for $j_\ell(kr)$ in the cases $kr << \ell$ and $kr \simeq \ell$, the accuracy varies from $\sim 0.1\%$, at the boundaries between the asymptotic regions, to $\sim 10^{-5}\%$ well away from the boundaries.
To evaluate bispectra we have to compute a double integral over the lookback conformal time $r = c\tau$ and the Schwinger parameter t. As we stated in previous section, in order to optimize the computational time, we adopt the Sachs-Wolfe approximations assuming an Harrison-Zel'dovich power spectrum with tilt $n_s = 1$, however our algorithms can be straightforwardly generalized to include the full transfer function. Working in Sachs-Wolfe regime allows us to integrate over a narrow r interval around the recombination value $r_* = 13893.25$ Mpc. Then we take an equally spaced quadrature in the interval $[14168.385, 13618.115]$ Mpc from which most of the contribution comes, as it can be seen

[4] we set the parameter boost accuracy in the CAMB code to 3

[5] CMBFast was the first efficient computer code able to numerically evaluate the power spectrum of CMB anisotropies, it was based on integration over source along the photon past light cone [46]

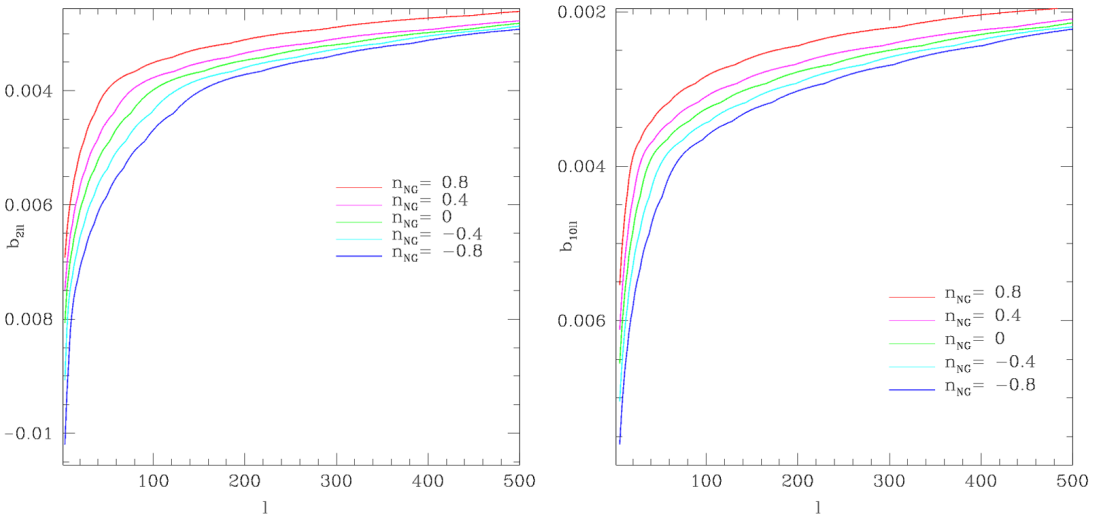

Figure 5.3: Two example of scale-dependent local bispectrum configuration for different values of the running parameter n_{NG}.. We fix $\ell_1 = 2, 10$ (left,right) and $\ell_2 = \ell_3 = \ell$ and plot the reduced bispectrum as a function of ℓ.

in figure (5.2). For the t integral we apply the Trapezoidal rule[6] on an uniform partition in $\log(t)$ with ten points for decades from 10^{-2} to 10^3. Some resulting bispectrum configurations are shown in figure 5.3.
Our Fisher matrix is defined by equation (5.23) with $\lambda_\alpha = f_{NL}$ and $\lambda_\beta = n_{NG}$. We have to define the derivative of the reduced bispectrum with respect to f_{NL} and n_{NG}, these are:

$$\frac{\partial b^{loc}_{\ell_1\ell_2\ell_3}}{\partial f_{NL}} = \frac{1}{\mathbf{k}_{piv}^{n_{NG}}\Gamma(1-n_{NG})}\int_0^\infty \mathrm{d}t\, t^{-n_{NG}} \int_0^\infty \mathrm{d}r\, r^2 \Big[\Big(\alpha_{\ell_1}\beta_{\ell_2}\xi_{\ell_3} + 5\,\text{perm.}\Big) + \\ + \Big(\beta_{\ell_1}\beta_{\ell_2}\zeta_{\ell_3} + 2\,\text{perm.}\Big)\Big], \tag{5.38}$$

$$\frac{\partial b^{loc}_{\ell_1\ell_2\ell_3}}{\partial n_{NG}} = \frac{f_{NL}}{\mathbf{k}_{piv}^{n_{NG}}}\frac{1}{\Gamma(1-n_{NG})}\int_0^\infty \mathrm{d}t\, t^{-n_{NG}}\,(-\psi_0(1-n_{NG}) - \ln \mathbf{k}_{piv} - \ln t)\times \\ \times \int_0^\infty \mathrm{d}r\, r^2 \Big[\Big(\alpha_{\ell_1}\beta_{\ell_2}\xi_{\ell_3} + 5\,\text{perm.}\Big) + \Big(\beta_{\ell_1}\beta_{\ell_2}\zeta_{\ell_3} + 2\,\text{perm.}\Big)\Big], \tag{5.39}$$

here $\psi_0(1-n_{NG})$ is the *digamma function*,it is defined as the logarithmic derivative of the gamma function.
In the Fisher matrix evaluation we will consider some fiducial value for f_{NL} and n_{NG}, in order to constrain a scale-dependence the amplitude parameter must be large enough

[6]The trapezoidal rule works by approximating the region under the graph of the function f(x) as a trapezoid and calculating its area. It follows that for every interval $[x_a, x_b]$ in the partition we have:

$$\int_{x_a}^{x_b} f(x)\,dx \approx (x_b - x_a)\left[\frac{f(x_a)+f(x_b)}{2}\right]. \tag{5.37}$$

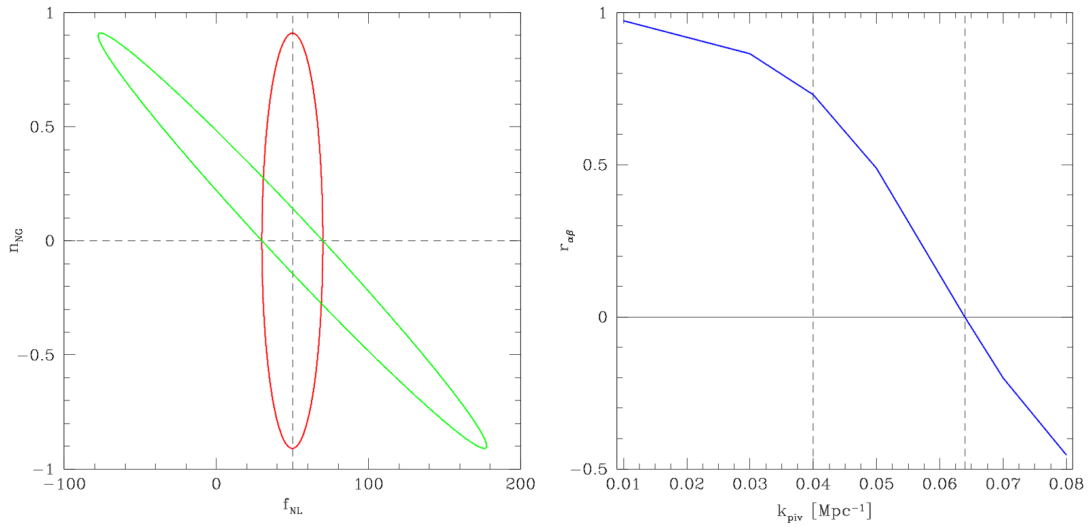

Figure 5.4: Left: Confrontation between different choice of the pivot point. The red ellipse refer to the $1-\sigma$ constraints on f_{NL} and n_{NG} assuming $k_{piv} = 0.064$ and fiducial values $f_{NL} = 50$, $n_{NG} = 0$. The green ellipse refer to $k_{piv} = 0.040$ with the same fiducial values, the correlation coefficient take values respectively $r_{\alpha\beta} = 0.001$, $r_{\alpha\beta} = 0.989$. Right: Correlation coefficient between the two parameters as a function of the pivot point. We consider $\ell_{max} = 500$, this is the range over which WMAP can be considered cosmic-variance dominated.

to be detected. Obviously we are not able to measure any of its features if it is too small (the lowest theoretical limit for an ideal experiment is $f_{NL} = 2$ [43]). As fiducial value we take $f_{NL} = 50$ and $n_{NG} = 0$, inserting these values in equation (5.38) and (5.39) we obtain:

$$\frac{\partial b^{loc}_{\ell_1\ell_2\ell_3}}{\partial f_{NL}} = \int_0^\infty \mathrm{d}t \int_0^\infty \mathrm{d}r\, r^2 \Big[\Big(\alpha_{\ell_1}\beta_{\ell_2}\xi_{\ell_3} + 5\,\text{perm.}\Big) + \Big(\beta_{\ell_1}\beta_{\ell_2}\zeta_{\ell_3} + 2\,\text{perm.}\Big)\Big], \quad (5.40)$$

$$\begin{aligned}\frac{\partial b^{loc}_{\ell_1\ell_2\ell_3}}{\partial n_{NG}} =& 50 \int_0^\infty \mathrm{d}t\ (-\gamma - \ln \mathbf{k}_{piv} - \ln t) \int_0^\infty \mathrm{d}r\, r^2 \Big[\Big(\alpha_{\ell_1}\beta_{\ell_2}\xi_{\ell_3} + 5\,\text{perm.}\Big) + \\ &+ \Big(\beta_{\ell_1}\beta_{\ell_2}\zeta_{\ell_3} + 2\,\text{perm.}\Big)\Big], \end{aligned} \quad (5.41)$$

where γ is the *Euler-Mascheroni constant,i.e.* $\psi_0(1) = \gamma \simeq 0.5772156649015328$, for further information about the gamma function and its derivatives see appendix B.3 or chapter 6 of [1].
To compute the Wigner symbol in equation (5.23) we use the analytical expression (B.19) for low ℓ, while, for high ℓ, we use the approximation (B.21) in order to avoid the problems arising from the numerical evaluation of the factorial in equation (B.19). This approach provides errors of the order of percent at the lowest ℓ, and decreasing as ℓ increases, for further details see [56] and [18].
In the next sections we will show the results of this analysis.

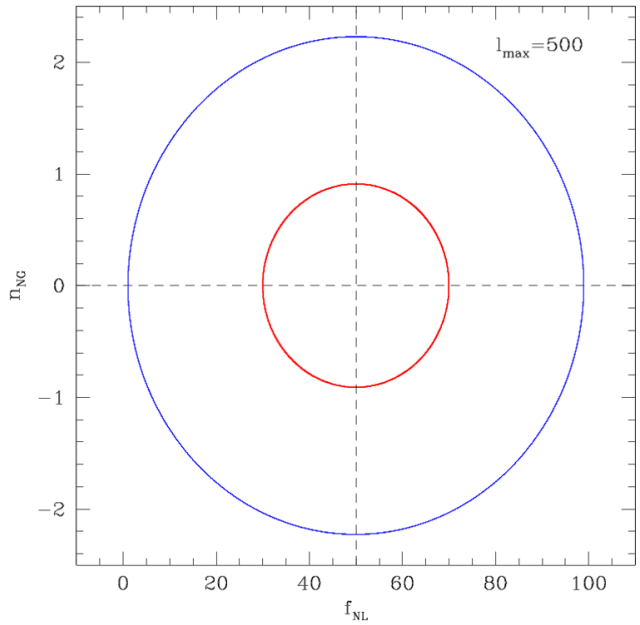

Figure 5.5: 68% (*red*) and 95% (*blue*)confidence region on local model parameters f_{NL} and n_{NG} for $\ell_{max} = 500$ (WMAP cosmic-variance dominated range), assuming $\mathbf{k}_{piv} = 0.064$.

5.4 Results

Thanks to formula (4.4), and to the algorithm just discussed, we are now able to compute scale-dependent bispectra for any separable shape. Unlike existing parametrizations, our form is analytically exact, allowing to perform a complete analysis of the scale dependence of a separable bispectrum. We show in this section the results of our computation for the local case in Sachs-Wolfe approximation in the range of sensitivity of WMAP. We make this choice in order to increase computational efficiency, since we run the code on a single CPU. This allows us to test our numerical tools in a controlled framework. As a comparison we refer to the article [43] in which the authors developed a similar computation using a simpler approximation for the amplitude's scale dependence.
As an example, we perform the same analysis in a wider range of sensitivity ($\ell_{max} = 3100$), but integrating over a smaller r interval $[13949.4, 13837.1]$. This made the computation feasible, but the precision of this computation is lower. We show the results in the end of this section.
In figure 5.3 are shown several configurations of local bispectra for different value of the running parameter n_{NG}. Note the absence of acoustic peaks, due to the fact that we are working in Sachs-Wolfe approximation.
Our work consists in a Fisher matrix analysis of the CMB bispectrum to forecasts error bars on the amplitude parameter f_{NL} and of a running parameter n_{NG}. As a preliminary test we consider the local model, expressed in equation (4.9), in a range of ℓ compatible with the WMAP sensitivity. We assume a fiducial value for $f_{NL} = 50$ and for $n_{NG} = 0$, and as pivot point we choose $\mathbf{k}_{piv} = 0.064$.

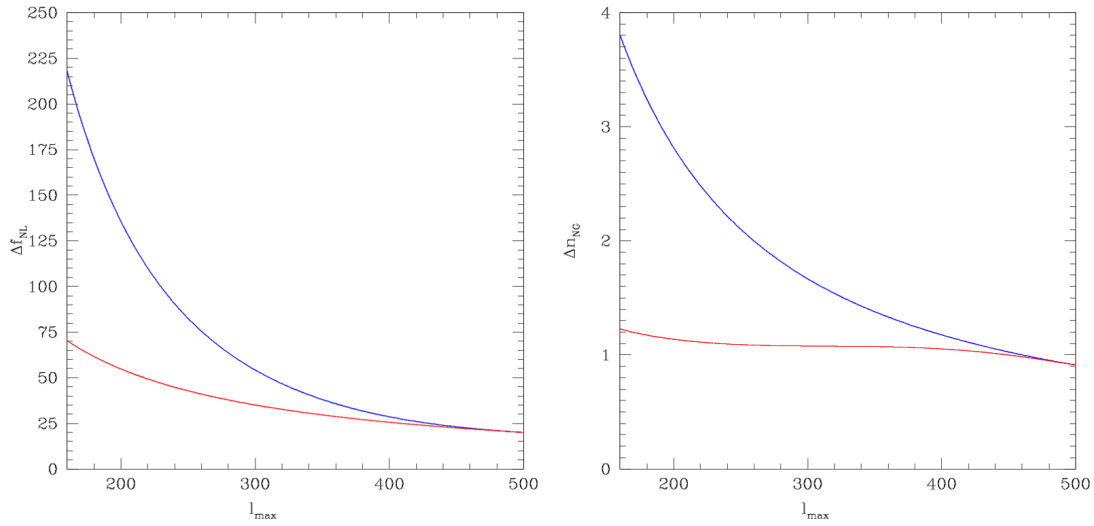

Figure 5.6: Expected marginalized (*blue lines*) and unmarginalized (*red lines*) $1-\sigma$ errors for f_{NL} (left panel) and n_{NG} (right panel) as function of ℓ_{max}.

Note that $f_{NL} = 50$ is nowadays a totally unrealistic value, the most recent estimate provided by *Planck* constrain the value of this parameter to $f_{NL} = 2.7 \pm 5.8$ for the local model. However we use this value because we are working at WMAP resolution. It is also consistent with WMAP less stringent constraints $f_{NL} < 100$.
We are essentially free to choose the pivot point as we like. It is thus logical and convenient to select a value that minimize the correlation between the two parameters.
We show in figure 5.4 (left panel) how this parameter influences the marginalized error: the two ellipses (red and green) refers respectively to $\mathbf{k}_{piv} = 0,064$ and $\mathbf{k}_{piv} = 0,040$. In the first case the correlation parameter (defined in equation (5.28)) takes value $r_{\alpha\beta} = -0.001$, this indicates a very low correlation between the two parameters, as can be deduced from the fact that the resulting ellipse (the red one) is almost aligned with the coordinates axes. In the second case, the value of the correlation parameter is $r_{\alpha\beta} = -0.989$, the inclination of the resulting ellipse is almost $45°$ with respect to the coordinates axes, its clear that in this case the addition of n_{NG} in the analysis dramatically increases the uncertainty on f_{NL}. This bad choice of parameters would make the interpretation of the result, and the comparison with the standard scale independent case harder.
The scaling of the correlation parameter with respect to the pivot point is shown in 5.4 (right panel). Removing the correlation between the two parameters allow us to perform our analysis on the running parameter without affect the measurement of f_{NL}. Thanks to this, we can say that the constraint on the extra running parameter come with *no cost* with respect to the constraints on the amplitude.
However, the pivot point depends on the particular shape considered, on the multipoles range, and on the characteristic signal-to-noise over the range of scales proved. So, analyzing different model, as the equilateral model or the orthogonal one, implies the definition of a different pivot scale, as well as considering a particular experiment (as *e.g. Planck* or WMAP).

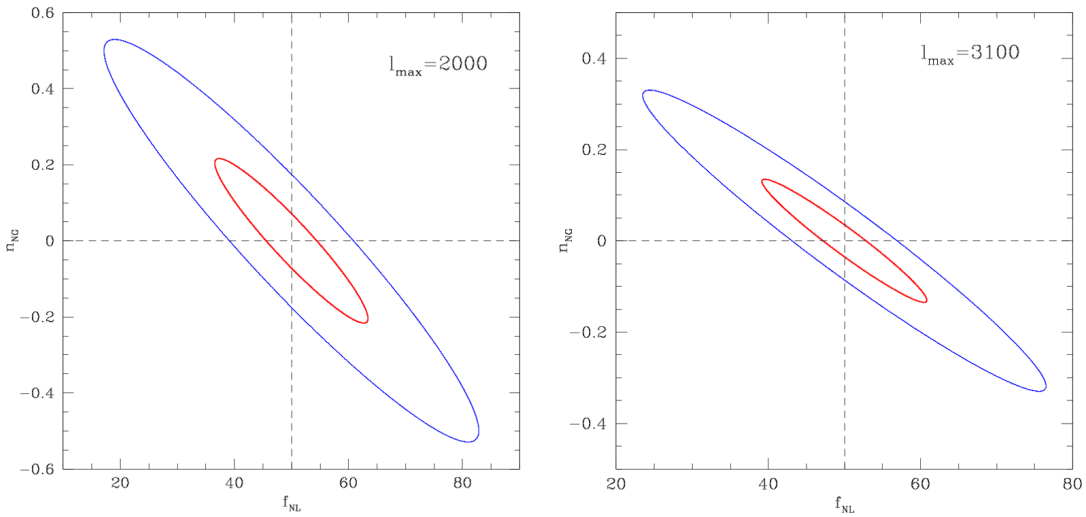

Figure 5.7: 68% (*red*) and 95% (*blue*)confidence region on local model parameters f_{NL} and n_{NG} for $\ell_{max} = 2000$ (left), corresponding to the *Planck* cosmic-variance dominated range, and for an ideal experiment with $\ell_{max} = 3100$. In both case we set $\mathbf{k}_{piv} = 0.07$.

In figure 5.5 we show the expected 68% (red ellipse) and 95% (blue ellipse) confidence region on local model parameters for the WMAP experiment. Note that the red ellipse is the same plotted in figure 5.4. The $1-\sigma$ uncertainties on the two parameters under consideration in this case are:

$$\Delta f_{NL} = 20.00, \tag{5.42}$$

$$\Delta n_{NG} = 0.91. \tag{5.43}$$

This values are compatible with the constraints found in [43] for WMAP. This was not obvious, as in [43] a very simple approximation is used to factorize the scale dependent part of the shape. This cross-check provide a useful validation of some of the results in [43], and this is a first application of our newly derived exact scale-dependent bispectrum ansatz.

In figure 5.6 we plot the expected marginalized (*blue lines*) and unmarginalized *red lines* $1-\sigma$ errors on respectively on f_{NL} (left panel) and n_{NG} (right panel) as a function of ℓ_{max}. This demonstrates how the correlation between the two parameters strictly depends on the multipole range of the experiment. In fact, for low ℓ_{max}, the marginalized and unmarginalized error are very different, whereas they are almost coincident at $l_{max} = 500$. This derives from the fact that we choose the pivot scale in order to minimize the correlation at this resolution.

As we said, we extend our analysis to $\ell_{max} = 3100$. Note that, even if we use a very narrow r interval, the computational time needed to obtain this results was $\sim 35\,hr$.

In figure 5.7 we show the expected errors for *Planck* and for an ideal experiment reaching $\ell_{max} = 3100$. Also in this calculation we use as fiducial values $f_{NL} = 50$ and $n_{NG} = 0$, as pivot point we choose $k_{piv} = 0.07$.

To obtain constraints at *Planck* resolution we assume $\ell_{max} = 2000$, neglecting the experimental noise, because this is the range over which the the main contribution to the

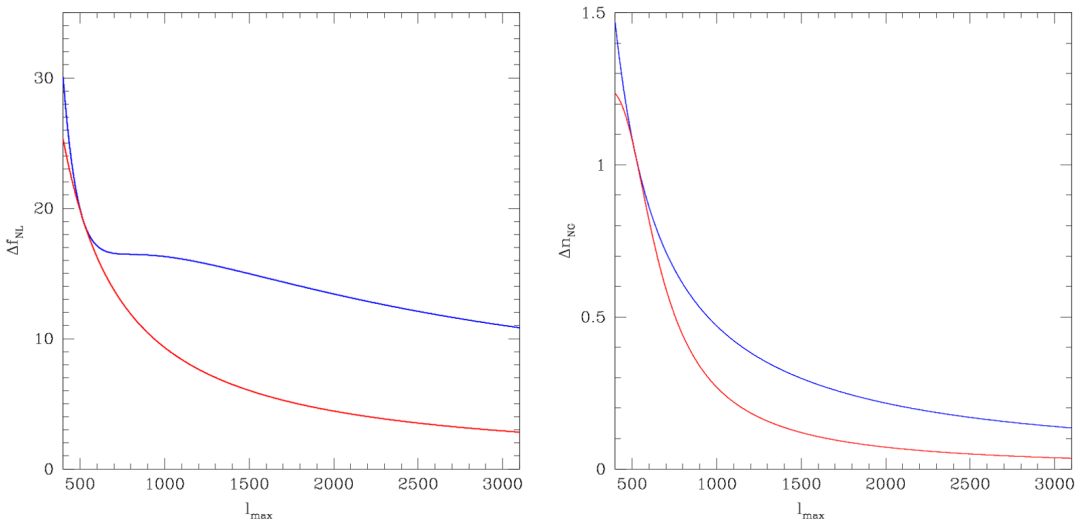

Figure 5.8: Expected marginalized (*blue lines*) and unmarginalized (*red lines*) $1-\sigma$ errors for f_{NL} (left panel) and n_{NG} (right panel) as function of ℓ_{max}.

noise comes from the cosmic-variance.
The uncertainties we obtained for *Planck* are:

$$\Delta f_{NL} = 13.49, \tag{5.44}$$
$$\Delta n_{NG} = 0.22. \tag{5.45}$$

And for the ideal experiment:

$$\Delta f_{NL} = 10.83, \tag{5.46}$$
$$\Delta n_{NG} = 0.13. \tag{5.47}$$

In figure 5.8 we show the scaling of the uncertainties on the two non Gaussian parameters f_{NL} and n_{NG}. Is evident how the marginalized error and the unmarginalized one coincide for $\ell_{max} \sim 500$ and diverge for higher values. As we stated above, this derives from the fact that the optimal pivot point, for which the correlation between the two parameter is minimal, strongly depends on the multipole range considered.
Before concluding this section we stress again that the results shown here rely on a number of simplifications, namely Sachs-Wolfe approximation, neglecting noise up to a given scale, and working at WMAP resolution.
Nonetheless, while allowing for strong reduction of computational time, these approximation are already good enough to fully characterize the scaling of signal-to-noise ratio, and for a first comparison with the previous results in the literature.
A full analysis at *Planck* resolution, including all the radiative transfer effects, is one of our goals for the near future. All the codes and the numerical machinery developed here can essentially be used without any change for this next step (except a trivial replacement of the Sachs-Wolfe transfer function with the full one). All that is needed for the full analysis is to improve the speed of the computation by porting the line to

a computer cluster, after its parallelization. We also stress again that the analytical precision of our method will be crucial in order to fully exploit the potential of accurate high-resolution CMB datasets such as *Planck*.

Chapter 6

Conclusions

The most promising theory to solve the outstanding questions related to initial conditions in the Standard Cosmological Model is the *Theory of Inflation*. However, present observations still have little power to discriminate between the huge number of different Inflationary scenarios proposed in the literature.
For this purpose, one of the main goals of contemporary Cosmology is to put constraints on the *non-Gaussianity* of the primordial cosmological perturbations field. Primordial non-Gaussianity is one of the most informative fingerprints of the origin of structure in the Universe, probing physics at extremely high energy scales inaccessible to laboratory experiments. The standard single-field *slow-roll* Inflationary model implies very small (but calculable) deviations from Gaussianity, however, a number of more complex models predict some degree of non-Gaussianity in the perturbations. Thus this measurement is one of the most valuable tools for the purpose of discriminating between the various Inflationary scenarios proposed in the literature.
Actual calculations in the Inflationary framework show that, in order to obtain information about the departure from Gaussianity of the primordial perturbation field, the ideal statistic is the tree-point function, or rather its Fourier counterpart, the primordial *Bispectrum* $B_\Phi(k_1, k_2, k_3)$.
Since the CMB temperature is linked to primordial perturbation by a linear operator describing radiative transfer effects in the primordial plasma, an eventual deviation from Gaussianity on the primordial cosmological perturbation field is directly reflected on the CMB temperature field. This makes the CMB angular Bispectrum $B_{\ell_1\ell_2\ell_3}$ a perfect observable to test primordial departure form Gaussianity.
Unfortunately, due to cosmic-variance, the signal-to-noise ratio of a single bispectrum configuration is too low to be detected. For this reason, bispectrum measurements focus on the determination of a single *amplitude parameter*, called f_{NL}, that can be obtained from the integration over all the allowed bispectrum configurations.
The primordial bispectrum is thus usually characterized by the dimensionless parameter f_{NL} and a *shape function* that defines from which kind of configurations the largest contribution to the signal comes. Different Inflationary Models generally generate bispectra peaked on different combinations of ℓ. In light of what we just said, it should be clear how the detection and characterization of the primordial bispectrum is a major issue of contemporary cosmology.

The greatest obstacle in the computation of bispectra is the high computational costs of this operation, a brute-force calculation would scale like $\mathcal{O}(\ell_{max}^5)$, resulting absolutely impossible for survey like *Planck* with $\ell_{max} \sim 2000$. For this reason, modern bispectrum calculations are based on *factorized forms* of the shape functions, this reduces the computational costs to $\mathcal{O}(\ell_{max}^3)$ making the computation viable.
Furthermore several Inflationary models suggest that the amplitude parameter f_{NL} could show a significant scale-dependence. Until now this aspect has received little attention in the literature, due to the high uncertainty on the determination of the amplitude parameter itself in the past surveys. However, thanks to the high angular resolution and sensitivity reached by modern surveys like *Planck*, it will be possible to put significant constraints on a possible scale dependence of f_{NL} [43]. The detection of a running of this parameter would provide completely new information about the Physics of the primordial Universe.
A first study was made by Sefusatti et al. in [43]. They developed a simple separable form and put preliminary constraints on the eventual scale dependence of the amplitude parameter. However, their parametrization is not adequate to precisely compute all the possible shapes of the bispectrum, and the high resolution of modern survey requires higher precision tools in order to correctly analyze the data.
In this thesis, starting from a scale-dependent primordial bispectrum ansatz, we develop an analytically exact scale-dependent parametrization for f_{NL} introducing a *running parameter* n_{NG}.
To do that, we appeal to the so called *Schwinger parametrization*, widely used in quantum field theory to evaluate loop integrals, and we perform the substitution:

$$f_{NL} \to f_{NL} \left(\frac{k_1 + k_2 + k_3}{\mathbf{k}_{piv}} \right)^{n_{NG}} = \frac{f_{NL}}{\mathbf{k}_{piv}^{n_{NG}}} \frac{1}{\Gamma(1 - n_{NG})} \int_0^\infty \mathrm{d}t \, t^{-n_{NG}} \left[k_1 e^{-t(k_1+k_2+k_3)} + 2 \,\mathrm{perm.} \right]. \tag{6.1}$$

in this form, the non-separable factor $(k_1 + k_2 + k_3)^{n_{NG}}$ becomes an integral over the so called *Schwinger parameter* t of a factorizable function. This parametrization is analytically exact and preserve the factorizability of the resulting bispectrum. We emphasize that, in order to compute the bispectrum, it is absolutely necessary to write it in separable form due to the high computational cost of non-separable forms.
With our parametrization it is now possible to write *every* scale-dependent bispectrum existing in the literature in separable form, without resorting to any approximation and allowing a complete analysis of the scale dependence of the non-Gaussian parameter. It will be possible to correctly take advantage of the high precision data sets provided by modern surveys, putting strict constraints on the running of the non Gaussian parameter.
We developed a complete set of numerical tools to compute separable scale-dependent bispectra and to forecast the expected uncertainties on the amplitude parameter f_{NL} and the running parameter n_{NG}. Our algorithms are developed to compute any kind of separable bispectrum in the literature taking into account the scale dependence of the running parameter. In our preliminary analysis we work in Sachs-Wolfe approximation to reduce the computational time, however our algorithms are readily suitable to undertake a complete analysis of the complete scenario including the full transfer function.
We performed a *Fisher matrix* analysis for the so called *local model*, obtaining constraints

for f_{NL} and n_{NG} in the range of sensitivity of WMAP. We find that our results are compatible with the existing literature: $\Delta f_{NL} \sim 20$ and $\Delta n_{NG} \sim 0,91$ at the WMAP scale [43]. Our computation shows that the addition of the running parameter doesn't affect the uncertainty on f_{NL}, since we can choose the optimal pivot point to remove any degeneracy between the two parameters.
Much work remains to be done: first of all we have to improve our analysis including the full transfer function and extending the computation to the sensitivity level of modern surveys. This does not require any conceptual generalization or rewriting of the currently existing pipeline and it will be possible having access to more computational power, and parallelizing the codes to allow them to work on multi-processor machine. Furthermore we have to include in our analysis also the other separable shapes existing in the literature, *e.g. equilateral model* and *orthogonal model*, to get a more complete picture of the predictions obtained from various Inflationary scenarios. Once we will develop a complete forecast for all the possible Inflationary models, the following step will be to extract both the amplitude parameter and the running parameter from the *Planck* data set.

Appendix A

Useful Formulae of General Relativity

In general relativity in the partial derivative operation we have to take into account the curvature of the space time. So the *covariant derivative* operator is introduced:

$$\nabla_\mu V^\mu = \partial_\mu V^\mu + \Gamma^\nu_{\mu\lambda} V^\lambda \tag{A.1}$$

where V^μ is a generic 4-vector and $\Gamma^\nu_{\mu\lambda}$ is the connections coefficients, also known as *Christoffel symbol*. The Christoffel symbol describe geodesic in non-trivial coordinates system.
A geodesic is the generalization in a curved space of a straight line.
The Christoffel symbol is defined from the metric as:

$$\Gamma^\mu_{\alpha\beta} = \frac{1}{2} g^{\mu\nu} \left[\partial_\alpha g_{\beta\nu} + \partial_\beta g_{\alpha\nu} - \partial_\nu g_{\alpha\beta} \right]. \tag{A.2}$$

The *geodesic equation*, expressing the Newton law with no forces in general relativity is :

$$\frac{\mathrm{d}^2 x^\mu}{\mathrm{d}\lambda^2} + \Gamma^\mu_{\alpha\beta} \frac{\mathrm{d}x^\alpha}{\mathrm{d}\lambda} \frac{\mathrm{d}x^\beta}{\mathrm{d}\lambda}. \tag{A.3}$$

In a curved space-time, the parallel transport of a vector V^σ on a closed loop defined by two infinitesimal vector A^μ and B^μ results in a modification δV^ρon the vector. This change is quantified by the curvature tensor also know as *Riemann tensor*, that is:

$$\delta V^\rho = R^\rho_{\sigma\mu\nu} A^\mu B^\nu V^\sigma. \tag{A.4}$$

The definition of the Riemann tensor is

$$R^\rho_{\sigma\mu\nu} = \partial_\mu \Gamma^\rho_{\nu\sigma} + \partial_\nu \Gamma^\rho_{\mu\sigma} + \Gamma^\rho_{\mu\lambda} \Gamma^\lambda_{\nu\sigma} + \Gamma^\rho_{\nu\lambda} \Gamma^\lambda_{\mu\sigma} \tag{A.5}$$

The contraction of the Riemann tensor give the *Ricci tensor* $R_\mu\nu$, its definition follow from A.5:

$$R^{\mu\nu} = \partial_\lambda \Gamma^\lambda_{\mu\nu} + \partial_\nu \Gamma^\lambda_{\mu\lambda} + \Gamma^\lambda_{\lambda\beta} \Gamma^\beta_{\mu\nu} + \Gamma^\lambda_{\beta\nu} \Gamma^\beta_{\mu\lambda}. \tag{A.6}$$

The track of the Ricci tensor define the Ricci scalar:

$$\begin{aligned} R =& g^{\mu\nu} R_{\mu\nu} \\ \nabla^{\mu} R_{\mu\nu} =& \frac{1}{2} \nabla_{\nu} R \end{aligned} \tag{A.7}$$

The Einstein equation is:

$$R_{\mu\nu} - \frac{1}{2} g_{\mu\nu} = G_{\mu\nu} = 8\pi G T_{\mu\nu} \tag{A.8}$$

were $G_{\mu\nu}$ is the *Einstein tensor*.

Appendix B

Special Functions

B.1 Spherical harmonics

Spherical harmonics are the angular portion of a set of solutions to Laplacian. Usually we refer to Laplace's spherical harmonics Y_ℓ^m that are a specific set of spherical harmonics forming an orthogonal system. They are eigenfunction of the equation

$$\left[\frac{1}{\sin\theta}\frac{\partial}{\partial\theta}\left(\sin\theta\frac{\partial}{\partial\theta}\right)+\frac{1}{\sin^2\theta}\frac{\partial^2}{\partial\phi^2}\right]Y_\ell^m(\theta,\phi)=-\ell(\ell+1)Y_\ell^m(\theta,\phi). \tag{B.1}$$

We used them to describe a distribution on a spherical surface with harmonics behavior; this is the analogue of the Fourier decomposition in flat space. The orthogonal relation states:

$$\int \mathrm{d}\Omega\,\overline{Y}_\ell^m\Omega Y_{\ell'}^{m'}(\Omega)=\delta_{\ell\ell'}\delta_{mm'}. \tag{B.2}$$

B.1.1 Legendre Polinomials

The Legendre polinomials are particular solutions of Legendre's equations the is useful to solve the Laplace's equation in spherical coordinates. For our aim is sufficient to know their orthogonality relation:

$$\int_{-1}^{1}\mathcal{P}_\ell(x)\mathcal{P}_{\ell'}(x)=\delta_{\ell\ell'}\frac{2}{2\ell+1}. \tag{B.3}$$

They can be expressed by a sum of products of spherical harmonics:

$$\mathcal{P}_\ell(\hat{x}\cdot\hat{x}')=\frac{4\pi}{2\ell+1}\sum_{m=-\ell}^{\ell}Y_\ell^m(\hat{x})\overline{Y}_\ell^m(\hat{x'}). \tag{B.4}$$

B.2 Spherical Bessel Functions

The spherical Bessel function $j_\ell(x)$ satisfy the differential equation:

$$\frac{\mathrm{d}^2 j_\ell(x)}{\mathrm{d}x^2}+\frac{2}{x}\frac{\mathrm{d}j_\ell(x)}{\mathrm{d}x}+\left[1-\frac{\ell(\ell-1)}{x^2}\right]j_\ell(x)=0. \tag{B.5}$$

They are crucial in the study of the CMB because, leading the radial evolution, they project the inhomogeneities at last scattering into the actual sky.
These function obey to the so called closure relation:

$$\int_0^\infty \mathrm{d}x\, x^2 j_\ell(ax) j_\ell(bx) = \frac{\pi}{2a^2}\delta_D(a-b) \tag{B.6}$$

They are related to Legendre polinomials by expressions:

$$\frac{1}{2}\int_{-1}^{1} \mathrm{d}\mu \mathcal{P}_\ell(\mu) e^{ix\mu} = \frac{j_\ell(x)}{(-i)^\ell} \tag{B.7}$$

The inversion of this equations gives a useful expansion fo Fourier basis functions:

$$e^{i\vec{k}\cdot\vec{x}} = \sum_{\ell=0}^{\infty} i^\ell (2\ell+1) j_\ell(kx) \mathcal{P}_\ell(\hat{k}\cdot\hat{x}). \tag{B.8}$$

Replacing formula (B.4) in this equation we obtain the spherical wave expansion of vector plane wave used in chapter 3 equation (3.17):

$$e^{i\vec{k}\cdot\vec{x}} = (4\pi)\sum_{\ell=0}^{\infty} i^\ell j_\ell(kr) \sum_{m=-\ell}^{\ell} Y_\ell^m(\hat{x})\overline{Y}_\ell^m(\hat{k}) \tag{B.9}$$

Another important relation allows to express the integral containing squared Bessel functions in terms of Euler Gamma functions:

$$\int_0^\infty \mathrm{d}x\, x^{n-2} j_\ell^2(x) = 2^{n-4}\pi \frac{\Gamma(\ell+\frac{n}{2}-\frac{1}{2})\Gamma(3-n)}{\Gamma(\ell+\frac{5}{2}-\frac{n}{2})\Gamma^2(2-\frac{n}{2})} \tag{B.10}$$

B.3 Gamma Functions

The Gamma function is an extension of the factorial function to real and complex number. That is, with n a real number:

$$\Gamma(n) = (n-1)! \tag{B.11}$$

More generally, for a generic complex number x:

$$\Gamma(x+1) = x\Gamma(x). \tag{B.12}$$

It is defined for all complex number except negative integers and zero. The derivative of the gamma function can be express in terms of the polygamma function:

$$\Gamma'(x) = \Gamma(x)\psi_0(x) \tag{B.13}$$

In particular, in our computation we used the value:

$$\Gamma'(1) = -\gamma \tag{B.14}$$

where γ is the Euler-Mascheroni constant, its value is: $\gamma = 0.5772156649015328...$.

B.4 Wigner 3-j symbols

The Wigner 3-j symbols are related to the Clebsh–Gordan coefficients which describe coupling of two angular momenta, they are defined as a 2×3 matrix

$$\begin{pmatrix} \ell_1 & \ell_2 & \ell_3 \\ m_1 & m_2 & m_3 \end{pmatrix}$$

more specifically a symbol of this kind describes three angular momenta forming a triangle, for this reason they satisfies the triangle conditions $L_1 + L_2 + L_3 = 0$, from this derives:

$$\begin{aligned} &|\ell_i - \ell_j| \leq \ell_k \leq \ell_i + \ell_j \\ &m_1 + m_2 + m_3 = 0 \\ &\ell_1 + \ell_2 + \ell_3 = even. \end{aligned}$$

The special case with $\ell_1 = \ell_2$ and $m_3 = 0$ is useful in the calculation of the variance of the bispectrum:

$$\begin{pmatrix} \ell & \ell & \ell' \\ m & -m & 0 \end{pmatrix} = \frac{(-1)^\ell}{\sqrt{2\ell + 1}} \delta_{\ell' 0} \tag{B.15}$$

Other important proprieties are the orthogonality relations we used in the calculation of angle average bispectrum

$$\sum_{\ell_3 m_3} (2\ell_3 + 1) \begin{pmatrix} \ell_1 & \ell_2 & \ell_3 \\ m_1 & m_2 & m_3 \end{pmatrix} \begin{pmatrix} \ell_1 & \ell_2 & \ell_3 \\ m_1' & m_2' & m_3 \end{pmatrix} = \delta_{m_1 m_1'} \delta_{m_2 m_2'} \tag{B.16}$$

$$\sum_{m_1 m_2} \begin{pmatrix} \ell_1 & \ell_2 & \ell_3 \\ m_1 & m_2 & m_3 \end{pmatrix} \begin{pmatrix} \ell_1 & \ell_2 & \ell_3' \\ m_1 & m_2 & m_3' \end{pmatrix} = \delta_{m_1 m_1'} \delta_{m_2 m_2'} \tag{B.17}$$

$$\sum m_1 m_2 m_3 \begin{pmatrix} \ell_1 & \ell_2 & \ell_3 \\ m_1 & m_2 & m_3 \end{pmatrix}^2 = 1. \tag{B.18}$$

An analytical expression for the symbol $\begin{pmatrix} \ell_1 & \ell_2 & \ell_3 \\ 0 & 0 & 0 \end{pmatrix}$ [56], that we used in the computations of Fisher matrix is:

$$\begin{pmatrix} \ell_1 & \ell_2 & \ell_3 \\ 0 & 0 & 0 \end{pmatrix} = (-1)^L \sqrt{\frac{(L + 2\ell_1)!(L + 2\ell_2)!(L + 2\ell_3)!}{(L+1)!}} \frac{(L/2)!}{(L/2 - \ell_1)!(L/2 - \ell_1)!(L/2 - \ell_1)!} \tag{B.19}$$

where $L = \ell_1 + \ell_2 + \ell_3$. Since problems arise in the numerical evaluation of the factorial for high ℓ, this formula can be replaced appealing to the Gosper version of the Stirling factorial approximation [18]:

$$n! = \left(\frac{n}{e}\right)^n \sqrt{\pi \left(2n + \frac{1}{3}\right)} \tag{B.20}$$

following this approximation the Wigner symbol can be rewrote in a computational simpler form:

$$\begin{pmatrix} \ell_1 & \ell_2 & \ell_3 \\ 0 & 0 & 0 \end{pmatrix} \simeq \left(-\frac{L}{L+1}\right)^{L/2} \frac{1}{(6L+7)^{1/4}} \sqrt{\frac{3e(3L+1)}{\pi(L+1)}} \prod_{i=1}^{3} \frac{(6L-12\ell_i+1)^{1/4})}{\sqrt{3L-6\ell_i+1}} \tag{B.21}$$

Appendix C

Six-Point Correlator

We report the full expression for the six-point correlator we used in chapter 4

$$
\begin{aligned}
&\langle a_{\ell_1 m_1} a_{\ell_2 m_2} a_{\ell_3 m_3} a^*_{\ell_1 m'_1} a^*_{\ell_2 m'_2} a^*_{\ell_3 m'_3} \rangle = \\
&\langle a_{\ell_1 m_1} a^*_{\ell_1 m'_1} \rangle \langle a_{\ell_2 m_2} a^*_{\ell_2 m'_2} \rangle \langle a_{\ell_3 m_3} a^*_{\ell_3 m'_3} \rangle + \langle a_{\ell_1 m_1} a^*_{\ell_1 m'_1} \rangle \langle a_{\ell_2 m_2} a^*_{\ell_3 m'_3} \rangle \langle a_{\ell_3 m_3} a^*_{\ell_2 m'_2} \rangle + \langle a_{\ell_1 m_1} a^*_{\ell_3 m'_3} \rangle \langle a_{\ell_2 m_2} a^*_{\ell_2 m'_2} \rangle \langle a_{\ell_3 m_3} a^*_{\ell_1 m'_1} \rangle + \\
&+ \langle a_{\ell_1 m_1} a^*_{\ell_2 m'_2} \rangle \langle a_{\ell_2 m_2} a^*_{\ell_1 m'_1} \rangle \langle a_{\ell_3 m_3} a^*_{\ell_3 m'_3} \rangle + (-1)^{m_3 - m'_3} \langle a_{\ell_1 m_1} a^*_{\ell_1 m'_1} \rangle \langle a_{\ell_2 m_2} a^*_{\ell_3 - m_3} \rangle \langle a_{\ell_3 - m'_3} a^*_{\ell_2 m'_2} \rangle + \\
&+ (-1)^{m_3 - m'_3} \langle a_{\ell_1 m_1} a^*_{\ell_3 - m_3} \rangle \langle a_{\ell_2 m_2} a^*_{\ell_2 m'_2} \rangle \langle a_{\ell_3 - m'_3} a^*_{\ell_1 m'_1} \rangle + (-1)^{m_2 - m'_2} \langle a_{\ell_1 m_1} a^*_{\ell_2 - m_2} \rangle \langle a_{\ell_2 - m'_2} a^*_{\ell_1 m'_1} \rangle \langle a_{\ell_3 m_3} a^*_{\ell_3 m'_3} \rangle + \\
&+ \langle a_{\ell_1 m_1} a^*_{\ell_2 m'_2} \rangle \langle a_{\ell_2 m_2} a^*_{\ell_3 m'_3} \rangle \langle a_{\ell_3 m_3} a^*_{\ell_1 m'_1} \rangle + (-1)^{m_3 - m'_1} \langle a_{\ell_1 m_1} a^*_{\ell_2 m'_2} \rangle \langle a_{\ell_2 m_2} a^*_{\ell_3 - m_3} \rangle \langle a_{\ell_1 - m'_1} a_{\ell_3 m'_3} \rangle + \\
&+ \langle a_{\ell_1 m_1} a^*_{\ell_3 m'_3} \rangle \langle a_{\ell_2 m_2} a^*_{\ell_1 m'_1} \rangle \langle a_{\ell_3 m_3} a^*_{\ell_2 m'_2} \rangle + (-1)^{m_2 - m'_2} \langle a_{\ell_1 m_1} a^*_{\ell_3 m'_3} \rangle \langle a_{\ell_2 - m'_2} a^*_{\ell_1 m'_1} \rangle \langle a_{\ell_3 m_3} a^*_{\ell_2 - m_2} \rangle + \\
&+ (-1)^{m_2 - m'_2} \langle a_{\ell_1 m_1} a^*_{\ell_2 - m_2} \rangle \langle a_{\ell_2 - m'_2} a^*_{\ell_3 m'_3} \rangle \langle a_{\ell_3 m_3} a_{\ell_1 m'_1} \rangle + (-1)^{m_3 - m'_3} \langle a_{\ell_1 m_1} a^*_{\ell_3 - m_3} \rangle \langle a_{\ell_2 m_2} a^*_{\ell_1 m'_1} \rangle \langle a_{\ell_3 - m'_3} a^*_{\ell_2 m'_2} \rangle + \\
&+ (-1)^{m_1 - m'_1} \langle a_{\ell_1 - m'_1} a^*_{\ell_2 m'_2} \rangle \langle a_{\ell_2 m_2} a^*_{\ell_3 m'_3} \rangle \langle a_{\ell_3 m_3} a_{\ell_1 - m_1} \rangle + (-1)^{m_1 - m'_1} \langle a_{\ell_1 - m'_1} a^*_{\ell_3 m'_3} \rangle \langle a_{\ell_2 m_2} a^*_{\ell_1 - m_1} \rangle \langle a_{\ell_3 m_3} a^*_{\ell_2 m'_2} \rangle
\end{aligned}
\tag{C.1}
$$

Bibliography

[1] M. Abramowitz and I.A. Stegun, *Handbook of Mathematical Functions*, (1972)

[2] J.R. Airey, Phil.Mag. 41:520 (1916)

[3] A. Albrecht and P.J. Steinhardt, Phys.Rev.Lett. 84:5699, (1982)

[4] D. Babich, m. Zaldarriaga, Phys.Rev. D70, (2004) arXiv:astro-ph/0408455

[5] J.M. Bardeem, P.J. Steinhardt, M.S. Turner, Phys.Rev. D28:679, 1983

[6] D. Baumann, H.V. Peiris, Adv.Sci.Lett. 2:105-120, (2009) arXiv:0810.3022 [astro-ph.CO]

[7] D. Baumann, (2009) arXiv:0907.5424 [hep-th]

[8] M. Birkinshaw and S.F. Gull, Nature 302:315-317, (1983)

[9] A. Blanchard and J. Shneider, Astron.Astrophys. 184:1-2, (1987)

[10] R. Brandenberger, R. Kahn, W.H. Press, Phys.Rev. D28:1809, (1983)

[11] X. Chen, Adv.Astron. 2010:638979, (2010) arXiv:1002.1416v3 [astro-ph.CO]

[12] P. Coles, F. Lucchin, *Cosmology*, John Wiley and Sons Ltd, (2002)

[13] P. Creminelli, L. Senatore, M. Zaldarriaga, JCAP 0703:019, (2007) arXiv:astro-ph/0606001v2

[14] S. Dodelson, *Modern Cosmology*, Academic Press, (2003)

[15] J.R. Fergusson, M. Liguori, E.P.S. Shellard, (2009) arXiv:0912.5516 [astro-ph.CO]

[16] J.R. Fergusson, M. Liguori, E.P.S. Shellard, (2010)arXiv:1006.1642v2 [astro-ph.CO]

[17] A. Gangui and J. Martin, Mon.Not.Astron.Soc. 313:323, 2000; Phys.Rev. D62,103004, (2000)

[18] F. Giovi, C. Baccigalupi, F. Perrotta, Phys.Rev. D68:12002, (2003) arXiv:astro-ph/0308118

[19] A Guth, Phys.Rev. D23:347, (1981)

[20] A. Guth and S.Y. Pi, Phys.Rev.Lett. 49:1110, (1982)

[21] A. Guth and S.Y. Pi, Phys.Rev. D32:1899, (1985)

[22] S. Hawking, Phys.Lett. B115:295, (1982)

[23] A.F. Heavens, Mon.Note.R.Astron.Soc., 299:805, (1998)

[24] A.F. Heavens, (2010) arXiv:0906.0664v3 [astro-ph.CO]

[25] W. Hu and S. Dodelson, Ann.Rev.Astron.Astrophys. 40:171-216, (2002) arXiv:astro-ph/0110414v1

[26] W. Hu and Sugiyama

[27] E. Hubble, Proc.Nat.Ac.Sci. 15, (1929)

[28] E. Komatsu and D.N. Spergel, Phys.Rev. D63:063002, (2001) arXiv:astro-ph/0005036v2

[29] M. Liguori, E. Sefusatti, J.R. Fergusson, E.P.S. Shellard, (2010) arXiv:1001.4707v1 [astro-ph.CO]

[30] A. Linde, Phys.Lett. B108:389, (1982)

[31] X. Luo, Ap.J.Lett. 427.l71, (1994)

[32] J.C. Mather et al., Ap.J. 420:439, (1994)

[33] A. Mangilli and L. Verde, Phys.Rev. D80,123007, (2009) arXiv:0906.2317 [astro-ph.CO]

[34] P.J.E. Peebles, Ap.J. 153:1-11, (1968)

[35] P.J.E. Peebles and J.T. Yu, Ap.J. 162:815-836, (1974)

[36] F.M. Persi, D.N. Spergel ,R. Cen, J.P. Ostriker, Astrophys.J. 469:437, (11996)

[37] M.E. Peskin and D.V. Schroeder, *An Introduction To Quantum Field Theory*, Westview Press, (1995)

[38] Planck Collaboration, (2013) arXiv:1303.5076 [astro-ph.CO]

[39] Planck Collaboration, (2013) arXiv:1303.5084 [astro-ph.CO]

[40] M. Rees and D. Sciama. Nature 217:511, (1968)

[41] R.K. Sachs and A.M. Wolfe, Ap.J. 147:73-90, (1967)

[42] S. Seager, D.D. Sasselov, D. Scott, Ap.J.Sup. 128:407-430, (2000)

[43] E. Sefusatti, M. Liguori, A.P.S. Yadav, M.G. Jackson, E. Pajer, JCAP 0912:022, (2009) arXiv:0906.0232

[44] Senatore, K.M. Smith and M. Zaldarriaga, JCAP 1001:028, (2010) arXiv:0905.3746

[45] U. Seljak,Ap.J. 460:549-555, (1996)

[46] U. Seljak and M. Zaldarriaga, Ap.J. 469:437-444, (1996). arXiv:astro-ph/9603033

[47] P. Serra and A. Cooray, Phys.Rev. D77:107305, (2008) arXiv:0801.3276 [astro-ph]

[48] J. Silk, Ap.J. 151:459-471, (1968)

[49] K.M. Smith and M. Zaldarriaga, MNRAS 417:2-19, (2011) arXiv:astro-ph/0612571v2

[50] G.F. Smoot, M.V. Gorenstein, R.A. Muller, Phys.Rev.Lett. 39:898, (1977)

[51] G.F. Smoot, C.L. Bennet, A. Kogut, E.L. Wright, J. Aymon, et al., Ap.J.Lett. 396:L1-L5, (1992)

[52] D.N. Spergel and D.M. Goldberg, Phys.Rev. D59,103001, (1999)

[53] A.A. Starobinsky, Phys.Lett. B117:175, (1982)

[54] R. Sunyaev and Y. Zel'dovich, Comm.Astrophys.Sp.Phys. 4:13, (1972)

[55] R. Tuluie, P. Laguna, Ap.J.Lett. 445:L73-L76, (1995)

[56] L. Verde, A.F. Heavens, S. Matarrese, Mon.Not.Roy.Astron.Soc. 318:584, (2000) arXiv:astro-ph/0002240

[57] G.N. Watson, *A Treatise on the Theory of Bessel Functions*, Cambridge University Press, (1944)

[58] Y. Zel'dovich, V. Kurt, R. Sunyaev, Sov.Phys.JETP 28:146, (1969)

[59] Y. Zel'dovich and R. Sunyaev, Astrophys.Space.Sci. 4:301, (1969)